

Self-Commissioning of Linear Toothed Belt Drives

DIPLOMA THESIS

Conducted in partial fulfillment of the requirements for the degree of a
Diplom-Ingenieur (Dipl.-Ing.)

supervised by

Univ.-Prof. Dr. techn. A. Kugi
Dr. techn. T. Glück

submitted at the

TU Wien

Faculty of Electrical Engineering and Information Technology
Automation and Control Institute

by

David Gruber
Matriculation number 1026565
Ambach 52
3124 Oberwölbling
Austria

Vienna, June 14, 2017

Vorwort

Diese Arbeit bildet den Abschluss meines Diplomstudiums der Regelungstechnik an der TU Wien. Ich danke an dieser Stelle Univ.-Prof. Dr. techn. A. Kugi, der mich durch seine Begeisterungsfähigkeit in meiner Wahl der Studienrichtung stets aufs Neue bestätigt hat.

Die Thematik dieser Diplomarbeit begeistert mich durch die Verknüpfung der theoretischen Lösungsansätze mit der Schwierigkeit diese auch praktisch zu implementieren. Obgleich dies manchmal auch Grund für Rückschläge war, so sehr schätze ich die abwechslungsreichen Herausforderungen im Rückblick.

Für die thematische Unterstützung während der Diplomarbeit möchte ich meinem Betreuer, Dr. techn. Tobias Glück, herzlich danken, der mir zu jederzeit beratend beistand. Ebenfalls sei an dieser Stelle Stefan Flixeder für die Unterstützung und Betreuung gedankt.

Meinen Kollegen Ulrich Knechtelsdorfer, Jakob Maderthaner und Michael Robin möchte ich für die gemeinsame Zeit und technische wie moralische Unterstützung während des gesamten Masterstudiums meinen Dank aussprechen. Ein herzliches Danke auch an all meine Freunde abseits des universitären Alltags für die schöne Zeit in den vergangenen Jahren. Außerdem sei das Forum Schweißkultur für die notwendige Ablenkung während der Ausarbeitung dieser Arbeit dankend erwähnt.

Besonderer Dank gilt insbesondere meiner Familie, die mich bedingungslos während meines gesamten Studiums unterstützt und mir stets Rückhalt geboten hat.

Vielen Dank!

Man muss das Unmögliche versuchen, um das Mögliche zu erreichen.

Hermann Hesse

Wien, 14. Juni, 2017

Abstract

This work deals with the self-commissioning of toothed linear belt drives. The self-commissioning includes the mathematical modelling of the system, the identification of the model parameters and the automatic controller design based on the parametric model. The presented algorithms utilize only little a priori knowledge of the system. The necessary information can be found in the data sheets of the used hardware. A feedback and feedforward controller are provided as result of the proposed algorithms. The algorithms allow for a direct implementation in the motor-controller software due to the time-discrete implementation. If the desired application needs further tuning of the control loop, this can be done by suitably adapting the design parameters of the proposed algorithms. All the algorithms are tested on an experimental setup.

The mathematical model utilizes the mechanical structure of toothed linear belt drives and is furthermore reduced to a two-mass-spring-damper model including nonlinear friction. The cascaded controller consists of an inner velocity controller and a superimposed position controller. The inner control loop is parametrized as proportional-integral-velocity-controller and the outer control loop as proportional-position-controller. Moreover, an appropriate feedforward controller is designed based on the identified mathematical model. The identification process and the controller design are automatized, that is, no further interaction of the user is required during the commissioning of the system.

Kurzzusammenfassung

Diese Arbeit beschäftigt sich mit der Selbstinbetriebnahme von Linearachsen mit Zahnriemenantrieb für Positionieraufgaben. Dabei wird die mathematische Modellierung des Systems, die Identifikation der Modellparameter und die darauf aufbauende automatisierte Reglerauslegung behandelt. Die vorgestellten Algorithmen verwenden dabei geringes a priori Wissen über das System. Die notwendigen Daten können den Datenblättern der verwendeten Hardware entnommen werden. Der präsentierte Algorithmus liefert als Ergebnis die fertig parametrisierte Reglerkaskade mit Vorsteuerung und kann durch die zeitdiskrete Implementierung direkt in die Motorcontroller-Software integriert werden. Falls gewünscht, kann der Endanwender das Systemverhalten anhand von wenigen Tuning-Parametern weiter anpassen. Die vorgestellten Algorithmen werden anhand eines Testaufbaus getestet und verifiziert.

Das mathematische Modell wird basierend auf dem mechanischen Aufbau hergeleitet und auf ein Zwei-Massen-Modell mit nichtlinearer Reibung reduziert. Die Reglerkaskade besteht aus einem inneren Geschwindigkeitsregelkreis und einem äußeren Regelkreis, der die Position des Systems regelt. Für den inneren Regelkreis wird ein Proportional-Integral Geschwindigkeitsregler eingesetzt, während für den überlagerten Positionsregler ein Proportionalregler zur Anwendung kommt. Außerdem wird anhand der identifizierten Modellparameter eine geeignete Vorsteuerung abgeleitet. Die Systemidentifikation und der Reglerentwurf sind dabei soweit automatisiert, dass keine weitere Interaktion des Endanwenders für die Inbetriebnahme notwendig ist.

Contents

1	Introduction	1
1.1	Test rig	2
1.2	Literature survey	3
1.3	Structure of this thesis	4
2	Mathematical modeling	5
2.1	Linear toothed belt drive	5
2.1.1	Model assumptions	6
2.1.2	Drive train	7
2.1.3	Three-mass-spring-damper model	8
2.1.4	Two-mass-spring-damper model	11
2.2	System analysis and characteristics	15
3	System identification	20
3.1	Excitation signals	20
3.2	Empirical transfer function estimate	23
3.3	Identification strategies	24
3.3.1	Open-loop identification	26
3.3.2	Closed-loop identification	26
	Direct closed-loop identification	27
	Indirect closed-loop identification	27
3.4	Identification results	28
3.5	Parameter fitting	31
3.6	Friction identification	34
4	Control strategies	37
4.1	Control structure	37
4.2	Velocity controller design	38
4.2.1	Prefilter design	38
	Notch filter design	38
	Butterworth filter design	39
4.2.2	PI-controller design	40
4.3	Position controller design	42
4.4	Feedforward controller design	44
5	Closed-loop measurement results	46
5.1	Influence of the prefilter	46
5.2	Influence of the feedforward control	46
5.3	Influence of the moving mass	48

6	Implementation	52
6.1	Velocity signal calculation	52
6.1.1	Event counter approach	55
6.1.2	Gate measurement approach	57
6.1.3	Combined gate measurement and event counter approach	59
6.2	Integrator anti-windup	61
6.3	Trajectory generator	62
7	Conclusions and outlook	66
	Appendices	68
A	Parameters	68
A.1	Data sheet parameters	68
A.2	Identified parameters	70
A.2.1	Plant parameters	70
A.2.2	Controller parameters	71
A.2.3	Trajectory generator parameters	72
A.2.4	Friction parameters	72
A.3	Simulation parameters	73
B	Comparison of a PID- and a P-PI-control structure	75
C	Additional derivations	78
C.1	Event counter approach	78
C.2	Gate measurement approach	79

List of Figures

1.1	Picture of the test rig as used for experiments.	2
2.1	Schematic of a belt driven servo mechanism.	5
2.2	Schematics of the drive train.	7
2.3	Schematic equivalent three-mass-spring-damper system of the belt driven system.	8
2.4	Comparison of the position-dependent stiffnesses of the two- and three-mass-spring-damper model.	9
2.5	Orientation of the linear axis relative to earth's gravitation field.	11
2.6	Simplified two-mass-spring-damper system of the belt driven servo mechanism.	12
2.7	Bode diagrams of the different simplified transfer functions.	15
2.8	Influence of parameter changes on the frequency response function.	17
2.9	Position-dependency of the frequency response.	18
2.10	Comparison of the transfer functions from motor torque to motor angle and to cart position.	19
3.1	Time-domain representation of pseudo random binary signals for different orders and clock periods.	22
3.2	PRBS in the frequency domain for different orders and clock periods.	22
3.3	Clary's method II using a priori knowledge of the system.	24
3.4	Schematic control circuits for open- as well as direct and indirect closed-loop identification.	25
3.5	Influence of the current control loop on the direct open-loop empirical transfer function estimate using Clary's method.	29
3.6	Comparison of the resulting frequency response function of the open- and closed-loop approaches.	31
3.7	Improvement of the signal to noise ratio by averaging the frequency response function measurement.	32
3.8	Comparison of the raw data frequency response function and the fitted parametric model.	33
3.9	Illustration of the data reduction from linear frequency spacing to nearly logarithmically spacings.	34
3.10	Measured torque using different measurement scenarios and fitted friction torque model.	36
4.1	Block diagram of the control strategy.	37
4.2	Block diagram of the velocity control loop.	38
4.3	Transfer function of a Notch filter, a second-order Butterworth filter and the nominal plant transfer function.	40

4.4	Comparison of the velocity controller with different prefilters.	42
4.5	Open-loop transfer function of the velocity controlled plant.	43
4.6	Block diagram of the position control loop.	43
4.7	Open-loop transfer function of the position controlled plant.	45
5.1	Influence of the prefilter on the controlling performance	47
5.2	Position change from $\xi = 0$ mm to $\xi = 500$ mm using a Butterworth filter for filtering the mechanical resonance with linear, nonlinear and without feedforward control and moving mass $m_c = 11.2$ kg.	49
5.3	Position change from $\xi = 0$ mm to $\xi = 500$ mm using a Butterworth filter for filtering the mechanical resonance with linear, nonlinear and without feedforward control and moving mass $m_c = 0$ kg.	50
5.4	Position change from $\xi = 0$ mm to $\xi = 500$ mm using a Butterworth filter for filtering the mechanical resonance and nonlinear feedforward control with different moving masses.	51
6.1	Velocity signal calculated by a first-order high-pass filter.	53
6.2	Illustration of the problem using a time-discrete high-pass filter to estimate a velocity signal from the position signals of an incremental encoder. . . .	54
6.3	Showcase of the state machine and of the calculation of the increments from the quadrature incremental encoder signals.	55
6.4	Graphical visualization of the event counter approach for estimating the actual velocity.	56
6.5	Comparison of the relative velocity errors of the gate measurement approach and the event counter approach.	57
6.6	Schematic picture of the gate measurement approach for velocities above the intended measurement range.	59
6.7	Schematic picture of the timeout extension of the gate measurement approach.	60
6.8	Comparison of the time-dependency of the gate measurement approach and event counter approach for estimating the velocity signal based on the incremental encoder signals.	61
6.9	Block diagram of the velocity control loop with filtered velocity control error \hat{e}_ω	62
6.10	Influence of the integrator anti-windup on the control results	63
6.11	Visualization of the working principle of the 7-step trajectory generator. . . .	65
B.1	Comparison of a proportional-integral-derivative-controller and a proportional-integral cascaded controller including feedforward control.	76

List of Tables

A.1	Data sheet parameters of the toothed belt axis EMMS-AS-70-S-LS-RMB from Festo used in the test rig.	68
A.2	Data sheet parameters of the linear axis EGC-70-600-TB-KF-0H-GK from Festo used in the test setup.	69
A.3	Data sheet parameters of the connection kit EAMM-A-L38-70A from Festo used in the test setup.	69
A.4	Plant parameters $G_{\mathcal{A}}$ for additional mass $m_c = 11.2$ kg mounted on the cart.	70
A.5	Plant parameters $G_{\mathcal{B}}$ for no additional mass $m_c = 0$ kg mounted on the cart.	70
A.6	Controller parameters $C_{\mathcal{A}}$ for plant $G_{\mathcal{A}}$, using a Notch filter in the controller design process and a phase margin $\varphi_r^\omega = 60^\circ$ for the velocity controller and $\varphi_r^\varphi = 80^\circ$ for the position controller, as well as a resonance suppression factor of $A_{\text{sup}} = -10$ dB.	71
A.7	Controller parameters $C_{\mathcal{B}}$ for plant $G_{\mathcal{A}}$, using a Butterworth filter in the controller design process and a phase margin $\varphi_r^\omega = 60^\circ$ for the velocity controller and $\varphi_r^\varphi = 80^\circ$ for the position controller, as well as a resonance suppression factor of $A_{\text{sup}} = -10$ dB.	71
A.8	Parameters $T_{\mathcal{A}}$ of the 7-step trajectory generator used for all experiments.	72
A.9	Parameters $T_{\mathcal{B}}$ of the 7-step trajectory generator.	72
A.10	Friction parameters for the system configurations $G_{\mathcal{A}}$ and $G_{\mathcal{B}}$	73
A.11	Plant parameters $S_{\mathcal{A}}$ for simulations.	73
A.12	Plant parameters $S_{\mathcal{B}}$ for simulations.	73
A.13	Plant parameters $S_{\mathcal{C}}$ for simulations.	74

Nomenclature

α	Tilt of the linear axis relative to a horizontal reference
$\ddot{\xi}_{\min}, \ddot{\xi}_{\max}$	Acceleration boundaries of the cart
$\Delta\xi_{\min}$	Minimal resolution of an incremental encoder
Δt_{\min}	Minimal measurable time period
$\Delta\dot{\xi}_{h, \text{err}}$	Relative velocity error in percent of the event counter approach
$\Delta\dot{\xi}_{l, \text{err}}$	Relative velocity error in percent of the gate measurement approach
δ_{sw}	Switching function for merging of the velocity signal estimation approaches
$\dot{\xi}_{\min}, \dot{\xi}_{\max}$	Velocity boundaries of the cart
$(\dot{\cdot})$	Total time derivative
$\dot{\xi}$	Cart velocity
$\dot{\xi}_{h, \max}$	Maximal measureable velocity of the event counter approach
$\dot{\xi}_{h, \min}$	Minimal measureable velocity of the event counter approach
$\dot{\xi}_h$	Velocity signal estimation of the event counter approach
$\dot{\xi}_{l, \max}$	Maximal measureable velocity of the gate measurement approach
$\dot{\xi}_{l, \min}$	Minimal measureable velocity of the gate measurement approach
$\dot{\xi}_l$	Estimated velocity signal of the gate measurement approach
$\dot{\xi}_m$	Combined velocity estimation of the gate measurement approach and the event counter approach
$\dot{\xi}_{\text{sw}}$	Velocity value at which the gate measurement and the event counter approach provide the same relative error
$(\hat{\cdot})$	Laplace transformed variable
\hat{G}_i	Identified a priori unknown part of the transfer function within Clary's method
I	Complex number
κ	Inertia rate
K_a^{PPI}	Acceleration feedforward for P-PI controller
K_I^{PPI}	Integrator gain of the P-PI controller
K_P^{PPI}	Proportional gain of the velocity controller in the P-PI controller cascade
K_{PP}^{PPI}	Proportional gain of the position controller in the P-PI controller cascade
K_v^{PPI}	Velocity feedforward for P-PI controller
$(\cdot)^*$	Optimal value regarding the according quality criteria
$[\cdot]$	Integer floor operation
$\mathcal{F}\{\cdot\}$	Fast Fourier Transformation
$\min(\cdot)$	Minimum of the argument according to the parameter in subscript
(\cdot)	Frequency
ω	Frequency
ω_1	Angular velocity of the driving pulley

ω_2	Angular velocity of the driven pulley
ω_{bw}	Cutoff frequency of the Butterworth filter
ω_c	Cutoff frequency of the velocity controlled loop
ω_d	Desired motor angular velocity
ω_g	Gearbox angular velocity
ω_m	Motor angular velocity
$\omega_{r,n}$	Center frequency of the Notch filter
ω_r	Mechanical resonance frequency
ω_z	Mechanical antiresonance frequency
$\omega_{c,\varphi}$	Cutoff frequency of the position controlled loop
φ_1	Angle of the driving pulley
φ_2	Angle of the driven pulley
φ_d	Desired motor angle
φ_g	Angle of the gearbox
φ_m	Motor angle
φ_r^ω	Phase margin of the velocity controller
φ_r^φ	Phase margin of the position controller
φ_d	Desired motor angle
τ^{FF}	Feedforward torque
τ_1	External torque acting on the driving pulley
τ_2	External torque acting on the end side pulley
τ_c	Coulomb friction parameter of motor and gearbox
τ_d	Desired motor torque
τ_e	Exciting torque for identifying the plant in closed-loop
τ_g	Gearbox torque
τ_i	Input of the identification process
τ_{mR}	Friction torque acting on the motor
τ_m	Motor torque
$\tau_m^I - \tau_m^{VI}$	Measurement dataset of the motor torque within the friction identification
τ_R	Motor torque to overcome static friction
$\tau_{c\omega}$	Motor torque due to controlling action in closed-loop identification
$\tau_{m,max}$	Maximum allowed motor torque
$\arg(\cdot)$	Phase function of the transfer function in the argument
$\text{env}(\cdot)$	Envelope of the argument
$\text{mod}(\cdot, \cdot)$	Modulo operator
$\text{sign}(\cdot)$	Signum function
Θ_e	Replacement moment of inertia of the motor, pulley and gearbox
Θ_g	Mass moment of inertia of the gearbox
Θ_m	Mass moment of inertia of the driving motor
Θ_r	Mass moment of inertia of the pulleys
$\tilde{\tau}_c$	Identified Coulomb friction parameter of the nonlinear friction model
\tilde{d}_v	Identified viscous damping parameter of the nonlinear friction model
$\tilde{G}_{\tau_m, \varphi_m}$	Transfer function from motor momentum to motor angle without belt damping d

\tilde{m}_e	Replacement mass for the feedforward control design
\mathbf{A}	System matrix of the two-mass-spring-damper model
\mathbf{b}	Input vector of the two-mass-spring-damper model
\mathbf{c}	Output vector of the two-mass-spring-damper model
\mathbf{f}	Nonlinear system of differential equations of the two-mass-spring-damper model
\mathbf{f}_{3m}	Nonlinear system of differential equations of the three-mass-spring-damper model
\mathbf{p}	Parameters to be estimated based on the frequency response function
\mathbf{x}	State vector of the two-mass-spring-damper model
\mathbf{x}_{3m}	State vector of the three-mass-spring-damper model
ξ	Cart position
ξ_d	Desired cart position
$\xi_{end}, \dot{\xi}_{end}, \ddot{\xi}_{end}$	End position, velocity and acceleration for the trajectory planning
ξ_{min}, ξ_{max}	Position boundaries of the cart
$\xi_{start}, \dot{\xi}_{start}, \ddot{\xi}_{start}$	Initial position, velocity and acceleration for the trajectory planning
A_{bw}	Design parameter of the Butterworth filter to limit its influence on lower frequencies
A_{Notch}	Design parameter of the Notch filter to limit its influence on lower frequencies
A_{sup}	Resonance suppression factor
c	Stiffness coefficient of the belt in the two-mass-spring-damper model
c_1, c_2, c_3	Stiffness coefficients of the three-mass-spring-damper model
C_ω	Transfer function of the velocity controller
C_φ	Transfer function of the position controller
C_τ	Transfer function of the current controller
d	Damping coefficient of the belt in the two-mass-spring-damper model
d_1, d_2, d_3	Damping coefficients of the three-mass-spring-damper model
d_c	Viscous friction parameter of the cart
d_m	Viscous friction parameter of the motor
d_n	Design parameter of the Notch filter
e_ω	Error of the velocity controlled loop
f	External force acting on the cart
f_c	Coulomb friction parameter of the cart
f_g	Gravitational force acting on the cart
f_R	Friction force at the cart
$f_{PRBS,max}$	Maximum spectral frequency content of a PRBS
$f_{PRBS,min}$	Minimum spectral frequency content of a PRBS
g	Gravity constant
G'_{τ_m, φ_m}	Transfer function from motor momentum to motor angle with belt damping d
$G_{\tau_m, \varphi_m}^{hf}$	High frequency approximation of the transfer function from motor torque to motor angle
$G_{\tau_m, \varphi_m}^{lf}$	Low frequency approximation of the transfer function from motor torque to motor angle

G_{bw}	Transfer function of the Butterworth filter
$G_{cc,cl}$	Closed-loop transfer function from desired torque to actual motor torque
G_{dt}	Dead time transfer function of the current controlled loop
G_i	Unknown part of the transfer function within Clary's method
G_{Notch}	Transfer function of the Notch filter
G_{PI}	Transfer function of the velocity controller
G_{pre}	Prefilter for damping the mechanical resonance
G_R	Transfer function for estimating the motor angular velocity from the motor angle
$G_{\omega,cl}$	Closed-loop transfer function of the velocity controlled plant
$G_{\varphi_m,\xi}$	Transfer function from motor angle to cart position
$G_{\varphi_m,\xi}$	Transfer function from motor angle to cart position
G_{τ_m,φ_m}	Simplified linear transfer function from motor torque to motor angle
G_{i_m,τ_m}	Transfer function from motor current to motor torque
i_g	Gearbox transmission ratio
i_m	Motor current
i_t	Combined gearbox and pulley transmission ratio
J	Quality criteria for parameter fitting
j	Jerk of the cart
J_{dt}	Quality criteria for calculating the dead time due to the current controller
j_{min}, j_{max}	Jerk boundaries of the cart
k_m	Motor constant
l_1	Distance between the center of the driving pulley and the left mounting point of the belt at the cart
l_2	Distance between the center of the driven pulley and the right mounting point of the belt at the cart
l_3	Distance between the driving and the end side pulley
L_τ	Open-loop transfer function of the current controlled plant
L_m	Winding inductance of the motor
l_ξ	Minimum distance between the center of the driving pulley and the center of the moving cart
m_c	Mass of the moving cart
n_b	Denominator of the known part within Clary's method
n_{inc}	Amount of increments in one sampling period
n_{PRBS}	Order of a PRBS
n_T	Parameter of the dead time element
P_{PRBS}	Clock period of a PRBS
R	Resonance ratio
r	Effective radius of the pulleys
R_m	Winding resistance of the motor
S	Input disturbance sensitivity transfer function of the closed-loop identification methods
s	Continuous-time Laplace variable
s_{PRBS}	Time-discrete signal values of a PRBS signal without regarding the clock period

$T_{\varphi_d, \varphi_m}^{\text{PID}}$	Transfer function of a PID-controller from desired motor angle to actual motor angle
$T_{\varphi_d, \varphi_m}^{\text{PPI}}$	Transfer function of a cascaded P-PI-controller from desired motor angle to actual motor angle
T_{inc}	Time between two consecutive increments within the gate measurement approach
T_{out}	Timeout of the gate measurement approach
T_s	Sampling time of all time-discrete systems
T_{trj}	Time needed for a position change under regard of the constraints of the trajectory generator
t_T	Dead time of the current controlled loop
T_R	Realization time constant for the first-order high-pass filter
$T_{n,\text{inc}}$	Measured time within the event counter approach
$T_{n,\text{inc}}$	Time between the first and last increment in one sampling period of the event counter approach
u	System input
V_1, V_2	Transfer functions of the prefilters within Clary's method
x_I	Integrator state of the velocity controller
y	System output
z	Complex variable of the time-discrete z-Transformation
z_b	Numerator of the known part within Clary's method

List of Abbreviations

PSM	permanent-magnet synchronous motor
PRBS	pseudorandom binary signal
GPRBS	generalized pseudorandom binary signal
FFT	Fast Fourier transformation
ETFE	empirical transfer function estimate
SISO	single input single output
RLSQ	recursive least squares
RTH	real-time hardware
FPGA	field programmable gate array
BWN	band limited white noise
SNR	signal to noise ratio
AWGN	additive white Gaussian noise
PID	proportional-integral-differential
P	proportional
PI	proportional-integral
FRF	frequency response function
SMC	sliding mode control
IMC	internal model control

1 Introduction

Modern production lines in industry make use of conveyor belts and industrial robots to increase productivity and competitiveness. Belt driven linear drives can be used as conveyor belts, propulsion chains for overhead cranes or even to build up a pick and place robot in delta design. Belt driven linear drives are constructed for high dynamic usage with low to medium masses. They utilize diverter pulleys to convert the rotatory movement of a motor into a linear movement of a cart mounted at the connecting belt. In contrast to spindle axis, belt driven linear axes can achieve higher velocities and accelerations of about one order of magnitude. Moreover, they are easier to build, which results in significant lower costs compared to spindle drives. The usage of belts introduces additional resonances in the lower frequency range, which need to be taken into account during the whole hardware design process and especially in the controller design. Another costly detail is the position measurement of the driven cart. While a rotary incremental encoder is mostly available at the motor side for controlling the motor torque, velocity and position, an incremental encoder at the moving cart is often not desirable. This is because of the necessary wiring, the additional hardware needed, and the constraints on the hardware design of the moving cart and the connected components due to the required space for the sensor and the adjacent encoder stripe.

The fundamental problem of controlling a propulsion chain is quite common in modern automation tasks. For example, an industry robot consists of up to seven serial position systems, each consisting of nearly the same system structure as the presented linear belt driven servo system. Nearly all motor driven positioning systems show a distinct resonance-antiresonance behavior due to the mechanical construction. Thus, the presented problem can be generalized above the scope of this diploma thesis, that is the application in belt driven servo systems.

This diploma thesis deals with self-commissioning of belt driven linear drives. The main goal is to support the technician with a toolbox for commissioning of the hardware while the actual controller characteristics can be easily adjusted to the needs of the target application. That is, a faster controller for high speed pick and place applications with softer constraints on the absolute position accuracy or a more robust, but slower controller setting for increased robustness against parameter variations like the moving mass. The technician therefore does not need in-depth knowledge of control and identification theory because commissioning is automatically performed by the presented algorithms, thus, simplifying the controller tuning of linear belt driven servo systems. Moreover, the model-based approach allows to gather diagnostic information about the system state. As to mention, allowing for failure prediction.

The subsequent section explains the test hardware and setup used for all experiments and for the verification of the presented algorithms and strategies. The second section of this chapter gives a short literature survey of the state of the art in auto-tuning

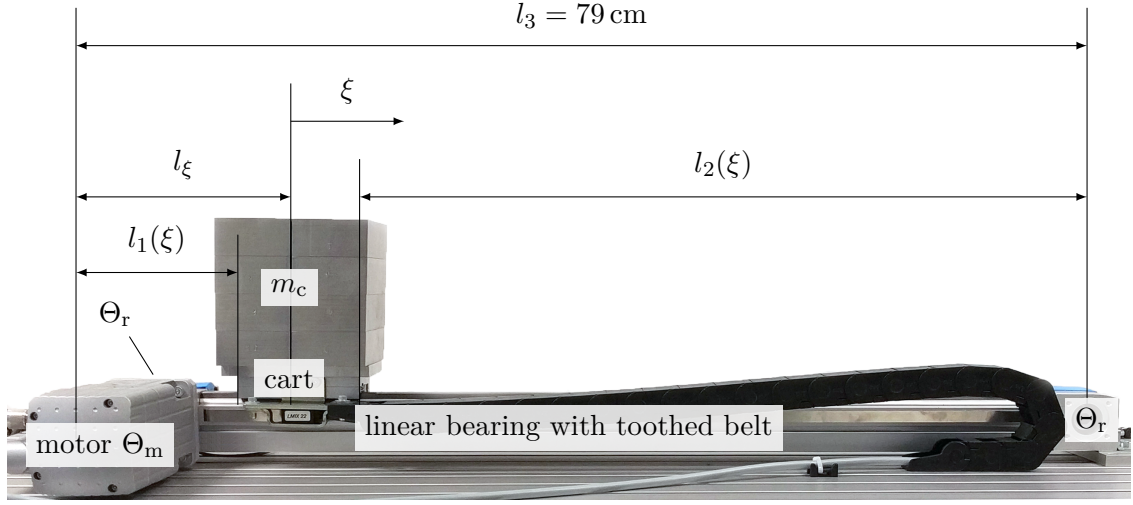


Figure 1.1: Picture of the test rig for all practical experiments presented in this diploma thesis.

and self-commissioning techniques on belt driven servo systems with emphasis on the differences compared to this work. In the last section of this chapter, the structure of this thesis is explained.

1.1 Test rig

A picture of the test setup for all experiments and measurements in this diploma thesis is shown in Figure 1.1. The motor (see parameters listed in Table A.1 in Appendix A) with mass moment of inertia Θ_m is relatively stiff coupled with the linear bearing (see parameters listed in Table A.2 in Appendix A) via an axial coupling set (see parameters listed in Table A.3 in Appendix A). The linear axis consists of a driving pulley at the motor side and a driven pulley at the opposite site of the axis, both with mass moment of inertia Θ_r . The distance between the centers of the pulleys is given by the constant length l_3 . Both pulleys are connected via a flexible toothed belt. Its ends are mounted at the moving cart, which can change its position ξ linearly along the linear bearing. Depending on the actual position of the moving cart the distance $l_1(\xi)$, which is the distance between the center of the driving pulley and the left side of the cart, the distance $l_2(\xi)$, which denotes the distance from the right mounting point of the belt at the cart to the center of the driven pulley, changes. In the initial position of the cart $\xi = 0$, the distance between the center of the driving pulley and the center of the moving cart encounters its minimum value l_ξ . In order to simulate different masses m_c mounted at the moving cart, additional weights in form of iron blocks can be mounted on the cart, each with a mass of about 1.3 kg. The motor is used in closed-loop current controlled mode.

1.2 Literature survey

Regarding the system identification process, Schütte [1] presents a framework for identifying belt driven servo mechanisms with test signals in a closed-loop approach. In contrast to [1], Henke [2] presents a pure model-based approach. He builds up a database of models for the motor and the mechanical subsystems from which the user can choose the used components. The models are manually tuned to fit the real hardware. Hence, the user selects the mathematical model by choosing the used components. Thus, only components that are listed in the database can be used and wearing or aging of the components is not modeled. Jokinen [3] and Jokinen et al. [4] present a model of a belt driven servo mechanism quite similar to the one used in this work. However, they identify the model by using the values of belt pretension provided by the manufacturer. This is often too inaccurate because of manufacturing tolerances and imperfections. In [5], Selezneva builds up the mathematical model using only the dataset given by the manufacturer and identifies the friction parameters using torque steps with different amplitude and alters the model parameters accordingly to fit the actual hardware. This leads, however, to a rather imprecise of the system dynamics due to tolerances in the data sheets or manufacturing imperfections. In addition, aging is not regarded within this approach. In [6], a comparison of an open-loop and a direct and indirect closed-loop system identification is provided. It is concluded that each of the approaches can be used to identify the system parameters. In [7], Nevaranta and in [8], Saarakkala utilize an online estimation approach for identifying the parameters of a linear model.

Regarding the control design strategy, Saarakkala [8] shows in his comparison of the works from Jokinen et al. [4], Saarakkala et al. [6, 9–13], and Harnefors et al. [14] that a controller cascade in the form of a proportional-integral (PI)-velocity-controller and a proportional (P)-position-controller provides sufficient control performance compared to more sophisticated nonlinear control strategies. Moreover, Schütte presented in [1] a state-space-based PI-velocity-controller with additional disturbance feedforward and a superimposed P-position-controller. This controller shows only satisfactory control performance and little robustness with respect to parameter variations. Additionally, an internal model control (IMC) approach and a P-PI-controller with state variable filter and torque backlash feedforward is presented. However, the IMC shows insufficient robustness to parameter variations, whereas the P-PI-controller cascade delivered the best control performance regarding the position accuracy and robustness. A Notch filter is utilized to dampen the mechanical resonance frequency in the P-PI-controller approach, which is used in a similar form in this work. In [2] a combined time- and frequency-domain quality criterion is stated and utilized to design a PI-velocity-controller and a P-position-controller. Furthermore, in [7] a linear quadratic controller is compared to a sliding mode control (SMC) and an online adaptive control algorithm. The work [7] concludes that the sliding mode controller is not preferable for mechanical systems due to the infinite controller bandwidth that is necessary and the hard switching behavior. The linear quadratic controller needs the partially not observable state variables and an appropriate weighting of the feedback matrices that often require further manual tuning. The adaptive controller, as proposed in [7], needs a robust and stable online identification algorithm, which can be used to adapt the controller parameters. However, the online identification

approach is limited by the amount and degree of the nonlinear friction, which limits the generality of the approach. Therefore, in [7], also a proportional-integral-differential (PID)-structure is used for control. In [3], Jokinen also uses a PID-controller, which, however, is based on the quantitative feedback theory.

1.3 Structure of this thesis

In Chapter 2, the mathematical model of a belt driven servo mechanism is derived starting with a three-mass-spring-damper model. It is simplified to a parametric two-mass-spring-damper model. In Chapter 3, this simplified model is identified by an open- and closed-loop empirical frequency response analysis. The frequency responses are then used to identify the characteristic parameters of the two-mass-spring-damper-model. The closing section of this chapter deals with the identification of the dominant nonlinearity of the system, the Coulomb friction. In Chapter 4, the parametric model is then used to design a cascaded feedback control structure to control the velocity and the position. The end section of this chapter deals with the design of a feedforward controller. Chapter 5 presents the measurement results based on the controller design of Chapter 4 and outlines the differences, advantages and disadvantages of the examined control strategies. Chapter 6 deals with some details on the implementation, as to mention, the integrator anti-windup, the generation of the velocity signals from the incremental encoder position signals and the generation of time-optimal position trajectories meeting constraints on the velocity, acceleration and jerk. The closing chapter, Chapter 7, gives a summary of the presented control and identification techniques and provides suggestions for improvements, which need further research and investigation beyond the scope of this diploma thesis.

2 Mathematical modeling of linear toothed belt drives

In this chapter, a mathematical model for linear toothed belt drives is derived. In a first step, the model is presented as a concentrated three-mass-spring-damper model. It is then further simplified to obtain a reduced two-mass-spring-damper model. The latter is furthermore linearized in order to obtain a linear model. This model forms the basis for the subsequent parameter identification presented in Chapter 3 and the controller design presented in Chapter 4. The frequency response behavior of the linear two-mass-spring-damper model and the implications of the applied simplifications are shown in more detail. Although this diploma thesis deals with the controller design based on the linearized model of the plant, this chapter also elaborates the main causes for the nonlinear behavior.

2.1 Linear toothed belt drive

Figure 2.1 depicts a schematic of a linear toothed belt driven servo mechanism.

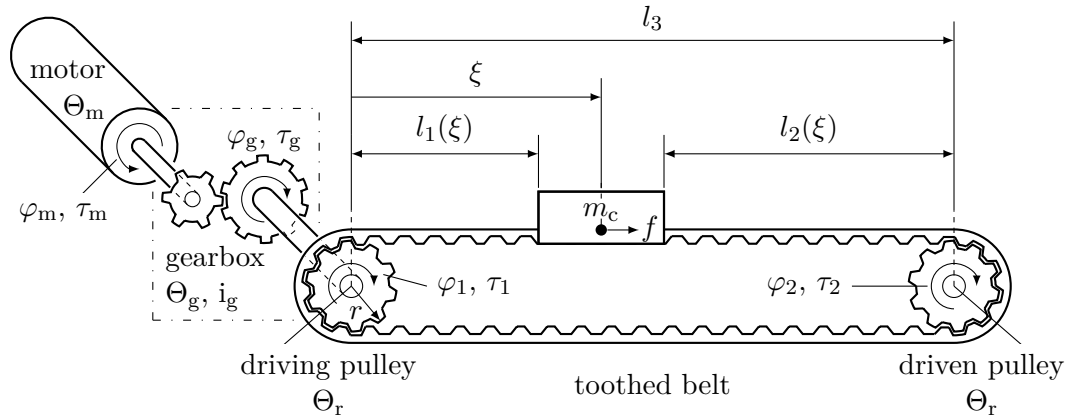


Figure 2.1: Schematic of a belt driven servo mechanism.

A linear toothed belt driven servo mechanism [15, 96ff] typically consists of a driving motor, e. g., a permanent-magnet synchronous motor (PSM) with mass moment of inertia Θ_m , motor angle φ_m and motor torque τ_m , which actuates a flexible timing-belt via a driving pulley with mass moment of inertia Θ_r , driving pulley angle φ_1 , pulley torque τ_1 and effective radius r . An optional gearbox with mass moment of inertia Θ_g , gear angle

φ_g and gear torque τ_g realizes a gear reduction. The transmission ratio is given by

$$i_g = \frac{\omega_m}{\omega_g}, \quad (2.1)$$

where

$$\omega_m = \dot{\varphi}_m = \frac{d\varphi_m}{dt} \quad (2.2a)$$

and

$$\omega_g = \dot{\varphi}_g = \frac{d\varphi_g}{dt} \quad (2.2b)$$

are the total time-derivatives of φ_m and φ_g , respectively, see [16] and [17]. The toothed belt connects the pulley at the driving side with the pulley at the end side. The distance between the pulleys and, hence, the length of the belt drive is given by l_3 . The angle and the torque of the end side pulley are denoted by φ_2 and τ_2 , respectively. Nearly all industrially used toothed belt drives utilize the same pulley for the driving side and the end side. Because of this, the end side pulley is assumed to have a mass moment of inertia Θ_r . A cart with mass m_c is mounted on the toothed belt and the cart position is denoted by ξ . An external force f is assumed to act on the cart.

2.1.1 Model assumptions

The schematics of a belt driven servo system depicted in Figure 2.1 allows to make a few assumptions, which simplify the mathematical modeling and enables a schematic representation of the system as a three-mass-spring-damper system. The following assumptions are made, see also [4, 5, 17, 18] and [19, 190ff]:

- The gearbox is assumed to be lossless and shows no backlash.
- The coupling between motor and gearbox is sufficiently stiff.
- The coupling between gearbox and driving pulley is supposed to be stiff.
- The toothed belt is assumed to be massless and the flexibility can be modeled by concentrated spring and damper elements, cf. Figure 2.3.
- The dynamics of the current-controlled motor is negligible, compared to the mechanical dynamics.

The assumptions on the rigid couplings are justified by the relatively small and, hence, dominant stiffness of the belt in comparison to the stiffness of the metal shaft connections, see parameters listed in Table A.2 and in Table A.3 in the Appendix A.

The mechanical resonance frequency of the toothed belt drive is typically in the range of 100Hz, see [16, 20, 21], which is significantly lower than the dynamics of the current-controlled electrical drive. Although not modeled, these dynamics will be identified as dead time element in Chapter 3. The motor is hence described by its motor constant k_m

in N m/A. This proportional factor gives the relationship between the motor current i_m and its associated torque

$$\tau_m = k_m i_m \quad (2.3)$$

by neglecting its dynamics.

2.1.2 Drive train

The drive train depicted in Figure 2.2 consists of a motor which generates a torque τ_m . It is driving a gearbox with the driving pulley connected rigidly to the output side.

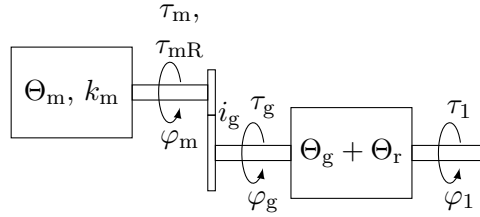


Figure 2.2: Schematics of the drive train.

The assumption of a lossless gear box implies

$$\tau_m \omega_m = \tau_g \omega_g, \quad (2.4)$$

which leads together with (2.1) to the torque transmission

$$\tau_g = i_g \tau_m \quad (2.5)$$

of the gearbox. The rigid coupling between the motor and gear box states

$$\varphi_g = \frac{\varphi_m}{i_g}, \quad (2.6)$$

and, additionally, the assumed rigid coupling between gearbox and the driving pulley is expressed by

$$\varphi_1 = \varphi_g. \quad (2.7)$$

The balance of angular momentum at the motor side results in

$$\underbrace{\left(\Theta_m + \frac{\Theta_r + \Theta_g}{i_g^2} \right)}_{\Theta_e} \ddot{\varphi}_m = \tau_m + \tau_{mR} + \frac{\tau_1}{i_g}, \quad (2.8)$$

with regard of the previously made assumptions, especially (2.5) and (2.7). Here, τ_{mR} denotes the sum of all friction forces in the motor, gearbox and driving pulley.

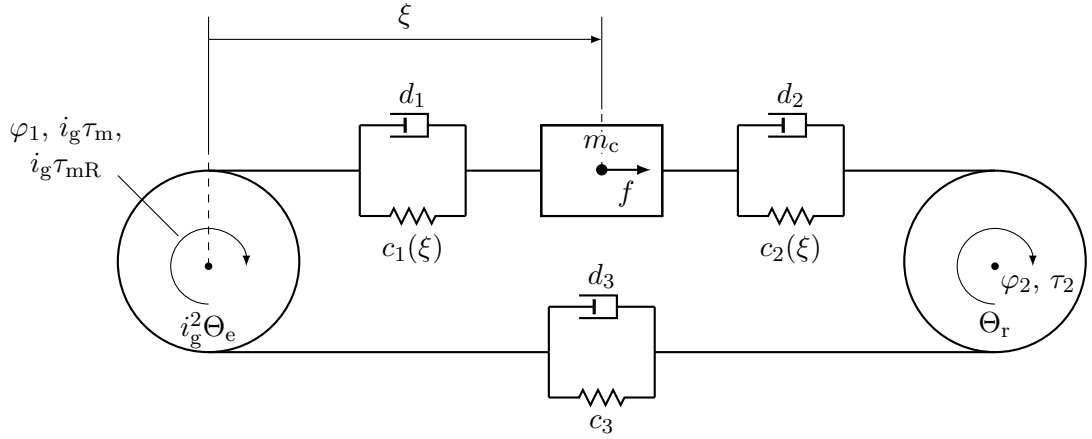


Figure 2.3: Schematic equivalent three-mass-spring-damper system of the belt driven system.

2.1.3 Three-mass-spring-damper model

Applying the previously stated assumptions on the subsystem consisting of the linear bearing and the toothed belt, depicted in Figure 2.1, a three-mass-spring-damper model can be deduced, see [3, 16]. The schematic of this model is depicted in Figure 2.3. The segments of the belt between the driving and the driven pulley, as well as the ones between the pulleys and the cart are represented by spring and damper elements with parameters d_1 , d_2 , d_3 , $c_1(\xi)$, $c_2(\xi)$ and c_3 . It is worth mentioning that the spring stiffnesses $c_1(\xi)$ and $c_2(\xi)$ depend on the cart position ξ as the length of the according belt segments, that is $l_1(\xi)$ and $l_2(\xi)$, vary with the position of the cart, see Figure 2.1.

The stiffness parameters can be approximately estimated by Hooke's Law [22, p. 13ff] with the relative change in length

$$\varepsilon_0 = \frac{dl}{l_0} = \frac{f_0}{EA} \quad (2.9)$$

using the modulus of elasticity E , the cross section area A as well as the initial length l_0 and the absolute change in length dl induced by an initial force f_0 of the belt. The stiffness c_0 of a segment of the belt with initial length l_0 stressed with a force f_0 is therefore given by

$$c_0 = \frac{EA}{l_0} = \frac{f_0}{l_0 \varepsilon_0}, \quad (2.10)$$

if its relative change in length is denoted by ε_0 . Figure 2.4 illustrates the position-dependency of the spring elements due to the change of the initial length of the belt segments with length $l_1(\xi)$ and $l_2(\xi)$. Here, c denotes the replacement stiffness for the two-mass-spring-damper model introduced in Section 2.1.4.

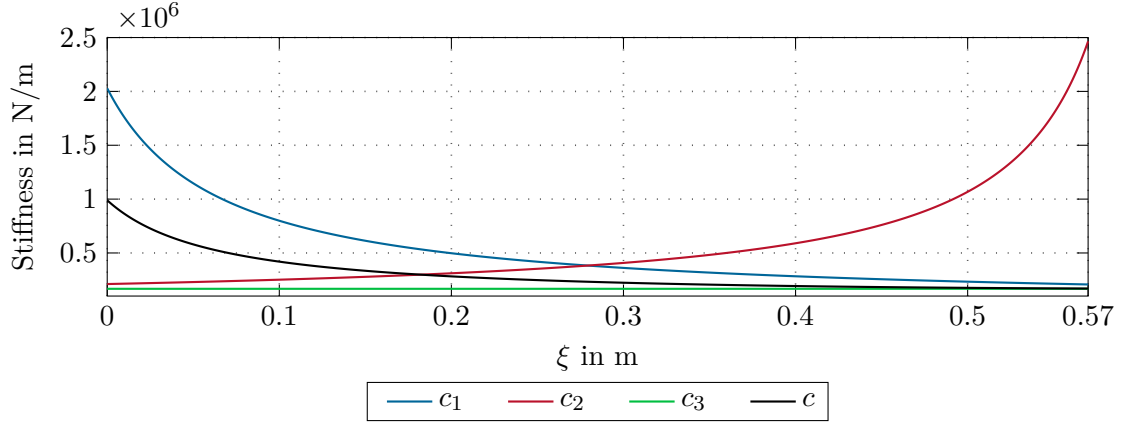


Figure 2.4: Comparison of the position-dependent stiffnesses of the two- and three-mass-spring-damper model.

Moreover, the balance of angular momentum at the driving pulley side reads as

$$i_g^2 \Theta_e \dot{\omega}_1 = i_g (\tau_m + \tau_{mR}) - r c_1(\xi) (r \varphi_1 - \xi) - r d_1 (r \omega_1 - \dot{\xi}) - r^2 c_3 (\varphi_1 - \varphi_2) - r^2 d_3 (\omega_1 - \omega_2) \quad (2.11)$$

and at the end side pulley

$$\Theta_r \ddot{\varphi}_2 = \tau_2 - r c_2(\xi) (r \varphi_2 - \xi) - r d_2 (r \dot{\varphi}_2 - \dot{\xi}) - r^2 c_3 (\varphi_2 - \varphi_1) - r^2 d_3 (\omega_2 - \omega_1), \quad (2.12)$$

where r is the effective radius of the pulleys and

$$\omega_1 = \dot{\varphi}_1 = \dot{\varphi}_g = \omega_g \quad (2.13a)$$

as well as

$$\omega_2 = \dot{\varphi}_2 \quad (2.13b)$$

denote the angular velocities of the driving and driven pulley. The balance of linear momentum applied to the moving cart results in

$$m_c \ddot{\xi} = f + c_1(\xi) (r \varphi_1 - \xi) + d_1 (r \omega_1 - \dot{\xi}) + c_2(\xi) (r \varphi_2 - \xi) + d_2 (r \dot{\varphi}_2 - \dot{\xi}). \quad (2.14)$$

Under the assumption of rigid couplings between the motor, the gearbox and the driving pulley, see (2.6) and (2.7), (2.11) can be equivalently expressed using the motor angle φ_m instead of the driving pulley angle φ_1 , thus, leading to

$$\Theta_e \ddot{\varphi}_m = \tau_m + \tau_{mR} - i_t c_1(\xi) (i_t \varphi_m - \xi) - i_t d_1 (i_t \dot{\varphi}_m - \dot{\xi}) - i_t^2 c_3 (\varphi_m - i_g \varphi_2) - i_t^2 d_3 (\dot{\varphi}_m - i_g \dot{\varphi}_2). \quad (2.15)$$

Here, the transmission coefficient

$$i_t = \frac{r}{i_g} \quad (2.16)$$

of the driving pulley and the gearbox was introduced. A comparison of (2.8) and (2.15) shows that the driving pulley torque τ_1 , which connects the drive train and the toothed belt linear bearing, can be expressed as

$$\tau_1 = -rc_1(\xi)(i_t\varphi_m - \xi) - rd_1(i_t\omega_m - \dot{\xi}) - ri_tc_3(\varphi_m - i_g\varphi_2) - ri_td_3(\omega_m - i_g\omega_2). \quad (2.17)$$

The system dynamics regarding the states ξ , φ_m , φ_2 and their corresponding time derivatives $\dot{\xi}$, ω_m , ω_2 is hence described by the three second-order ordinary differential equations (2.12), (2.14) and (2.15). Introducing the state vector

$$\mathbf{x}_{3m}^T = [\varphi_m \quad \omega_m \quad \varphi_2 \quad \omega_2 \quad \xi \quad \dot{\xi}] \quad (2.18)$$

and input

$$u = \tau_m \quad (2.19)$$

allows to state the three-mass-spring-damper model in the form

$$\begin{aligned} \dot{\mathbf{x}}_{3m} &= \mathbf{f}_{3m}(\mathbf{x}_{3m}, u) \\ &= \begin{bmatrix} \omega_m \\ \frac{1}{\Theta_e} \left(\tau_m + \tau_{mR} + \frac{\tau_1}{i_g} \right) \\ \frac{1}{\Theta_r} \left(\tau_2 - rc_2(r\varphi_2 - \xi) - rd_2(r\dot{\varphi}_2 - \dot{\xi}) - r^2c_3\left(\varphi_2 - \frac{\varphi_m}{i_g}\right) - r^2d_3\left(\dot{\varphi}_2 - \frac{\dot{\varphi}_m}{i_g}\right) \right) \\ \frac{1}{m_c} \left(f + c_1(i_t\varphi_m - \xi) + d_1(i_t\dot{\varphi}_m - \dot{\xi}) + c_2(r\varphi_2 - \xi) + d_2(r\dot{\varphi}_2 - \dot{\xi}) \right) \end{bmatrix}. \end{aligned} \quad (2.20)$$

These equations contain the nonlinear friction torques τ_{mR} and τ_2 . The motor friction is modeled by

$$\tau_{mR} = -d_m\omega_m - \tau_c\text{sign}(\omega_m), \quad (2.21)$$

where d_m is the viscous damping coefficient and τ_c denotes the Coulomb friction coefficient, see [23]. The end pulley friction τ_2 is modeled in a similar fashion. Moreover, a tilt of the belt drive relative to the gravitational field is considered. Depending on the orientation of the servo system relative to earth's gravitational force field, see Figure 2.5, the gravity component is given by

$$f_g = -m_cg \sin(\alpha), \quad (2.22)$$

where the angle α denotes the tilt of the axis relative to the horizontal reference mounting orientation and g is the gravitational acceleration. The cart friction force f_R is modeled by

$$f_R = -d_c\dot{\xi} - f_c\text{sign}(\dot{\xi}), \quad (2.23)$$

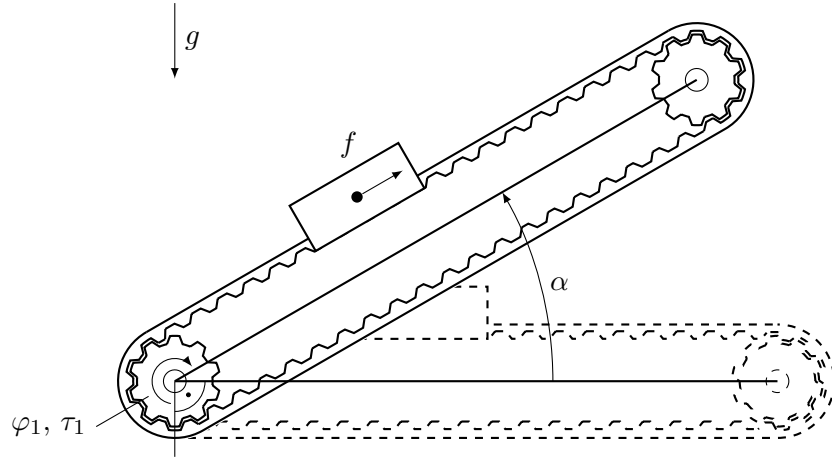


Figure 2.5: Orientation α of the linear axis relative to earth's gravitational field.

with the viscous damping coefficient d_c and the Coulomb friction coefficient f_c of the cart. Hence, the force f in (2.20) is given by

$$f = f_R + f_g. \quad (2.24)$$

The nonlinear system of differential equations (2.20) is hard to identify due to the large number of parameters, including position-dependent stiffnesses and time-varying friction. Moreover, the position of the cart ξ and driven pulley angle φ_2 are not measurable in practice, as sensors at the moving cart are not desired due to difficult wiring and additional costs. Moreover, sensors for the driven pulley do not provide additional information unless the cart position is externally fixed. Hence, further simplifications are necessary, which will result in a two-mass-spring-damper system presented in the following.

2.1.4 Two-mass-spring-damper model

Assuming that the inertia of the end side pulley Θ_r is small in comparison to the motor inertia Θ_m and the moving mass m_c , the influence of its dynamics (2.12) on the system behavior can be neglected. A two-mass-spring-damper model, schematically depicted in Figure 2.6, can be inferred. The balance of momentum gives rise to

$$\Theta_e \dot{\omega}_m = \tau_m + \tau_{mR} - i_t c (i_t \varphi_m - \xi) - i_t d (i_t \omega_m - \dot{\xi}) \quad (2.25a)$$

and

$$m_c \ddot{\xi} = f + c (i_t \varphi_m - \xi) + d (i_t \omega_m - \dot{\xi}). \quad (2.25b)$$

The springs with stiffness coefficient c_2 and c_3 , depicted in Figure 2.3, operate in series to each other and parallel to the spring with stiffness coefficient c_1 . Hence, approximately, the replacement stiffness coefficient is given by

$$c(\xi) = c_1(\xi) + \frac{c_2(\xi)c_3}{c_2(\xi) + c_3}. \quad (2.26)$$

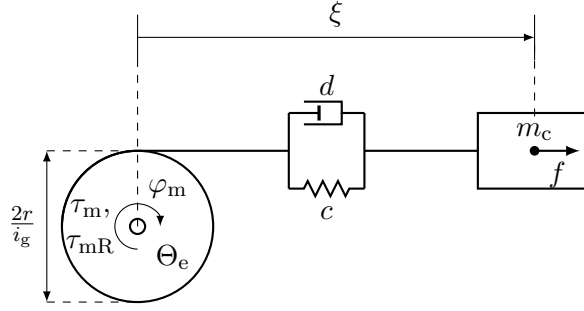


Figure 2.6: Simplified two-mass-spring-damper system of the belt driven servo mechanism.

The position-dependency of this replacement spring is depicted in Figure 2.4. It is obvious that the spring with stiffness c_1 dominates the resulting stiffness c .

Analogously, the damper with coefficient d replaces d_2 in series with d_3 and both parallel to d_1 , so that

$$d = d_1 + \frac{d_2 d_3}{d_2 + d_3} \quad (2.27)$$

holds. Again, the introduction of the state vector

$$\mathbf{x}^T = [\varphi_m \quad \omega_m \quad \xi \quad \dot{\xi}] \quad (2.28)$$

and the input

$$u = \tau_m \quad (2.29)$$

with the mathematical model (2.25a) and (2.25b) yields

$$\dot{\mathbf{x}} = \mathbf{f}(\mathbf{x}, u) = \begin{bmatrix} \omega_m \\ \frac{1}{\Theta_e} \left(\tau_m + \tau_{mR} - i_t c (i_t \varphi_m - \xi) - i_t d (i_t \dot{\varphi}_m - \dot{\xi}) \right) \\ \dot{\xi} \\ \frac{1}{m_c} \left(f + c (i_t \varphi_m - \xi) + d (i_t \dot{\varphi}_m - \dot{\xi}) \right) \end{bmatrix}. \quad (2.30)$$

In order to preserve the benefits of a linear model, the position dependency of the stiffness $c = c(\xi)$ is dropped and replaced by the worst case stiffness when the cart is closest to the end side pulley. This is only an approximation as shown by the measurement results in Figure 2.9 for three different positions.

In addition, only viscous friction, i. e.,

$$\tau_{mR} = -d_m \omega_m \quad (2.31)$$

and

$$f_R = -d_c \dot{\xi} \quad (2.32)$$

is considered and the tilt angle is neglected, i. e., $\alpha = 0$, which allows to state the linear two-mass-spring-damper model in the form

$$\dot{\mathbf{x}} = \mathbf{A}\mathbf{x} + \mathbf{b}u, \quad (2.33)$$

with

$$\mathbf{A} = \begin{bmatrix} 0 & 1 & 0 & 0 \\ -\frac{i_t^2 c}{\Theta_e} & -\frac{i_t^2 d + d_m}{\Theta_e} & \frac{i_t c}{\Theta_e} & \frac{i_t d}{\Theta_e} \\ 0 & 0 & 0 & 1 \\ \frac{i_t c}{m_c} & \frac{i_t d}{m_c} & -\frac{c}{m_c} & -\frac{d + d_c}{m_c} \end{bmatrix} \quad (2.34)$$

and

$$\mathbf{b}^T = \begin{bmatrix} 0 & \frac{1}{\Theta_e} & 0 & 0 \end{bmatrix}. \quad (2.35)$$

Furthermore, we define the output

$$y = \varphi_m = \mathbf{c}^T \mathbf{x} \quad (2.36)$$

with

$$\mathbf{c}^T = \begin{bmatrix} 1 & 0 & 0 & 0 \end{bmatrix}. \quad (2.37)$$

The respective transfer function from the motor torque $\tau_m = u$ to the motor angle $\varphi_m = y$ is given by

$$\begin{aligned} G'_{\tau_m, \varphi_m}(s) &= \frac{\hat{\varphi}_m}{\hat{\tau}_m} = \frac{\hat{y}}{\hat{u}} \\ &= \mathbf{c}^T (s\mathbf{E} - \mathbf{A})^{-1} \mathbf{b} \\ &= \frac{b'_2 s^2 + b'_1 s + b'_0}{a'_4 s^4 + a'_3 s^3 + a'_2 s^2 + a'_1 s} \end{aligned} \quad (2.38a)$$

with coefficients

$$b'_0 = c, \quad (2.38b)$$

$$b'_1 = d + d_c, \quad (2.38c)$$

$$b'_2 = m_c, \quad (2.38d)$$

$$a'_1 = i_t^2 c(d_c + d_m), \quad (2.38e)$$

$$a'_2 = c(\Theta_e + i_t^2 m_c) + i_t^2 (dd_m + dd_c + d_m d_c), \quad (2.38f)$$

$$a'_3 = i_t^2 m_c(d + d_m) + \Theta_e(d + d_c), \quad (2.38g)$$

$$a'_4 = m_c \Theta_e. \quad (2.38h)$$

Here, s denotes the Laplace variable and the notation $(\hat{\cdot})$ is introduced for the Laplace transformed signals. Due to the high friction of the moving cart and the motor, cf.

Section 3.6, the damping parameter d of the toothed belt is rather small. Therefore, this parameter is neglected in the following. Accordingly, the transfer function (2.38) becomes

$$\begin{aligned}\tilde{G}_{\tau_m, \varphi_m}(s) &= \frac{\hat{\varphi}_m}{\hat{\tau}_m} \\ &= \frac{\tilde{b}_2 s^2 + \tilde{b}_1 s + \tilde{b}_0}{\tilde{a}_4 s^4 + \tilde{a}_3 s^3 + \tilde{a}_2 s^2 + \tilde{a}_1 s}\end{aligned}\quad (2.39a)$$

with

$$\tilde{b}_0 = c, \quad (2.39b)$$

$$\tilde{b}_1 = d_c, \quad (2.39c)$$

$$\tilde{b}_2 = m_c, \quad (2.39d)$$

$$\tilde{a}_1 = i_t^2 c (d_c + d_m), \quad (2.39e)$$

$$\tilde{a}_2 = c (\Theta_e + i_t^2 m_c) + i_t^2 d_m d_c, \quad (2.39f)$$

$$\tilde{a}_3 = i_t^2 m_c d_m + \Theta_e d_c, \quad (2.39g)$$

$$\tilde{a}_4 = m_c \Theta_e. \quad (2.39h)$$

It is worth noting that for frequencies below the resonance frequency, the transfer function

$$G_{\tau_m, \varphi_m}^{\text{lf}}(s) = \frac{1}{c} \frac{m_c s^2 + d_c s + c}{s^2 (\Theta_e + i_t^2 m_c) + s i_t^2 (d_m + d_c)} \quad (2.40)$$

gives a sufficiently good approximation as shown in the bode diagram depicted in Figure 2.7. For frequencies around the resonance frequency and upwards, the transfer function

$$G_{\tau_m, \varphi_m}^{\text{hf}}(s) = \frac{m_c}{s^2 m_c \Theta_e + s (i_t^2 m_c d_m + \Theta_e d_c) + c (\Theta_e + i_t^2 m_c)} \quad (2.41)$$

approximates the behavior of the system, cf. Figure 2.7. As a consequence of this, an approximation of the transfer function (2.39) is given by

$$\begin{aligned}G_{\tau_m, \varphi_m}(s) &= G_{\tau_m, \varphi_m}^{\text{lf}}(s) G_{\tau_m, \varphi_m}^{\text{hf}}(s) \underbrace{c \frac{\Theta_e + i_t^2 m_c}{m_c}}_{\chi} \\ &= \underbrace{\frac{1}{s^2 (\Theta_e + i_t^2 m_c) + s i_t^2 (d_m + d_c)}}_{\text{rigid part}} \underbrace{\frac{m_c s^2 + d_c s + c}{\frac{\Theta_e m_c}{\Theta_e + i_t^2 m_c} s^2 + \frac{i_t^2 m_c d_m + \Theta_e d_c}{\Theta_e + i_t^2 m_c} s + c}}_{\text{flexible part}} \\ &= \frac{\tilde{b}_2 s^2 + \tilde{b}_1 s + \tilde{b}_0}{\tilde{a}_4 s^4 + (\tilde{a}_3 + \tilde{a}_{3,e}) s^3 + (\tilde{a}_2 + \tilde{a}_{2,e}) s^2 + \tilde{a}_1 s} \\ &\approx \tilde{G}_{\tau_m, \varphi_m}(s).\end{aligned}\quad (2.42)$$

The error caused by this approximation is given by the additive factors

$$\tilde{a}_{2,e} = \frac{i_t^2 (d_m + d_c)}{\Theta_e + i_t^2 m_c} (i_t^2 m_c d_m + \Theta_e d_c) \quad (2.43a)$$

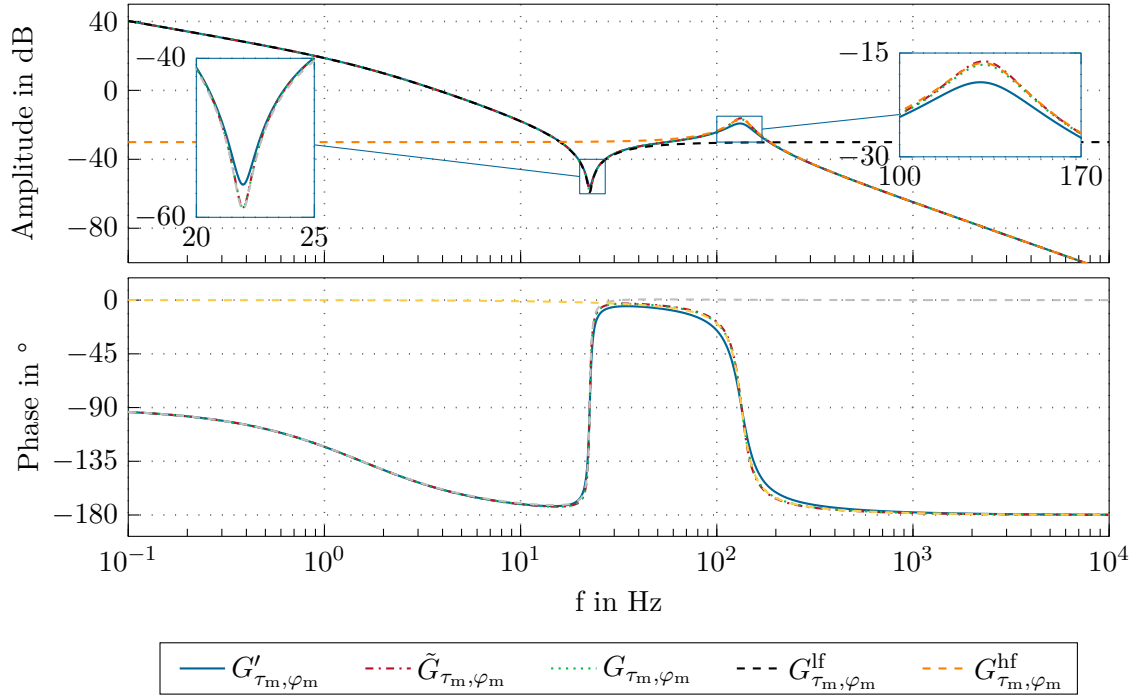


Figure 2.7: Bode diagram of the full linear model G'_{τ_m, φ_m} , simplified model $\tilde{G}_{\tau_m, \varphi_m}$ without belt damping and the approximations $G^{\text{lf}}_{\tau_m, \varphi_m}$, $G^{\text{hf}}_{\tau_m, \varphi_m}$ as well as G_{τ_m, φ_m} . Simulation parameter set $S_{\mathcal{A}}$ in Appendix A.

and

$$\tilde{a}_{3,e} = i_t^2(d_m + d_c) \frac{\Theta_e m_c}{\Theta_e + i_t^2 m_c} \quad (2.43b)$$

in the denominator. The factor χ compensates for $\lim_{s \rightarrow \infty} G^{\text{lf}}_{\tau_m, \varphi_m}$ as well as for $\lim_{s \rightarrow 0} G^{\text{hf}}_{\tau_m, \varphi_m}$. The transfer function (2.42) allows to separate the system into a rigid and a flexible part, see also [3].

2.2 System analysis and characteristics

The separation does not significantly influence the location of the resonance and antiresonance frequency. In the undamped case, $d_c = d_m = 0$, the resonance frequency ω_r is in accordance with the flexible part of (2.42) given in the form

$$\omega_r = \sqrt{c \frac{\Theta_e + i_t^2 m_c}{\Theta_e m_c}} \quad (2.44)$$

and the antiresonance frequency by

$$\omega_z = \sqrt{\frac{c}{m_c}}. \quad (2.45)$$

If the inertia rate

$$\kappa = \frac{i_t^2 m_c}{\Theta_e} \quad (2.46)$$

is introduced, the resonance ratio reads as

$$R = \frac{\omega_r}{\omega_z} = \sqrt{1 + \kappa}. \quad (2.47)$$

Note that increasing the mass m_c of the cart shifts the antiresonance frequency towards lower frequencies and increases the resonance ratio R and, hence, the frequency distance between the resonance and antiresonance frequency. Figure 2.8 depicts the transfer function $G_{\tau_m, \varphi_m}(s)$ for different cart masses m_c and stiffness coefficients c of the belt. An increased belt stiffness coefficient c increases the resonance and antiresonance frequency by the same factor. Clearly, the resonance ratio R remains constant for constant masses, cf. (2.47). However, the belt stiffness actually depends on the position, which is why both resonances are shifted with a changing position, cf. (2.44) and (2.45). This position-dependency is depicted in Figure 2.9 for three different cart positions. In the following, the position-dependency is neglected, however, in the controller design, presented in Chapter 4, a model with the lowest resonance and antiresonance frequency is considered. This worst case approximation occurs when the cart mass m_c is highest and the stiffness c is lowest, which corresponds to the cart position ξ farthest away from the driven end.

By looking at the Bode diagram depicted in Figure 2.7, it is noticeable that for low frequencies up to the antiresonance frequency ω_z , the system behaves like a rigid coupled servo system. Above this characteristic frequency, the subsystem of the moving cart decouples from the driving subsystem including the motor and an optional gearbox which leads to the characteristic resonance-antiresonance-behavior. This decoupling property depends mostly on the moving mass m_c and the stiffness coefficient c of the belt. Moreover, the antiresonance marks an upper bound on the closed-loop control bandwidth with regard to a limited maximum torque due to motor size and belt force restrictions. As the stiffness tends to get lower for longer linear axis, see (2.10), the expected system performance will decrease with both, length of the axis and moving mass.

For positioning purposes, however, the transfer function $G_{\tau_m, \xi}(s)$ from the motor torque τ_m to the cart position ξ is of particular interest. In the assumed linear case, the transfer function reads as

$$\begin{aligned} G_{\tau_m, \xi}(s) &= G'_{\tau_m, \varphi_m}(s) G_{\varphi_m, \xi}(s) \\ &= i_t \frac{ds + c}{\tilde{a}_4 s^4 + \tilde{a}_3 s^3 + \tilde{a}_2 s^2 + \tilde{a}_1 s}, \end{aligned} \quad (2.48)$$

where the first part $G'_{\tau_m, \varphi_m}(s)$ denotes the transfer function (2.38a) from the motor torque τ_m to the motor angle φ_m and

$$G_{\varphi_m, \xi}(s) = \frac{\hat{\xi}}{\hat{\varphi}_m} = i_t \frac{ds + c}{m_c s^2 + s(d + d_c) + c} \quad (2.49)$$

is the transfer function from the motor angle φ_m to the cart position ξ . In contrast to the transfer function G'_{τ_m, φ_m} , $G_{\tau_m, \xi}$ lacks the antiresonance, as depicted in Figure 2.10.

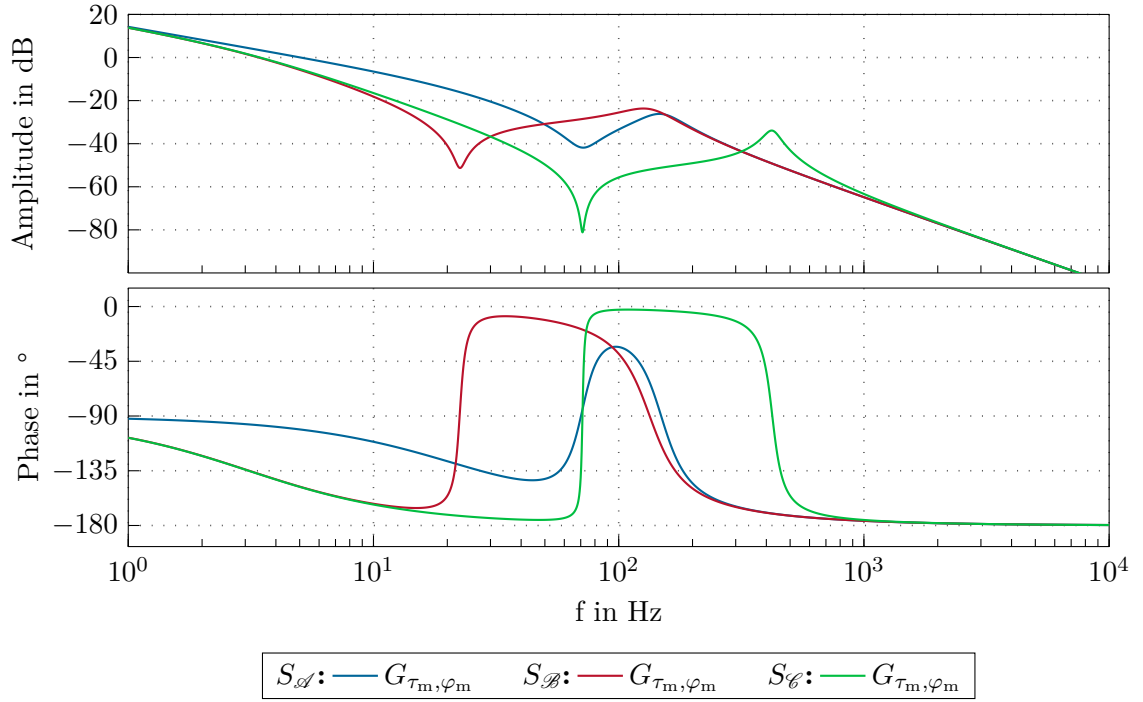


Figure 2.8: Bode diagram of the plant model $G_{\tau_m, \varphi_m}(s)$ for the parameter sets $S_{\mathcal{A}}$, $S_{\mathcal{B}}$ and $S_{\mathcal{C}}$ given in Table A.11, Table A.12 and Table A.13 in Appendix A. The moving mass and belt stiffness are changed by one order of magnitude.

In order to conclude the chapter on the mathematical modeling of the toothed belt driven servo mechanism, the simplified and linearized model with the transfer function G_{τ_m, φ_m} from the motor torque τ_m to the motor angle φ_m presented in (2.42) builds the starting point for the parameter identification in Chapter 3 and the controller design in Chapter 4. Although the position-dependency is neglected and the belt damping is assumed to be of minor influence on the response behavior, this model can be used to estimate the system parameters that are needed for the feedforward and the feedback control design. Moreover, if the positioning mechanism is tilted by an angle α relative to the horizontal alignment, the presented model can remain unchanged for system identification purposes. The only difference is that an offset in the motor momentum given by (2.22) has to be applied in order to compensate the nonlinearity due to the gravitation.

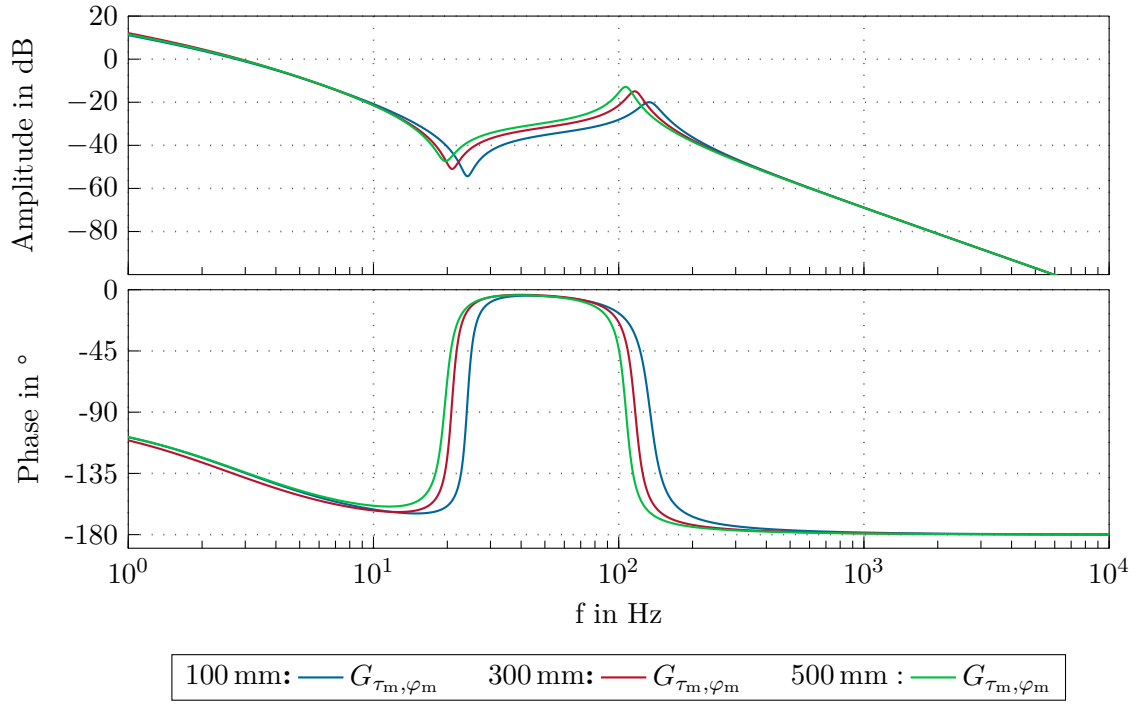


Figure 2.9: Position-dependency of the frequency response G_{τ_m, φ_m} for the cart positions $\xi = 100$ mm, $\xi = 300$ mm and $\xi = 500$ mm. The picture shows the identified and fitted bode plots in an open-loop setup for plant configuration $G_{\mathcal{A}}$, see Table A.4 in Appendix A.

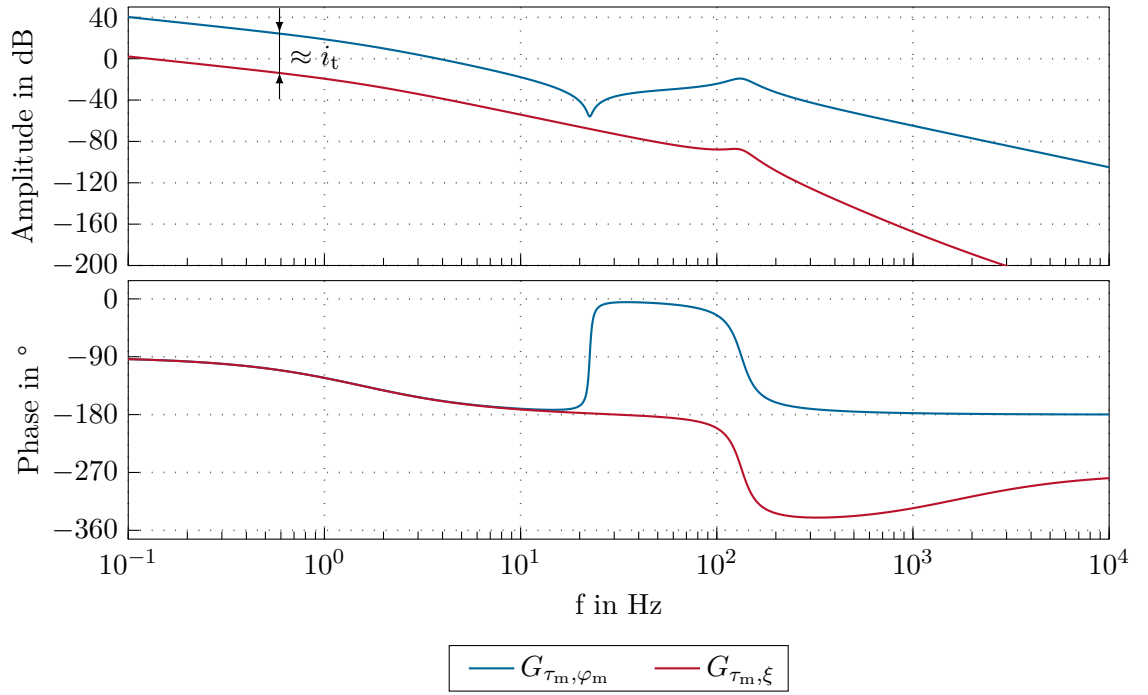


Figure 2.10: Bode diagram of the transfer function from motor torque to motor angle G_{τ_m, φ_m} and to cart position $G'_{\tau_m, \xi}$ for the simulation parameters $S_{\mathcal{A}}$ listed in Table A.11 in Appendix A.

3 System identification and verification

This chapter covers mainly the offline parameter identification of the linear transfer function (2.42). The first section deals with the different excitation signals, their parameters and influence on the identification process. In the subsequent section, the offline identification method utilizing the frequency response function (FRF), which is implemented on the target system, is described in more detail. In a first step, the FRF is determined and the parametrized model from Chapter 2, in particular (2.42), is then fitted to this function. The closing section of this chapter presents a method for identification of the nonlinear friction parameters which can be used to design an appropriate feedforward compensation.

3.1 Excitation signals

In order to identify a dynamic system, the excitation signals must be chosen in such a way that the system is sufficiently excited in the interesting frequency regions, see [24]. For a belt driven servo system, these frequencies start in the range of one and go up to a few hundred Hertz depending on the length of the axis, belt pretension and the moving mass m_c . The excitation signal should not move the cart in an undefined way with long strokes when operated in open loop because the system behavior, and consequently the parameters to be identified change with the position ξ of the cart. Therefore, the excitation signal should lead to a minimal deviation of the position from its initial value during the identification process. In practice, two different excitation signals are often used in system identification, namely a chirp signal and a pseudorandom binary signal (PRBS), see [25, p. 418ff] and [25, p. 423].

A chirp signal consists of a sine wave with continuously changing frequency $\omega_{1,\text{chirp}} \leq \omega \leq \omega_{2,\text{chirp}}$ over time. An additional windowing function, typically of trapezoidal form, can be applied in a multiplicative way to fade-in and fade-out the chirp signal. However, the chirp signal has two main disadvantages. First and foremost, it leads to larger position changes of the target system compared to white noise, especially in the lower frequency region, when used for open-loop identification. Moreover, if the system exhibits large friction, the cart may get stuck for small cart velocities, at least for low frequencies. In order to overcome friction and not violating the position boundaries, it is difficult to find an appropriate setting for the amplitude of the signal. Because of these reasons, a PRBS is preferred for the system identification.

Ideally, a band limited white noise (BWN) signal excites a system with equal spectral power density up to its cutoff frequency. Above this frequency, the dynamics of the system are not excited, at least in the ideal case. However, it is hard to generate a white noise signal and even harder to limit its spectral distribution by an ideal low-pass filter and, therefore, a digital approximation is often used [26, p. 161ff]. A PRBS qualifies as an appropriate excitation signal, see also [7, 27, 28]. Besides its amplitude, a PRBS has two

parameters which allow the frequency spectrum to be stretched and shifted, namely its order n_{PRBS} and the so-called clock period P_{PRBS} [25, p. 422]. The order n_{PRBS} defines the maximum amount of different signal points

$$M = 2^{n_{\text{PRBS}}} - 1 \quad (3.1)$$

generated in one period of the signal, whereas the clock period P_{PRBS} allows to shift the spectrum towards lower frequencies by using each signal value $s_{\text{PRBS}}(k)$ P_{PRBS} -times. We introduce the short notation $\text{PRBS}_{P_{\text{PRBS}}}^{n_{\text{PRBS}}}$, which denotes a **PRBS** with order n_{PRBS} and clock period P_{PRBS} . The values of the **PRBS** are then characterized by

$$s_{\text{PRBS}}(k) = \text{mod} (a_{1,\text{PRBS}}s(k-1) + \dots + a_{n_{\text{PRBS}},\text{PRBS}}s(k-n_{\text{PRBS}}), 2), \quad (3.2)$$

for

$$k = 0, \dots, 2^{n_{\text{PRBS}}} - 2, \quad (3.3)$$

where the $\text{mod}(\cdot, \cdot)$ operation denotes the remainder of the first argument divided by the second one. The coefficients $a_{i,\text{PRBS}} \in \{0, 1\}, i = 1, \dots, n_{\text{PRBS}}$ can be chosen in such a way that the maximum amount of different signal points M is generated, see [25, p. 420]. The initial values $s(j), j = -1, -2, \dots, -n_{\text{PRBS}}$ can be chosen arbitrarily but not all equal to zero. With respect to the clock period P_{PRBS} , the time domain signal is given by

$$u_{\text{PRBS}}((P_{\text{PRBS}}k + i)T_s) = A_{\text{PRBS}} \left(s_{\text{PRBS}}(k) - \frac{1}{2} \right), \quad i = 0, \dots, P_{\text{PRBS}} - 1, \quad k = 0, \dots, 2^{n_{\text{PRBS}}} - 2, \quad (3.4)$$

where A_{PRBS} is the amplitude of the signal and T_s denotes the sampling time. Calculated over one period, this signal does not have a mean value of exactly zero, however, with rising length M , it converges towards zero. This has to be kept in mind as it will lead to a position drift when the signal is applied to the system in an open-loop identification. The influence of the parameters n_{PRBS} and P_{PRBS} on the time domain can be seen in Figure 3.1 and their corresponding continuous frequency spectra are depicted in Figure 3.2.

According to (3.3) and (3.4), the reciprocal value of the shortest time between two value changes gives the first zero of the spectrum at

$$f_{\text{PRBS},\text{max}} = \frac{1}{P_{\text{PRBS}}T_s} \quad (3.5)$$

and the reciprocal value of the whole sequence time gives the lowest frequency of the spectrum

$$f_{\text{PRBS},\text{min}} = \frac{1}{(2^{n_{\text{PRBS}}} - 1)P_{\text{PRBS}}T_s}, \quad (3.6)$$

see [29, p. 230ff]. Between these frequencies, the system is excited properly for system identification. However, the upper bound in the frequency range only marks the first zero in the frequency spectrum of the **PRBS**. Therefore, this bound is only a soft one, whereas the

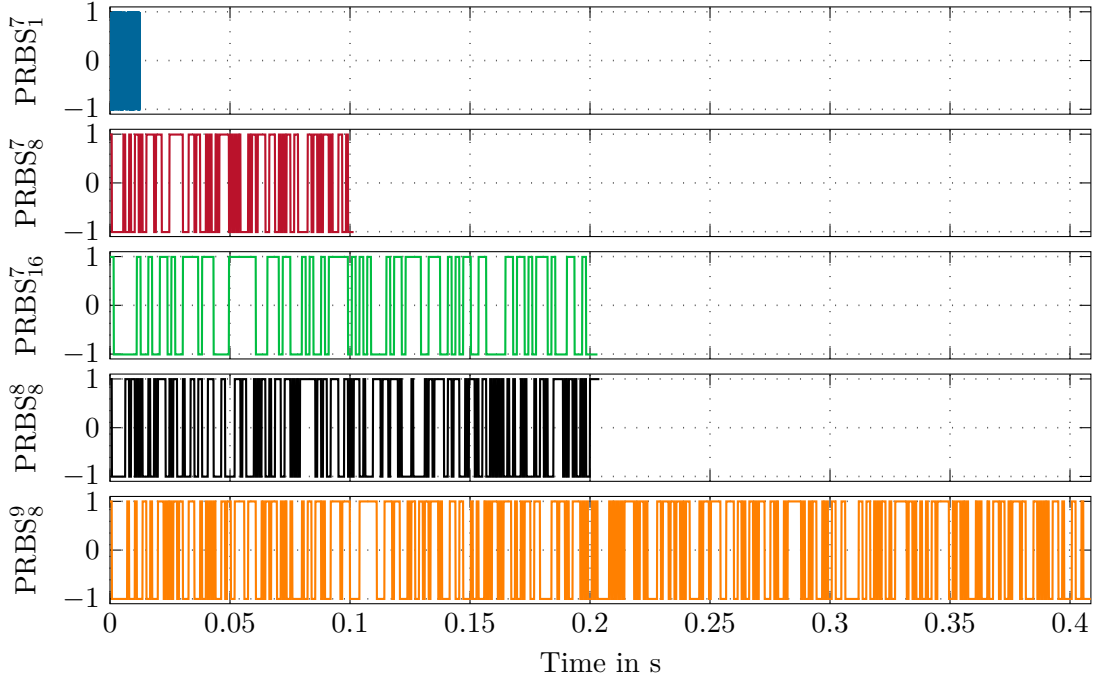


Figure 3.1: One full period of each **PRBS** in the time domain for different orders n_{PRBS} and different clock periods P_{PRBS} using a sampling time of $T_s = 100 \mu\text{s}$.

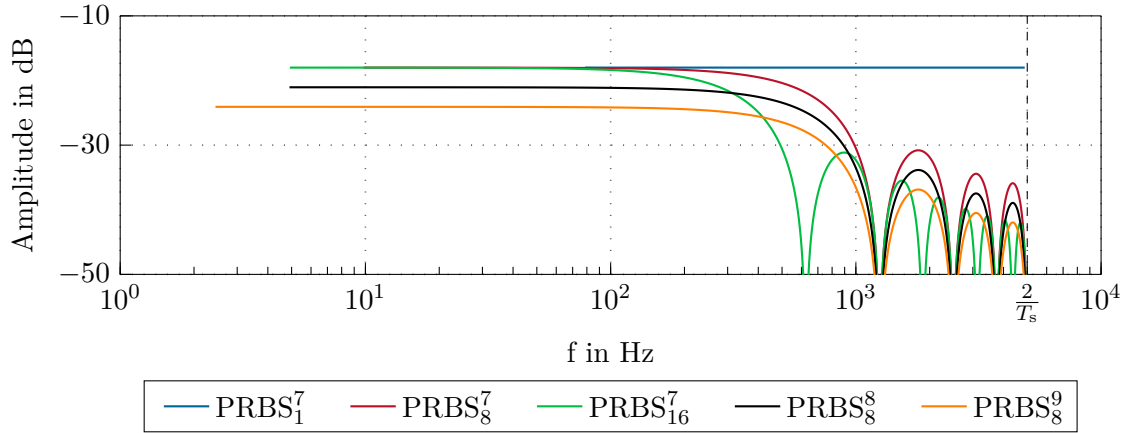


Figure 3.2: **PRBS** in the frequency domain for different orders n_{PRBS} and different clock periods P_{PRBS} using a sampling time of $T_s = 100 \mu\text{s}$.

lower bound is a hard restriction due to the length of the time window $t_{\text{PRBS,max}} = \frac{1}{f_{\text{PRBS,min}}}$ for the Fast Fourier transformation (FFT). When using a generalized pseudorandom binary signal (GPRBS), as presented in [26, p. 172ff], the zero in the frequency spectrum can be avoided at the cost of a smaller spectral power density in the frequency range below. Because the GPRBS uses a random sequence that changes depending on the seed of the random generator, the PRBS is preferred for maintaining repeatable results, see Section 3.4.

3.2 Empirical transfer function estimate

It can be shown that an estimate for the transfer function $G_{u,y}(z)$ is given by the ratio of the spectra of the input signal u_k and the output signal y_k of a system, see [25] and [24]. Here, $z = e^{j\omega T_s}$ denotes the time-discrete Laplace variable, j is the complex number, T_s is the sampling time and ω represents the frequency. This estimate

$$\hat{G}_{u,y}(e^{j\omega T_s}) = \frac{\mathcal{F}\{y_k\}}{\mathcal{F}\{u_k\}} \quad (3.7)$$

is called empirical transfer function estimate (ETFE) because linearity is preassumed. Here, $\mathcal{F}\{\cdot\}$ denotes the FFT of the argument. From (2.39) it is known that the system exhibits an integrating behavior. Using Clary's method II, see [30], this a priori knowledge can be utilized so that only the unknown remaining transfer function has to be estimated. A block diagram explaining Clary's method II is given in Figure 3.3. Within Clary's method II, the system with transfer function $G_{u,y}(z)$ is split up into a known part $\frac{z_b(z)}{n_b(z)}$ and an unknown part $G_i(z)$, i. e.,

$$G_{u,y}(z) = \frac{z_b(z)}{n_b(z)} G_i(z). \quad (3.8)$$

In the problem at hand we can measure the input torque

$$u_k = \tau_{i,k} \quad (3.9)$$

and the output motor angle

$$y_k = \varphi_{m,k}. \quad (3.10)$$

Moreover, the integrating behavior is known, i. e.,

$$\frac{z_b(z)}{n_b(z)} = \frac{z}{z-1}, \quad (3.11)$$

and unknown is the transfer function

$$G_i(z) = G_{\tau_i, \omega_m}(z). \quad (3.12)$$

It is easy to show that prefilters in the form

$$V_1(z) = 1 \quad (3.13)$$

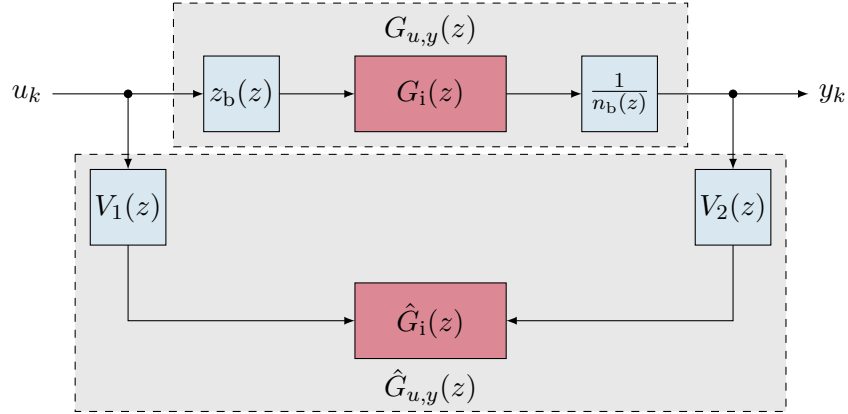


Figure 3.3: Clary's method II using a priori knowledge of the system.

and

$$V_2(z) = \frac{z-1}{z} \quad (3.14)$$

allow a proper estimate of the transfer function $G_{\tau_i, \varphi_m}(z)$ because

$$\hat{G}_{\tau_i, \varphi_m}(z) = \frac{V_2(z) \hat{y}(z)}{V_1(z) \hat{u}(z)} = \frac{z-1}{z} \hat{G}_{\tau_i, \omega_m}(z). \quad (3.15)$$

3.3 Identification strategies

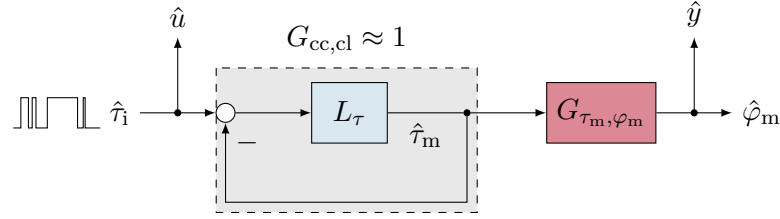
Within the offline identification approach using Clary's method II, the plant can be excited in an open- or closed-loop setup, see [6]. In the closed-loop case, a further distinction is made between a direct and an indirect approach. The block diagrams of the individual identification strategies are depicted in Figure 3.4. The input signal used for the identification process is denoted by \hat{u} and the output signal by \hat{y} . In order to keep the presentation short, the dependency of the transfer functions on the Laplace variable is omitted in the following. The calculation of the motor angular velocity ω_m from the motor angle φ_m is assumed to be performed by a known filter with transfer function G_R , see Section 6.1.

All approaches use an inner current controlled loop consisting of a current controller with transfer function C_τ and the electrical subsystem with transfer function G_{i_m, τ_m} from the motor current i_m to the motor torque τ_m . The respective open-loop transfer function is given by

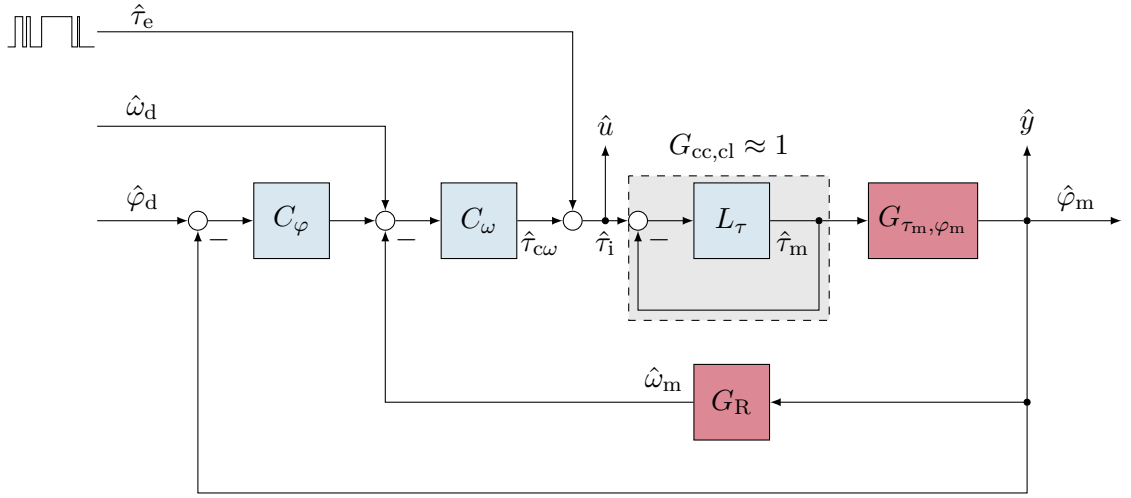
$$L_\tau = C_\tau G_{i_m, \tau_m}. \quad (3.16)$$

The closed-loop transfer function of this control loop reads as

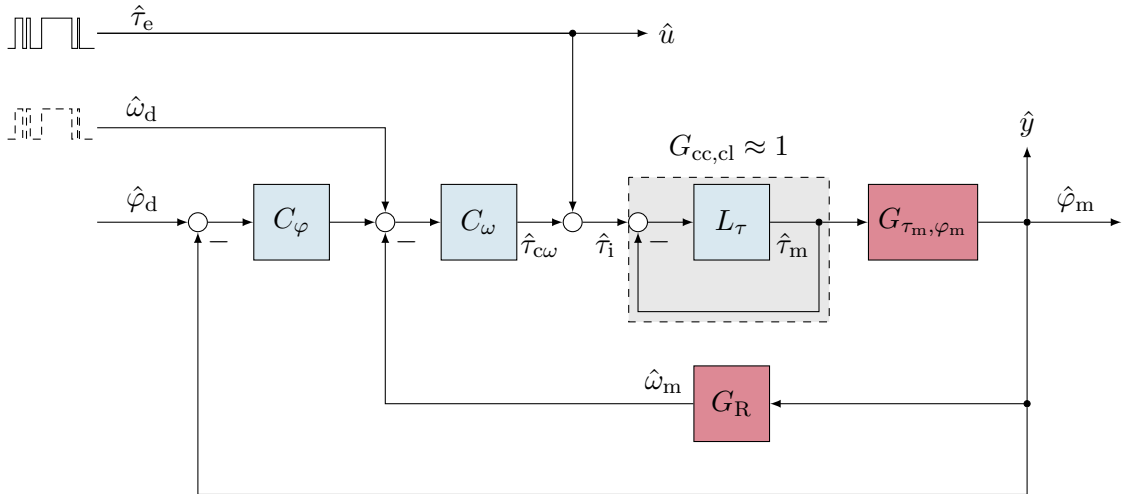
$$G_{cc,cl} = \frac{L_\tau}{1 + L_\tau} \approx 1. \quad (3.17)$$



(a) Schematic diagram: Open-loop identification.



(b) Schematic diagram: Direct closed-loop identification.



(c) Schematic diagram: Indirect closed-loop identification.

Figure 3.4: Open-loop, direct closed-loop and indirect closed-loop identification exemplified as schematic control circuits. The identification process uses \hat{u} as an input and \hat{y} as an output of the system.

The approximation made is valid if the current controlled loop has a high bandwidth compared to the mechanical frequencies of the plant with transfer function G_{τ_m, φ_m} .

In the open-loop identification approach, neither the velocity nor the position of the cart is controlled, cf. Figure 3.4(a). This results in a direct applicability of Clary's method II, as presented in Section 3.2. In the direct and indirect closed-loop approach, the identification uses signals obtained from a closed-loop experiment. The direct closed-loop approach uses the plant input $u = \tau_e + \tau_{c\omega}$ as an input for identification. This includes the control input $\tau_{c\omega}$ of the outer control loops and the excitation signal τ_e , see Figure 3.4(b). Here and in the following, the outer control loop refers to a velocity controller with transfer function C_ω and an optional position controller with transfer function C_φ . The indirect closed-loop identification uses the excitation signal $u = \tau_e$ as an input for the identification process without the control part of the outer control loops, cf. Figure 3.4(c). This results in an estimation of the sensitivity function of the closed control loop. However, the influence of the outer control loops can be eliminated mathematically because the transfer function of the used controllers are known.

In contrast to the open-loop approach, the closed-loop approaches need to take into account the active outer control loops, because the excitation signal acts via the input disturbance transfer function on the measured output, thus reducing the signal to noise ratio (SNR) of the output signal and, hence, affecting the identification results. However, the closed-loop identification scenarios provide the advantage of identifying the system at operating points where $\dot{\xi} \neq 0$, hence, minimizing the nonlinear friction effects on the estimation results. The downside of these approaches is that a controller for the unknown system has to be available.

The following sections deal with the open- and closed-loop, non-parametric identification of the FRF of the toothed linear belt drive.

3.3.1 Open-loop identification

The system is excited with a motor torque $\tau_1 \approx \tau_m$ and responds with a motor angle φ_m . Applying Clary's method II results in

$$\hat{G}_{\tau_m, \varphi_m} = \frac{V_2 \hat{\varphi}_m}{V_1 \hat{\tau}_m} \approx \frac{z-1}{z} G_{\tau_m, \omega_m}. \quad (3.18)$$

Problematic in the open-loop approach is the fact that the system is uncontrolled. If the situation of installation is vertical for instance, i.e., $\alpha = \frac{\pi}{2}$, the cart may hit the limit stops when the system is excited by a PRBS. In order to identify the system in such a case, either a closed-loop approach with active velocity controller and an optional position controller is needed, or the gravitational force f_g needs to be compensated by an offset in the motor torque.

3.3.2 Closed-loop identification

Identification in a closed-loop manner allows to compensate the influence of the gravitation and allows to impress a desired velocity of the cart in order to minimize the nonlinear

friction effects on the identification results. In fact, a high performance controller is counterproductive because the excitation signal acts like an input disturbance, hence, via the sensitivity transfer function

$$S = \frac{G_{\tau_m, \varphi_m} G_{cc, cl}}{1 + G_{\tau_m, \varphi_m} G_{cc, cl} C_\omega (G_R + C_\varphi)}, \quad (3.19)$$

cf. Figure 3.4(b) and Figure 3.4(c). For the closed-loop approach, the velocity signal ω_m needs to be calculated from the incremental encoder position signal φ_m , which is denoted by the transfer function G_R . The realization of this filter is discussed in Section 6.1.

With the controller transfer functions in the denominator of the sensitivity transfer function S , the gain of the controller directly influences the measurable output according to the excitation signal τ_e . Hence, a high gain controller reduces the SNR of the measurement signals used by the identification. However, if it is assumed that the controller already exists, it is possible to identify the system at operating points where $\omega_m \neq 0$ and $\dot{\xi} \neq 0$. In this case, the influence of the nonlinear Coulomb friction on the identification process does not play a role if the velocities of the cart and the motor do not cross zero during the identification procedure. As a consequence of this restriction, the desired velocity must be high enough to fulfill this condition. Contrary to this, the velocity should be as small as possible in order to keep the influence of the position on the identification results small.

Direct closed-loop identification

The direct closed-loop identification approach uses the input signal $u = \tau_i$ and the output signal $y = \varphi_m$ of the plant to estimate the FRF. As depicted in Figure 3.4(b), the system is operated in closed loop and the excitation signal τ_e acts as disturbance on the input of the current control loop. The influence of the superimposed control loops is eliminated by using the actual values of the system input τ_i instead of the excitation signal τ_e . Contrary to this, the indirect closed-loop identification uses only the excitation signal $u = \tau_e$ without the control part.

Indirect closed-loop identification

Additionally to the direct closed-loop approach, it is possible to estimate the closed-loop sensitivity transfer function

$$S = \frac{G_{\tau_m, \varphi_m}}{1 + G_{\tau_m, \varphi_m} C} \quad (3.20)$$

from the input $u = \tau_e$ to the output $y = \varphi_m$ with a known controller transfer function C , cf. Figure 3.4(c). Depending on the active superimposed control loops, the controller influence C is given by

$$C = \begin{cases} G_R C_\omega & \text{with velocity controller,} \\ (G_R + C_\varphi) C_\omega & \text{with position and velocity controller,} \end{cases} \quad (3.21)$$

where C_φ denotes the transfer function of the position controller and C_ω the transfer function of the velocity controller. In the single input single output (SISO) case, this equation can be solved explicitly for the unknown transfer function

$$G_{\tau_m, \varphi_m} = \frac{S}{1 - SC}. \quad (3.22)$$

Alternatively, the excitation signal can be applied at the output of the position controller, i.e., at the input ω_d , cf. Figure 3.4(c). This introduces an additional filtering of the excitation signal by the velocity controller. In this case, the excitation can be too small in the interesting frequency range leading to a low SNR. Moreover, in this case, the transfer function

$$S_{\omega_d} = \frac{G_{\tau_m, \varphi_m} C_\omega}{1 + G_{\tau_m, \varphi_m} C} \quad (3.23)$$

gives the input-output relation and (3.22) needs to be replaced by

$$G_{\tau_m, \varphi_m} = \frac{S_{\omega_d}}{C_\omega - S_{\omega_d} C}. \quad (3.24)$$

with the relationship for C from (3.21). Note that (3.20) and (3.23) differ in the multiplicative transfer function C_ω . Because of the mentioned additional filtering of the excitation signal by the velocity controller, the approach without additional filtering of the excitation signal is preferred in this diploma thesis.

3.4 Identification results

For the open-loop ETFE, a PRBS₁₂₈⁷ and for the closed-loop ETFE a PRBS₆₄⁷ is used as excitation signal. Moreover, all closed-loop identification results presented here utilize a closed velocity control loop with desired velocity $i_t \omega_d = \dot{\xi}_d = 100 \text{ mm/s}$. Note that in the closed-loop identification, the excitation signal clock period P_{PRBS} is chosen smaller than in the open-loop case. That is, the clock period P_{PRBS} of the excitation signal is reduced to half of its value in comparison to the one used in the open-loop approach. The reduction of the signal clock period is performed in order to minimize the influence of the position-dependency of the parameters on the identification results. Because the closed-loop identification is performed with $\dot{\xi} \neq 0 \text{ m/s}$, the position-dependent parameters get averaged over the position range covered during the identification procedure.

The amplitude of the excitation signal needs to fulfill two conditions. The amplitude of the excitation signal must be chosen large enough to overcome the static friction. However, if chosen too large, the position-dependency of the parameters affects the identification results and in the worst case, the cart may hit the axis limits. In order to yield an appropriate value for the amplitude of the excitation signal, the amplitude is increased successively, starting from zero. This allows to select the amplitude of the excitation signal regardless of the additional mass m_c mounted on the cart, while maintaining a

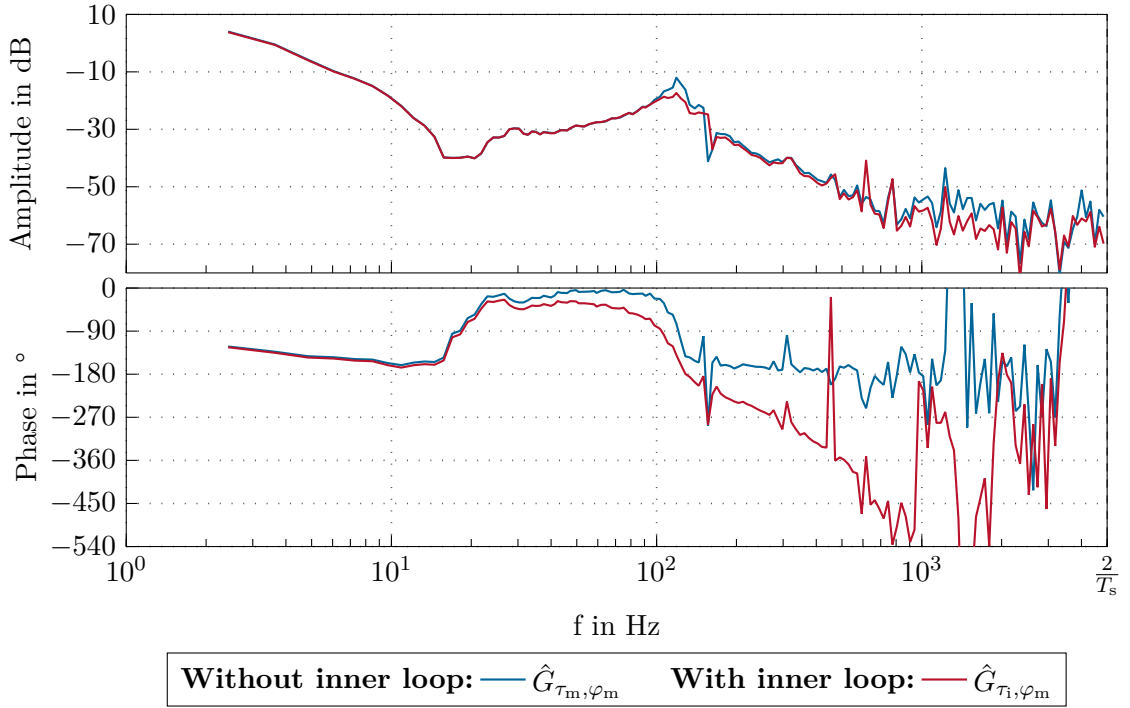


Figure 3.5: Influence of the current control loop on the direct ETFE utilizing Clary's Method II when using the actual torque τ_m as input of the identification process leading to $\hat{G}_{\tau_m, \varphi_m}$ or using the desired torque τ_i resulting in $\hat{G}_{\tau_i, \varphi_m}$. Measurements were taken at position $\xi = 500$ mm and an additionally mounted mass of $m_c = 11.2$ kg on the cart. The system parameters $G_{\mathcal{A}}$ are listed in Table A.4 in Appendix A.

sufficient SNR for the identification procedure. Hence, the amplitude of the excitation signal for the experiments is chosen as $A_{\text{PRBS}} = 0.3$ N m.

If, in the open-loop identification approach, instead of $\hat{u} = \hat{\tau}_m$, the input $\hat{u} = \hat{\tau}_i$ is selected, the influence of the closed current control loop can be evaluated. Figure 3.5 shows the corresponding estimated transfer functions $\hat{G}_{\tau_m, \varphi_m}$ and $\hat{G}_{\tau_i, \varphi_m}$. Obviously, in the considered frequency range the current control loop behaves like a dead time element. In Chapter 4, an appropriate velocity controller is designed, which aims for a closed-loop bandwidth smaller than the antiresonance of the mechanical system, hence, justifying the negligible phase shift, at least for large masses. However, the influence of the current control loop is taken into account by adding a serial dead time element with transfer function

$$G_{\text{dt}} = z^{-n_T}. \quad (3.25)$$

This approximates the response behavior of the closed current control loop with transfer function $\hat{G}_{\text{cc,cl}}$, that is

$$\hat{G}_{\text{cc,cl}} \approx G_{\text{dt}}. \quad (3.26)$$

The dead time $t_T = n_T T_s$ includes the sum of all relevant delays in the closed current control loop, like signal delays due to the time-discrete working principle of the sensors and the current controller, as well as the non-ideality of the current controller itself. The dead time can be estimated by solving the minimization problem of the form

$$J_{dt}^* = J_{dt}(n_T^*) = \min_{n_T} \left(\arg(\hat{G}_{\tau_i, \varphi_m}(e^{j\omega T_s})) - \arg(\hat{G}_{\tau_m, \varphi_m}(e^{j\omega T_s})) - \arg(G_{dt}(e^{j\omega T_s}; n_T)) \right)^2 \quad (3.27)$$

in the interesting frequency range, that is in general $0 \leq \omega \leq \omega_r$. Here, G_{τ_m, φ_m} denotes the transfer function from the actual motor torque τ_m , respectively, its corresponding current value i_m multiplied by the motor constant k_m to the actual motor angle φ_m . Moreover, G_{τ_i, φ_m} denotes the transfer function from the input of the current control loop, which equals the excitation torque τ_i , to the actual motor angle φ_m , that is to say

$$G_{\tau_i, \varphi_m} = G_{cc, cl} G_{\tau_m, \varphi_m}. \quad (3.28)$$

Together with the phase of the dead time element

$$\arg(G_{dt}(e^{j\omega T_s})) = -\omega n_T T_s, \quad (3.29)$$

this problem can be solved using standard optimization algorithms. The solution of the minimization problem is given by

$$t_T^* = n_T^* T_s \approx 1 \text{ ms}. \quad (3.30)$$

Further details on solving the minimization problem are given in Section 3.5, where a similar minimization problem is stated for finding the plant parameters. If the dead time is known a priori, it can also be integrated into Clary's method II by adapting the prefilters accordingly. Figure 3.6 indicates that the velocity controller C_ω has a gain crossover frequency below 1 Hz. According to (3.20), this results in little influence of the controller on the identified transfer function above this frequency. This is because

$$G_{\tau_m, \varphi_m} C_\omega \ll 1 \quad (3.31)$$

is valid in the respective frequency range. Also in Figure 3.6, the FRF of the direct and indirect closed-loop identification as well as the open-loop identification are depicted. It can be noted that all three approaches provide nearly similar results. Especially the open-loop and direct closed-loop approach show no significant difference. However, the indirect closed-loop approach shows a bias in the gain for the lower frequency range, compared to the other methods. This results in an error when estimating the moving mass m_c and the damping parameters d_m and d_c . Using the closed-loop identification approaches, the remaining question is how to design the controller C_ω in advance. That is, the controller must not achieve high performance demands, as this reduces the SNR of the measurement signals, while a too weak controller results in a high control error and, thus, in an actual velocity that is significantly different from the desired velocity. If the control error is too large, the condition of no zero crossings in the velocity during the identification can not be guaranteed. Therefore, the open-loop identification method is

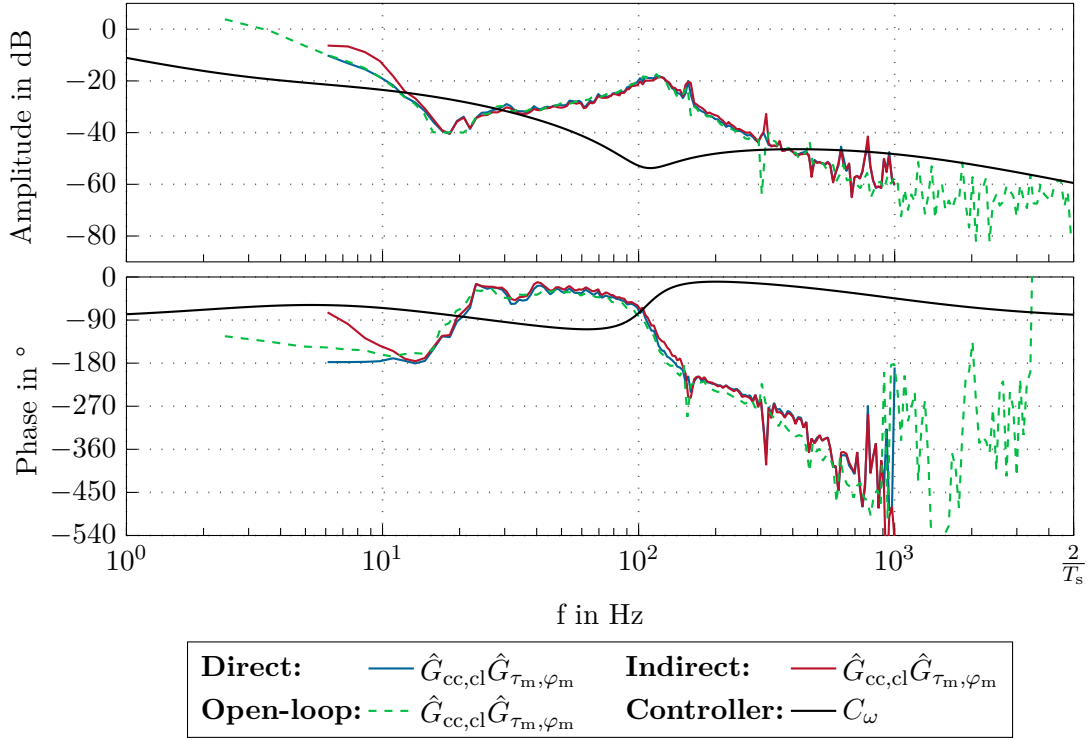


Figure 3.6: Comparison of the FRF acquired by the open-loop approach as well as the direct and indirect method of the closed-loop approach. Additionally, the transfer function of the velocity controller C_ω used within the closed-loop methods is depicted.

preferred for the self-commissioning of the linear toothed belt drive. Nonetheless, this is only possible if the installation angle $\alpha \approx 0$ is assumed. If this condition does not hold, the gravity force f_g needs to be compensated by an additional motor torque $\tau_m = i_t f_g$, as suggested in Chapter 7.

Figure 3.7 depicts the FRF in the frequency range above 500 Hz. Obviously, the SNR becomes worse with rising frequency. Assuming the disturbance can be characterized as additive white Gaussian noise (AWGN), the influence of the noise can be reduced by using the central limit theorem [31, p. 94ff]. The measurements can be repeated n_m -times and calculating the mean values in the frequency domain leads to an increased SNR by a factor $\sqrt{n_m}$. Especially the phase response for frequencies above the resonance frequency ω_r benefits from this increase in SNR, which allows for better identification results of the dead time t_T .

3.5 Parameter fitting

The transfer function (2.42) shows six independent parameters, namely the mass moment of inertia Θ_e , the cart mass m_c , the belt stiffness c , the transmission ratio i_t and the

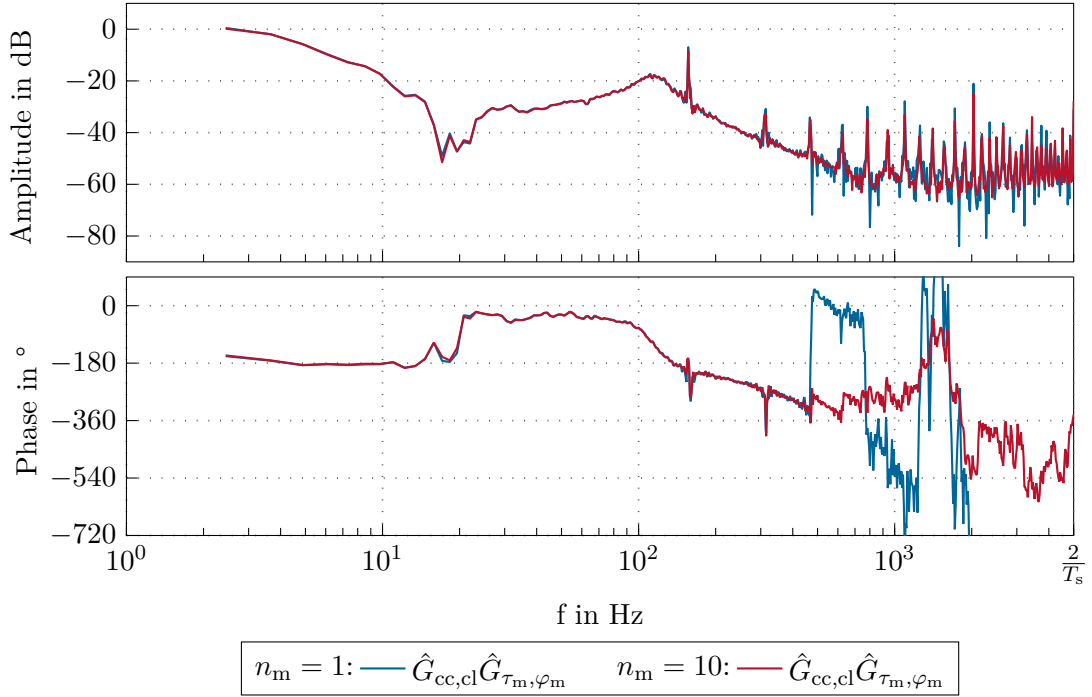


Figure 3.7: Improvement of the SNR by averaging the FRF measurement $n_m = 10$ times.

damping coefficients d_m and d_c . The feedback and feedforward controller, which will be designed in Chapter 4, rely on the continuous-time representation of the transfer function (2.42). Hence, the parameters of (2.42) have to be identified. In the following, it is assumed that the mass moment of inertia Θ_e of the motor, the gear box and the coupling in between as well as the transmission ratio i_t are known from the data sheets with sufficient accuracy. This is why only the parameters collected in the parameter vector

$$\mathbf{p}^T = [m_c \quad c \quad d_m \quad d_c] \quad (3.32)$$

are identified in the following. For this reason, a least squares problem is defined and solved, which utilizes the magnitude of the estimated FRF. This can be interpreted, according to [25, p. 230], as a maximum likelihood estimation under assumption of a fixed noise model. The phase information of the FRF remains disregarded in the optimization problem, as the system with transfer function G_{τ_m, φ_m} is supposed to be of minimum phase. Hence, the phase provides no additional information. Given n_o distinct frequencies $f_i \in F_o$ of the measured FRF and the corresponding magnitude values $|\hat{G}_{\tau_m, \varphi_m}(12\pi f_i)|$, the parameters \mathbf{p} of the mathematical model $G_{\tau_m, \varphi_m}(12\pi f_i; \mathbf{p})$ from equation (2.42) are determined by minimizing the cost function

$$J(\mathbf{p}) = \sum_{i=1}^{n_o} \left(20 \log |\hat{G}_{\tau_m, \varphi_m}(12\pi f_i)| - 20 \log |G_{\tau_m, \varphi_m}(12\pi f_i; \mathbf{p})| \right)^2 \quad (3.33)$$

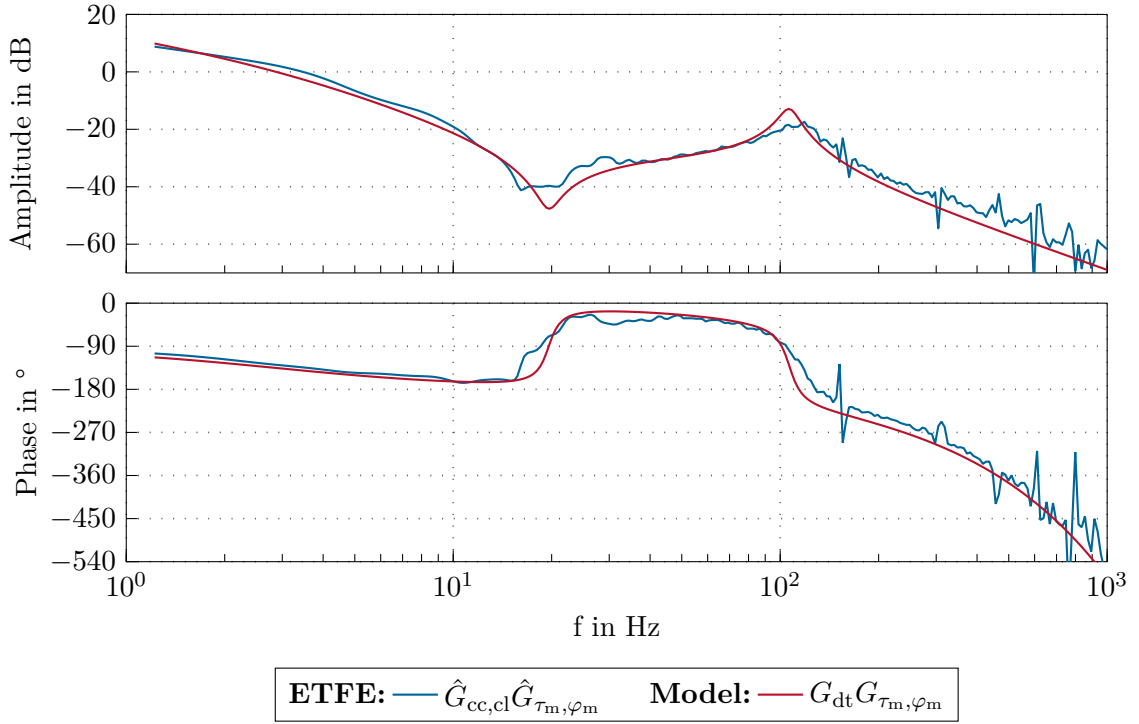


Figure 3.8: Comparison of the **ETFE** raw data $\hat{G}_{cc,cl}\hat{G}_{\tau_m,\varphi_m}$ of an open-loop identification experiment using an additional mass of $m_c = 11.2$ kg and the fitted parametric model $G_{dt}G_{\tau_m,\varphi_m}$ according to the minimization problem (3.34) including the dead time element G_{dt} for the closed current control loop $G_{cc,cl}$ at the cart position $\xi = 500$ mm.

with respect to the parameters \mathbf{p} . The best set of parameters \mathbf{p}^* regarding this cost function is then given by the solution of the minimization problem

$$J^* = J(\mathbf{p}^*) = \min_{\mathbf{p}}(J), \quad (3.34)$$

which can be solved with static optimization algorithms such as the Levenberg-Marquard algorithm [32–34], trust region reflective [35, 36], or derivative-free algorithms, i. e., the Nelder-Mead algorithm [37]. The resulting parameters \mathbf{p}^* of the model given by (2.42) can then be used to plot the frequency response of the parametrized model. Figure 3.8 compares the **FRF** of the fitted model $G_{dt}G_{\tau_m,\varphi_m}$ to the **FRF** of $\hat{G}_{cc,cl}\hat{G}_{\tau_m,\varphi_m}$ acquired by the **ETFE**.

The estimated **FRF** is based on a data sequence in the time domain consisting of n_t data points sampled with a sampling time of T_s . The **FRF** itself consists of $n_f = |F| = \lfloor \frac{n_t}{2} \rfloor^1$ evenly distributed data points in the frequency domain starting from $f_{\min} = \frac{1}{n_t T_s}$ up to $f_{\max} = \frac{2}{T_s}$. In order to reduce the computational effort to solve the static optimization problem (3.33) and to compensate for the logarithmic frequency scaling of the **FRF**, the

¹ $|\cdot|$ denotes the cardinality of a set and $\lfloor \cdot \rfloor$ denotes the integer floor operation.

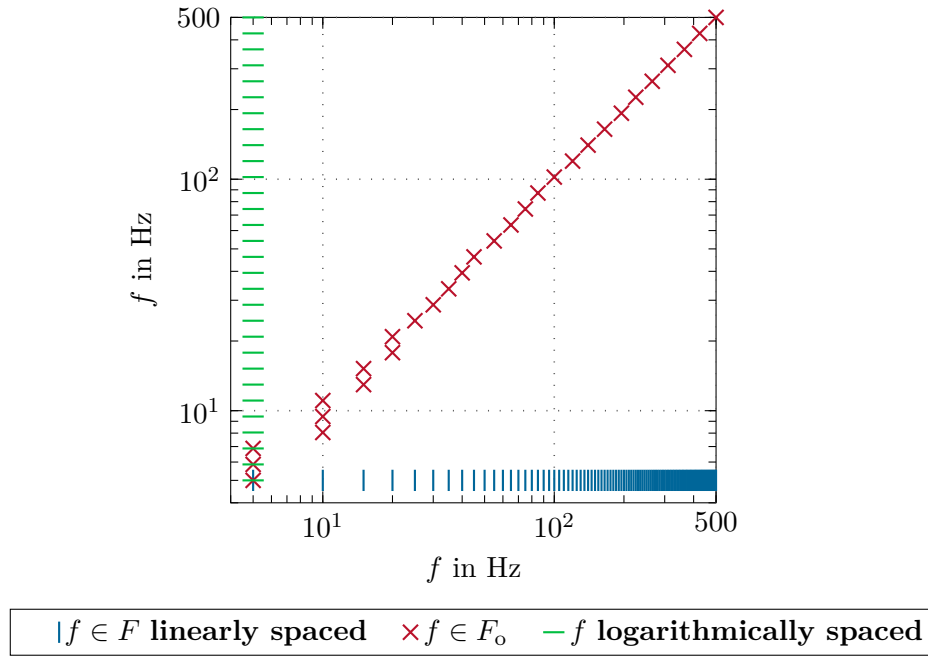


Figure 3.9: Illustration of the data reduction from linear frequency spacings in the set F to nearly logarithmically spacings in the subset F_o . Parameters: $n_o = 30$, $n_f = 100$, $f_{\min} = 5$ Hz, $f_{\max} = 500$ Hz.

data points in the frequency domain are reduced to $n_o = |F_o| < n_f$ nearly logarithmically spaced data points. The n_o reduced data points are included in the set of linearly spaced frequencies, e. g., $F_o \subset F$. This relationship is illustrated in Figure 3.9. Note that the logarithmic spacing acts like a weighting function which puts more weight on lower frequencies and less weight on higher ones.

3.6 Friction identification

This section is devoted to friction estimation and analysis. In order to reduce the effect of the nonlinear friction on the positioning control performance, a feedforward controller will be designed in Section 4.4. This controller is based on the friction models (2.21) and (2.23), hence, this friction model must be parametrized. In typical applications, the cart position cannot be measured. Due to this, we will assume in the following that the coupling between the motor and cart is rigid, i. e., $c = 0$ and $d = 0$. Consequently, the equations (2.25) reduce to

$$(\Theta_e + m_c i_t^2) \dot{\omega}_m = \tau_m + \tau_{mR} + i_t f_g + i_t f_R. \quad (3.35)$$

If we assume a constant velocity, i. e., $\dot{\omega}_m = 0$, and a horizontal situation of installation, $f_g = 0$, (3.35) allows to measure the friction torque, because

$$\tau_m = \tau_R(\omega_m) = -\tau_{mR} - i_t f_R = \underbrace{(d_m + i_t^2 d_c)}_{\tilde{d}_v} \omega_m + \underbrace{(\tau_c + i_t f_c)}_{\tilde{\tau}_c} \text{sign}(\omega_m) \quad (3.36)$$

holds true. Using a position controller and a periodic triangular-shaped reference position allows to force a constant velocity over a period. Different velocities are set for different periods of time with a certain running-in-time to assure a constant velocity. With the measured torque, the parameters \tilde{d}_v and $\tilde{\tau}_c$ are obtained by solving a least squares problem.

The measured torque τ_m and the mathematical model $\tau_R(\omega_m)$ with fitted parameters are depicted in Figure 3.10. The picture shows six sets of measurement data which differ in the acquisition order of their corresponding data. The data set τ_m^I represents a measurement starting from lowest velocities $\omega_m \approx 0$ and increasing the velocity steadily, whereas τ_m^{II} reverses this sequence. Moreover, τ_m^{III} utilizes an arbitrarily chosen sequence of velocities s_ξ given by (A.1) in Appendix A and τ_m^{IV} represents the average of ten consecutive measurements like the data set τ_m^I . That is, one data point is measured ten times before continuing with the next higher velocity. Dataset τ_m^V is a long term friction measurement after approximately nine month of usage, acquired in the same way as τ_m^I . The last measurement data τ_m^{VI} equals τ_m^V with an additional mass of $m_c = 11.2 \text{ kg}$ mounted on the cart. Clearly, the real friction contains dependencies, e. g., on the temperature, the humidity, etc., which are not modeled by (3.36). This explains the variance of the measured friction curves. Besides the Coulomb friction, a small Stribeck effect can be observed around zero velocity.

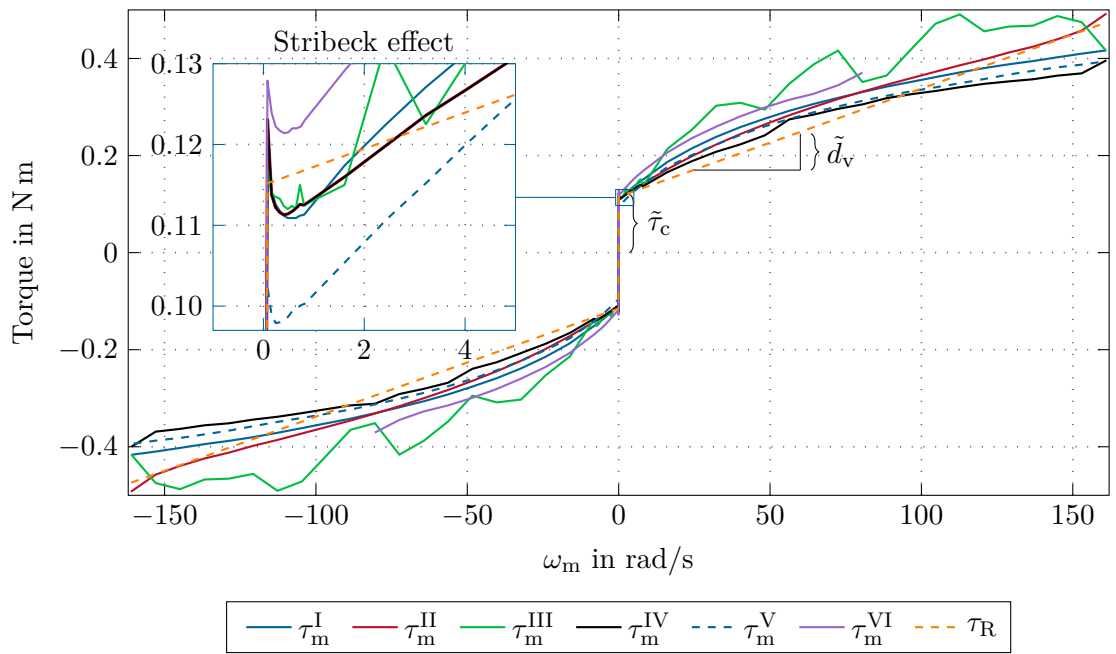


Figure 3.10: Measured torque using different measurement scenarios and fitted friction torque model.

4 Control strategies

The previous chapter shows the identification and validation of the mathematical model derived in Chapter 2. This parametrized model will be used in this chapter to design an appropriate control loop. The current controlled plant, given by the result of the identification process from Chapter 3, acts as target plant for which the control loop has to be designed. In [3], [5] and [11] it was shown that linear belt driven servo mechanisms can be controlled by linear control loops and can achieve sufficient performance. These control strategies utilize typically a PID control structure or a cascaded P-PI control structure with an inner velocity control loop and a superimposed position control loop. This concept is successfully used in industry for many years. The first section of this chapter deals with an overview of the used control strategy, whereas the following section focuses on the design of the inner PI-velocity control loop. Based on the closed velocity control loop, the position control loop is designed in the next section. The last section deals with the feedforward controller design.

4.1 Control structure

The proposed control strategy is depicted in Figure 4.1. The control design is based on the parametric model of the plant given by the transfer function G_{τ_m, φ_m} and the closed current control loop, described by the transfer function G_{dt} . The velocity feedback controller

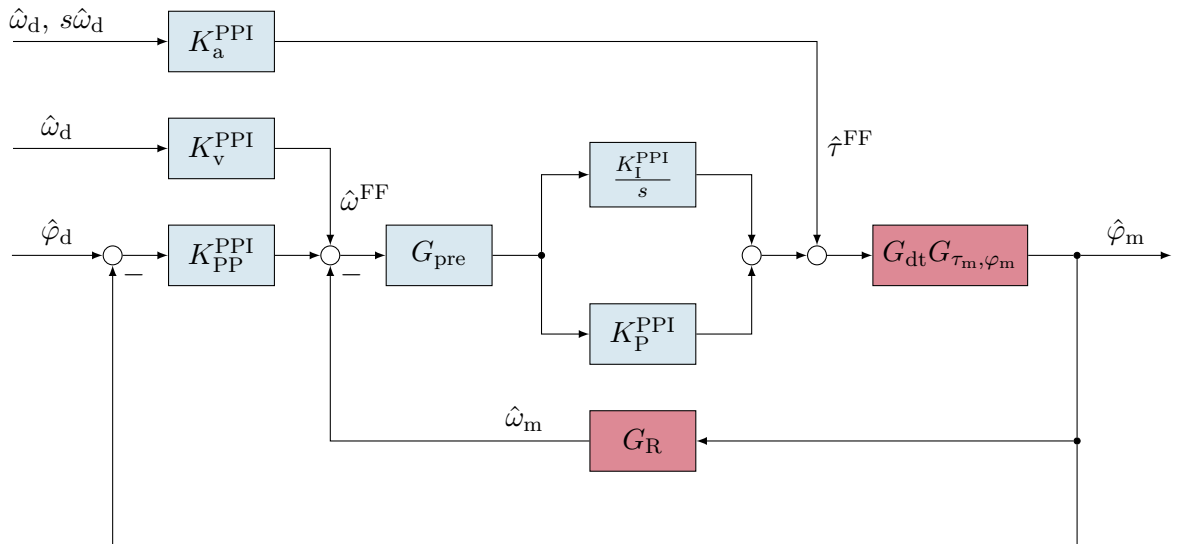


Figure 4.1: Block diagram of the control strategy.

consists of a prefilter with transfer function G_{pre} to dampen the mechanical resonance of the plant and a PI-velocity-controller C_ω with respective tuning parameters $K_{\text{I}}^{\text{PPI}}$ and $K_{\text{P}}^{\text{PPI}}$. The outer P-position control loop, with the respective tuning parameter $K_{\text{P}}^{\text{PPI}}$, is superimposed to the closed velocity control loop. The feedforward controller $K_{\text{a}}^{\text{PPI}}$ and $K_{\text{v}}^{\text{PPI}}$ compensates for the friction and the moving mass, see Section 4.4.

4.2 Velocity controller design

The parametric model $G_{\tau_{\text{m}}, \varphi_{\text{m}}}$ from (2.42) serves as a basis for the velocity controller design. This model was parametrized in Chapter 3 by solving the minimization problem (3.34). The plant for the controller design consists of a serial connection of the identified electromechanical system $G_{\tau_{\text{m}}, \varphi_{\text{m}}}$, given by (2.42), and a dead time element G_{dt} given by (3.25). The velocity signal is calculated from the position signal via the transfer function G_{R} , see Section 6.1. The input limits are not explicitly regarded in the controller

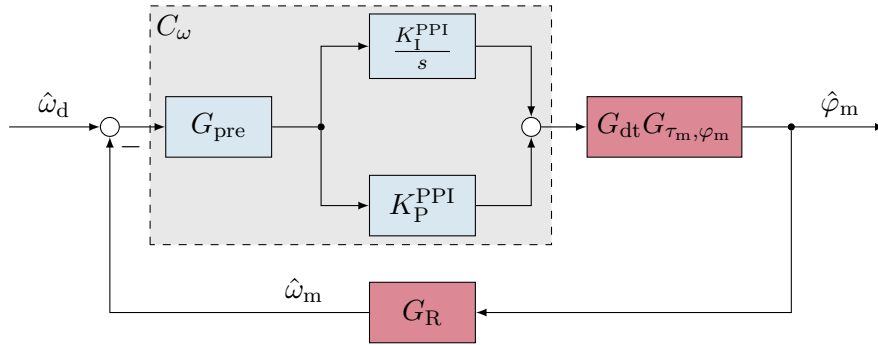


Figure 4.2: Block diagram of the velocity control loop.

design. However, they can be systematically taken into account by the trajectory generator presented in Section 6.3. First, in Section 4.2.1 a prefilter is designed to dampen the mechanical resonance of the plant. Hereby, two different filters are discussed in detail. The next section, Section 4.2.2, deals with the PI-velocity-controller design.

4.2.1 Prefilter design

The mechanical resonance of the plant is suppressed by adding an additional filter G_{pre} in the velocity control loop. Without this prefilter, the mechanical resonance limits the controller performance, see Section 5.1, or even worse, causes instability. This can either be done by a low-pass filter of appropriate cutoff frequency or by filtering the resonance frequency with a Notch filter.

Notch filter design

If perfect model knowledge is assumed, the Notch filter can compensate for the mechanical resonance in the transfer function (2.42). However, the plant parameters will change with time by wearing and aging, as well as with the position ξ , cf. Figure 2.4. Henceforth,

the Notch filter is designed to suppress the worst case mechanical resonance with limited influence on the plant below the antiresonance frequency ω_z . This worst case scenario occurs if the mass m_c is largest and the belt stiffness coefficient c is smallest, meaning that the cart is in the position farthest away from the driven end of the linear axis. The transfer function of the Notch filter, see [38], is given by

$$G_{\text{Notch}} = \frac{s^2 + 2\frac{1}{d_n}\omega_{r,N}s + \omega_{r,N}^2}{s^2 + 2d_n\omega_{r,N}s + \omega_{r,N}^2}, \quad (4.1)$$

where d_n is the design parameter for the frequency range over which the Notch is active and $\omega_{r,N}$ denotes the center frequency of the stopband. Because the worst case mechanical resonance of the plant is identified to occur at frequency ω_r , the center frequency of the Notch filter is fixed at $\omega_{r,N} = \omega_r$. Supposing the antiresonance frequency ω_z of the plant marks a lower bound on the desired influence of the Notch or a possible low-pass filter, the filter influence should not undergo frequencies below ω_z in a significant manner. Otherwise, the achievable bandwidth of the closed velocity control loop will suffer. As shown in Figure 2.8, the stopband of the Notch has to be adapted to the resonance ratio κ , that is, for small resonance ratios the stopband has to be narrower than for high values of κ . Regarding this condition, the amplitude attenuation of the Notch at frequency ω_z is required to fulfill the condition

$$|G_{\text{Notch}}(I\omega_z)| = A_{\text{Notch}}, \quad (4.2)$$

with the design parameter $A_{\text{Notch}} < 1$. This relation maintains the connection between the stopband width of the Notch filter and the resonance ratio κ of the plant. Moreover, it can be used to determine the design parameter by explicitly solving (4.2) for d_n . For shorter linear axis this is sufficient, as the drift of the resonance frequency ω_r is limited, cf. Figure 2.9, and the achievable bandwidth does not suffer significantly by choosing the worst case scenario as design reference.

Butterworth filter design

Another approach of filtering the mechanical resonance frequency of the plant is a second order Butterworth filter, see [39], given by the transfer function

$$G_{\text{bw}} = \frac{1}{\frac{s^2}{\omega_{\text{bw}}^2} + \sqrt{2}\frac{s}{\omega_{\text{bw}}} + 1}, \quad (4.3)$$

with cutoff frequency ω_{bw} . Analogously to (4.2), the influence of the filter on frequencies below ω_z has to be limited, which is achieved by the condition

$$|G_{\text{bw}}(I\omega_z)| = A_{\text{bw}}, \quad (4.4)$$

with the design parameter $A_{\text{bw}} < 1$. The cutoff frequency ω_{bw} in (4.3) is determined by (4.4) and the design parameter A_{bw} .

In Figure 4.3, the frequency response of the Notch filter (4.2) with $\omega_{r,N} = \omega_r$ and $A_{\text{Notch}} = -6$ dB and the second-order low-pass (4.3) with $A_{\text{bw}} = -3$ dB are depicted in

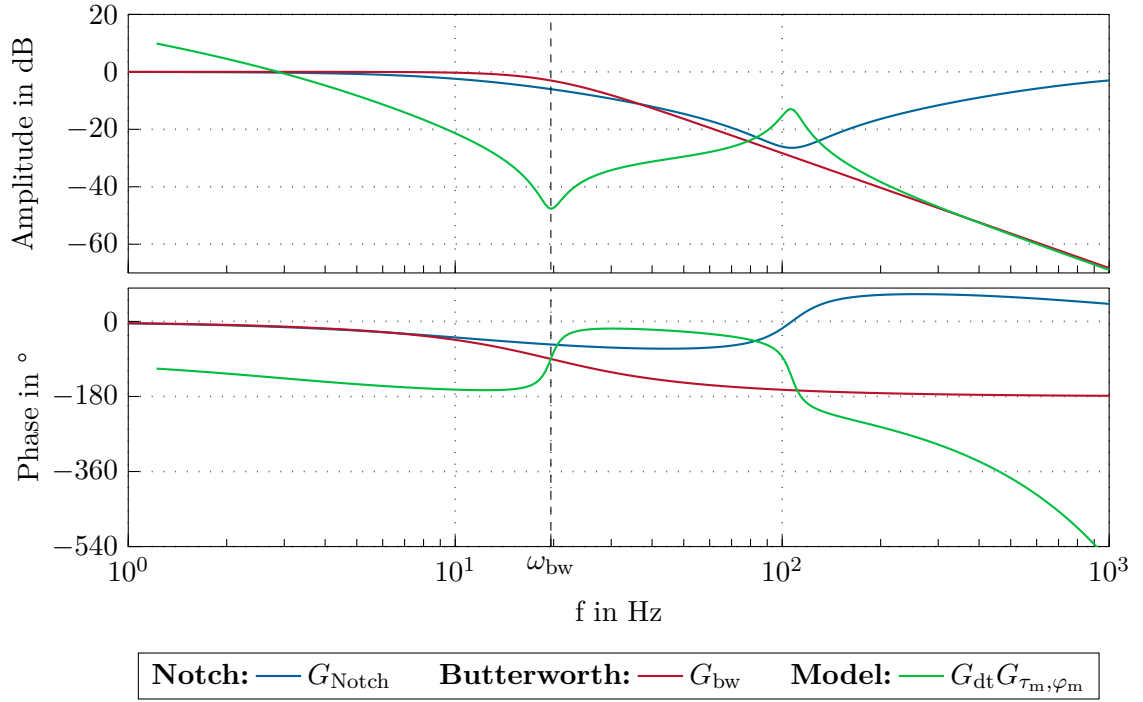


Figure 4.3: Transfer function of a Notch filter, a second-order Butterworth filter and the nominal plant transfer function.

comparison with the identified transfer function $G_{\text{dt}}G_{\tau_m, \varphi_m}$ of the plant. The Butterworth filter shows a better roll-off at the cost of a larger phase shift around its cutoff frequency ω_{bw} . This is especially of interest for stability reasons, as the open-loop gain crossover frequency of the velocity control loop lies in the range of ω_{bw} , see Section 4.2.2. One advantage of the low-pass filter over the Notch filter is that it is very robust against lower masses and/or stiffer connections, which both result in mechanical resonance frequencies of the plant shifted to higher values, see (2.44).

The approach of filtering the mechanical resonance can also be applied to a system with more than one resonance frequencies by filtering the one with the lowest frequency. Resonances above the filtered one are then damped by the sufficient roll-off of the Butterworth filter. In the case of the Notch filter, an additional low-pass filter can be used to add this necessary roll-off for higher frequencies.

4.2.2 PI-controller design

The filter G_{pre} in the form of a Notch filter G_{Notch} or a Butterworth filter G_{bw} , designed in Section 4.2.1, is now added in series to the transfer function of the plant, leading to the velocity control loop depicted in Figure 4.2. For the already determined part of the

open-loop transfer function, the abbreviation

$$G_\omega = G_{\text{pre}} G_{\text{dt}} \underbrace{G_{\tau_m, \varphi_m}}_{\approx G_{\tau_m, \omega_m}} G_{\text{R}} \quad (4.5)$$

is introduced and used to design the PI-controller with the transfer function

$$G_{\text{PI}} = \frac{K_{\text{I}}^{\text{PPI}}}{s} + K_{\text{P}}^{\text{PPI}}. \quad (4.6)$$

Although the filter G_{pre} suppresses the mechanical resonance, it has to be further considered in the controller design. While the controller design parameters $K_{\text{I}}^{\text{PPI}}$ and $K_{\text{P}}^{\text{PPI}}$ can be chosen arbitrarily, the prefilter itself does not guarantee stability of the closed-loop system. That is why a resonance suppression factor A_{sup} is introduced. It guarantees that at the resonance frequency ω_{r} of the plant the gain of the open-loop transfer function of the velocity control loop is smaller than this factor, hence, preventing instability caused by the mechanical resonance. Therefore, the open-loop transfer function has to fulfill the condition

$$|G_{\text{PI}}(\text{I}\omega_{\text{r}})G_\omega(\text{I}\omega_{\text{r}})| \stackrel{!}{=} A_{\text{sup}}, \quad (4.7)$$

with $A_{\text{sup}} < 1$ denoting the resonance suppression factor. For practical implementation, the resonance suppression factor is chosen to be $A_{\text{sup}} = -10$ dB. Additionally to the resonance suppression factor A_{sup} , the phase margin $\varphi_{\text{r}}^\omega$ at the cutoff frequency ω_{c} of the control loop serves as stability measure. The bandwidth of the control loop, or equivalently, the cutoff frequency is defined by

$$|G_{\text{PI}}(\text{I}\omega_{\text{c}})G_\omega(\text{I}\omega_{\text{c}})| = 1, \quad (4.8)$$

where the open-loop gain passes from magnification to attenuation. In order to guarantee stability, the phase margin has to be chosen sufficiently large, see [40]. The phase margin condition

$$\arg(G_{\text{PI}}(\text{I}\omega_{\text{c}})G_\omega(\text{I}\omega_{\text{c}})) \stackrel{!}{=} -\pi + \varphi_{\text{r}}^\omega \quad (4.9)$$

defines the second restriction to the PI controller, hence, both design parameters, $K_{\text{I}}^{\text{PPI}}$ and $K_{\text{P}}^{\text{PPI}}$, are determined. As mentioned in [41, p. 105], an appropriate value for the phase margin is $30^\circ \leq \varphi_{\text{r}}^\omega \leq 60^\circ$. Depending on the real operating conditions and requirements, its actual value remains as design parameter. This allows for an easy detuning or tightening of the control loop. For test purposes, the phase margin is chosen to be 60° , which puts emphasis on the stability of the closed-loop system.

With (4.7), the parameter $K_{\text{I}}^{\text{PPI}}$, and with (4.9), the parameter $K_{\text{P}}^{\text{PPI}}$ of the PI-velocity-controller are fixed. The PI-controller is thus formally completely defined and the position controller can be tuned as the superimposed control loop. However, the conditions (4.7) and (4.9) cannot be solved explicitly for the design parameters $K_{\text{P}}^{\text{PPI}}$ and $K_{\text{I}}^{\text{PPI}}$ of the controller. This is because the crossover frequency, given by (4.8), needs to be calculated as a function of the controller design parameters, which, however, is a nonlinear function

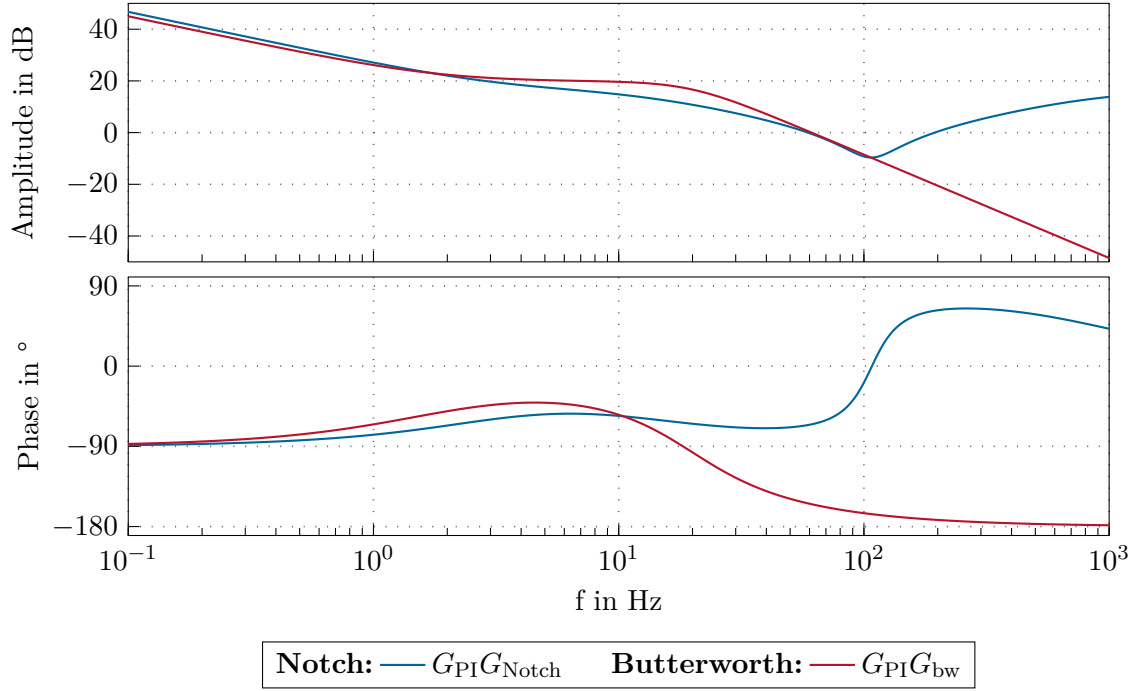


Figure 4.4: Comparison of the velocity control loops based on the Notch filter and the Butterworth filter in the frequency domain. The design parameters of the controllers are given by the parameter sets $C_{\mathcal{A}}$ and $C_{\mathcal{B}}$ in Table A.6 and Table A.7 in Appendix A.

and cannot be solved analytically. In order to calculate the parameters K_P^{PPI} , K_I^{PPI} and ω_c , the equations (4.7), (4.8) and (4.9) can be solved numerically, e. g., using the Newton-Raphson method, see [42]. The Bode diagram of the velocity controller $G_{\text{pre}}G_{\text{PI}}$ for both, filtering the mechanical resonance with $G_{\text{pre}} = G_{\text{Notch}}$ and $G_{\text{pre}} = G_{\text{bw}}$, are depicted in Figure 4.4, where the design parameters $\varphi_r^\omega = 60^\circ$, $A_{\text{sup}} = -10$ dB as well as $A_{\text{Notch}} = -6$ dB and $A_{\text{bw}} = -3$ dB were chosen. The respective open-loop transfer functions of the velocity controlled loop are depicted in Figure 4.5. The desired values of the phase margin are maintained within the solution of the nonlinear equations (4.7), (4.8) and (4.9), however, in case of a Notch prefilter, due to numeric errors, the achieved resonance suppression factor is insignificantly lower than the desired value. Moreover, the crossover frequency is slightly lower than with the Butterworth prefilter. It can be noted that the open-loop transfer functions, when using a Notch or a Butterworth prefilter in the controller design, are comparable to each other, if the same design parameters A_{sup} and φ_r^ω are chosen.

4.3 Position controller design

Based on the designed prefilter in Section 4.2.1 and the velocity controller in Section 4.2.2, a P-position-controller is designed. The schematic diagram of the position control loop is

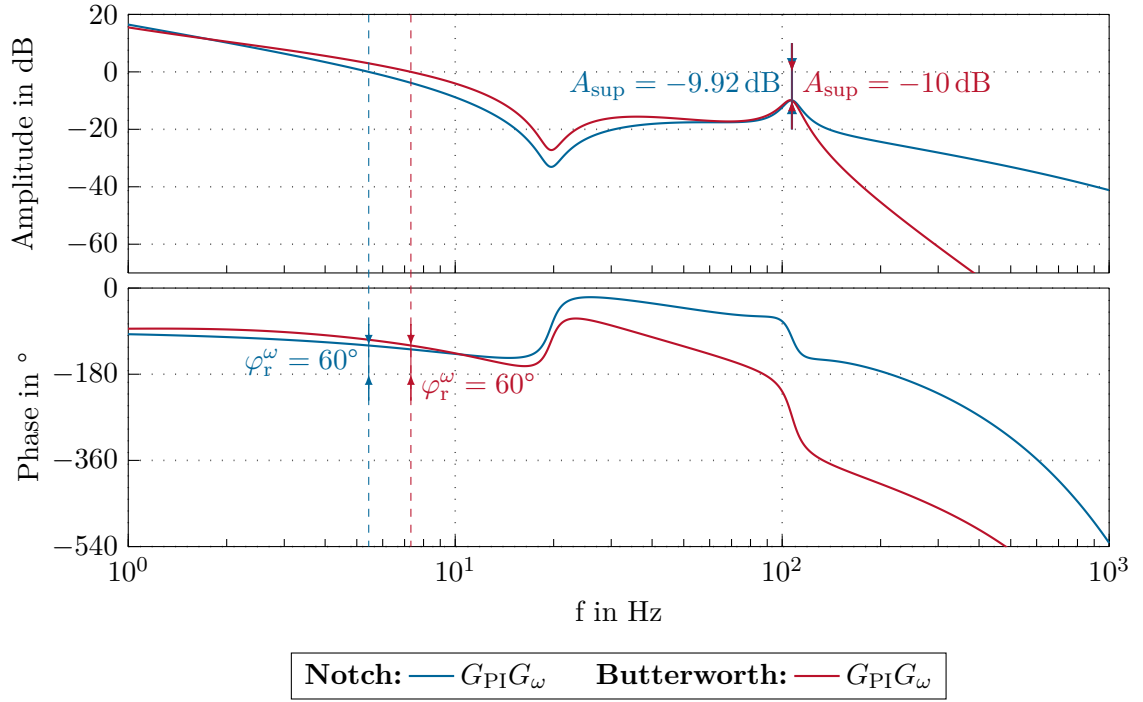


Figure 4.5: Open-loop transfer function of the velocity controlled plant, with plant and controller parameters according to Table A.4, Table A.6 and Table A.7 in Appendix A.

depicted in Figure 4.6. Although the control structure is cascaded, the velocity control

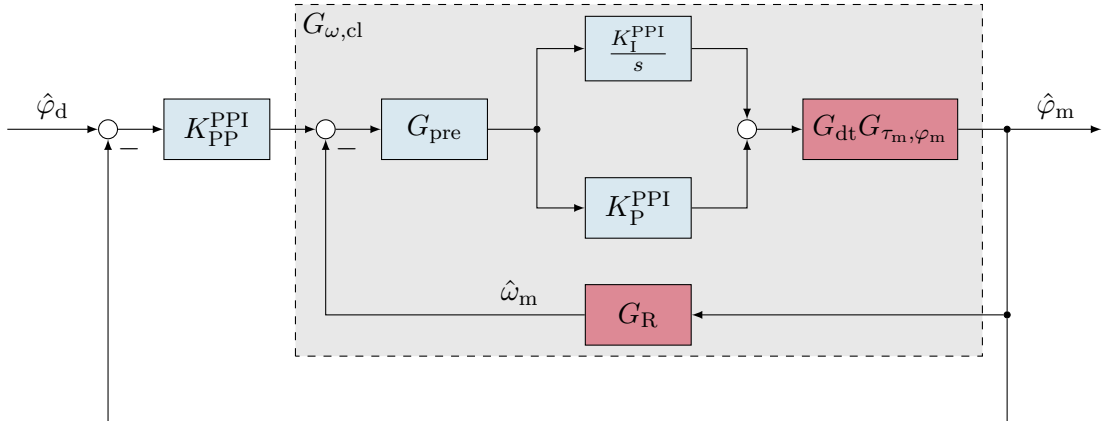


Figure 4.6: Block diagram of the position control loop.

loop has to be regarded in the design process, as its bandwidth is not large enough, compared to the position controller. Therefore, the closed-loop transfer function of the

velocity controlled loop, in the following denoted by

$$G_{\omega,cl} = \frac{G_{PI}G_{\tau_m, \varphi_m}G_{dt}}{1 + G_{PI}G_{\tau_m, \varphi_m}G_{dt}G_R}, \quad (4.10)$$

is used as starting point for the position controller design. The proposed proportional controller exhibits one degree of freedom, namely K_{PP}^{PPI} , and is given by the transfer function

$$C_\varphi = K_{PP}^{PPI}. \quad (4.11)$$

Therefore, only one design parameter of the open-loop transfer function can be chosen independently. Here, this parameter is the phase margin φ_r^φ of the open-loop transfer function. The phase margin is defined at the gain crossover frequency $\omega_{c,\varphi}$, which is given by

$$|G_{\omega,cl}(j\omega_{c,\varphi})C_\varphi| = 1. \quad (4.12)$$

Because the proportional controller can not change the phase of the open-loop transfer function, the frequency location of the gain crossover frequency has to be changed by the controller parameter K_{PP}^{PPI} . Therefore, in order to meet a desired phase margin φ_r^φ , the relation

$$\arg(G_{\omega,cl}(j\omega_{c,\varphi})) = -\pi + \varphi_r^\varphi \quad (4.13)$$

fixes the gain crossover frequency $\omega_{c,\varphi}$. Analogously to (4.9), this equation cannot be solved for $\omega_{c,\varphi}$ analytically, thus, a numerical solution approach is used to obtain the solution $\omega_{c,\varphi}^*$. Therefore, the controller gain is determined by

$$K_P^{PPI} = \frac{1}{|G_{\omega,cl}(j\omega_{c,\varphi}^*)|}. \quad (4.14)$$

In Figure 4.7, the open-loop transfer function of the position controlled plant for the different prefilter approaches of the previous section are depicted.

4.4 Feedforward controller design

Based on the identified model of Chapter 3, the model parameters can be used to design a feedforward control of the desired velocities and accelerations, as depicted in Figure 4.1. Because the cart position cannot be measured, we will assume a rigid coupling between the cart and the driving pulley, i.e., $c = 0$ and $d = 0$, see also Section 3.6. This yields, according to (2.25) for $f_g = 0$

$$\tau_m = \underbrace{(i_t^2 m_c + \Theta_e)}_{\tilde{m}_e} \dot{\omega}_m + \underbrace{(d_m + i_t^2 d_c)}_{\tilde{d}_v} \omega_m + \underbrace{(\tau_c + i_t f_c)}_{\tilde{\tau}_c} \text{sign}(\omega_m). \quad (4.15)$$

The parameters \tilde{d}_v for the viscous friction and $\tilde{\tau}_c$ for the Coulomb friction of the total mechanical system are used, as identified in Section 3.6. The sum of the motor mass

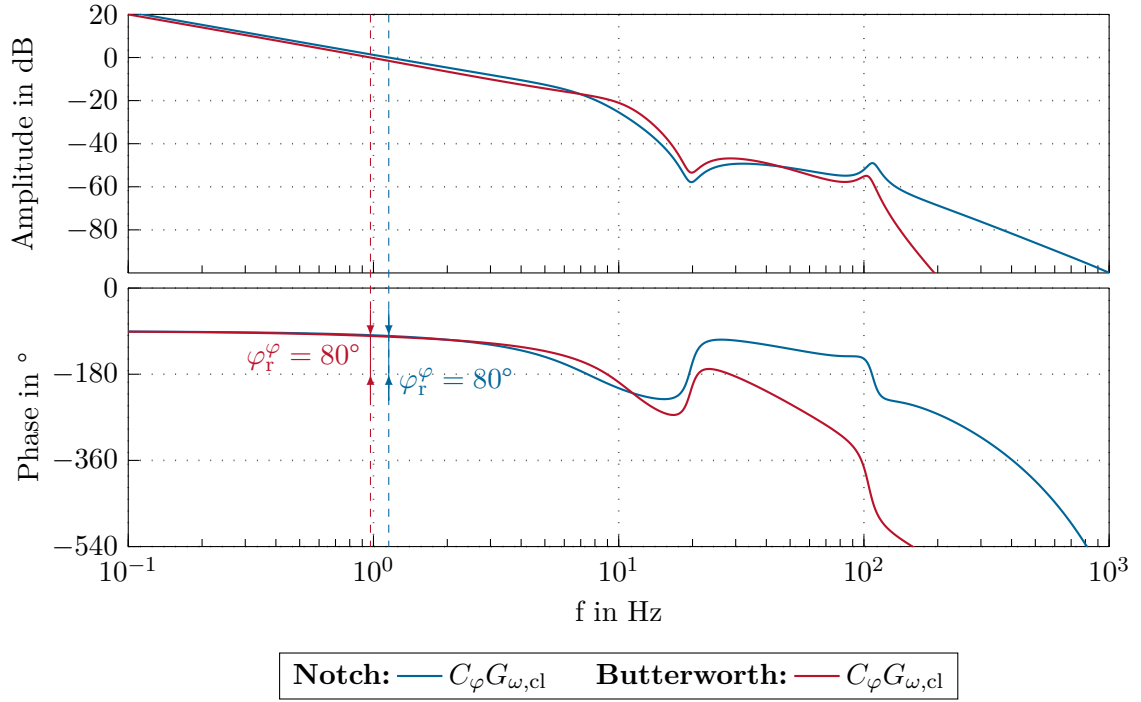


Figure 4.7: Open-loop transfer function of the position controlled plant, with plant and controller parameters according to Table A.4, Table A.6 and Table A.7 in Appendix A.

moment of inertia and the equivalent mass moment of inertia of the moving mass m_c is denoted by \tilde{m}_e . By replacing ω_m with the desired value ω_d , the feedforward torque

$$\tau^{\text{FF}} = \tilde{m}_e \dot{\omega}_d + \tilde{d}_v \omega_d + \tilde{\tau}_c \text{sign}(\omega_d) \quad (4.16)$$

and, hence, by a little abuse of the notation, the feedforward acceleration controller K_a^{PPI} shown in Figure 4.1 is determined. The velocity feedforward parameter K_v^{PPI} is simply given by

$$K_v^{\text{PPI}} = 1 \quad (4.17)$$

because $\hat{\omega}^{\text{FF}} = \hat{\omega}_d$ will impose the desired velocity ω_d . Obviously, the feedforward acceleration controller also accounts for the Coulomb friction. If the nonlinear friction identification shown in Section 3.6 is not desirable, the parameter $\tilde{\tau}_c$ can be set to zero.

To summarize this chapter on the automatic controller design process, the user has to choose the design parameters A_{sup} , φ_r^ω and φ_r^ϕ , as well as the filter parameters d_n or ω_{bw} , according to the application needs. This guarantees that the user has as much freedom as possible in adapting the controller, while the design process itself is automated and does not need any further intervention by the user. This allows to build up a graphical user interface with one or more sliders for the tuning parameters, which can then be used to manually tune the controllers for the application needs without any deeper knowledge in control theory.

5 Closed-loop measurement results

This chapter deals with measurement results in the closed-loop system. The controller is designed in Chapter 4. The first section shows measurements which put emphasis on the influence of the prefilter on the control results. The second section deals with different feedforward control strategies, namely the linear and nonlinear one, compared to an experiment without feedforward control. These results are presented with a small moving mass and a large moving mass. The last section of this chapter shows the influence of the moving mass on the measurement results. All measurements utilize a desired position change from $\xi_d = 0$ m to $\xi_d = 0.5$ m, while the desired trajectory is generated by the trajectory generator presented in Section 6.3 with the parameters listed in Table A.8 in Appendix A.

5.1 Influence of the prefilter

Figure 5.1 depicts the desired and actual cart position ξ_d and ξ , and, additionally, the control error for a position change of the cart with moving mass $m_c = 11.2$ kg. Moreover, the desired and the actual cart velocity, $\dot{\xi}_d$ and $\dot{\xi}$, are shown. As the controller utilizes the motor side measurements of the cart position and velocity, that is φ_m and ω_m , also the control errors of this signals with respect to ξ_d and $\dot{\xi}_d$ are depicted. The last diagram of the figure shows the actual value of the motor torque τ_m . It has to be noted that in the case of no prefilter, the control design procedure of Chapter 4 is applied with $G_{\text{pre}} = 1$. If the controller parameters of the controller design with prefilter are used and only $G_{\text{pre}} = 1$ is set for the implementation, the control loop is unstable due to the mechanical resonance of the plant. As mentioned in Section 4.2.1, both filter approaches show nearly the same response behavior. This is because the cascaded controllers were designed to fulfill the same conditions on the phase margins $(\varphi_r^\omega, \varphi_r^\varphi)$ and resonance suppression factor (A_{sup}) . However, the Butterworth filter approach is more robust to parameter variations compared to the Notch filter approach. This is because of the roll-off of the low-pass filter for higher frequencies. By comparing the control loops with prefilter and without prefilter, a significantly larger error in the position as well as in the velocity can be observed, thus, justifying the application of the prefilter in the controller design.

5.2 Influence of the feedforward control

The previous section outlined the influence of the prefilter on the control performance and the advantage of using a Butterworth prefilter. Because of this, in this section only the Butterworth prefilter is used in the controller design.

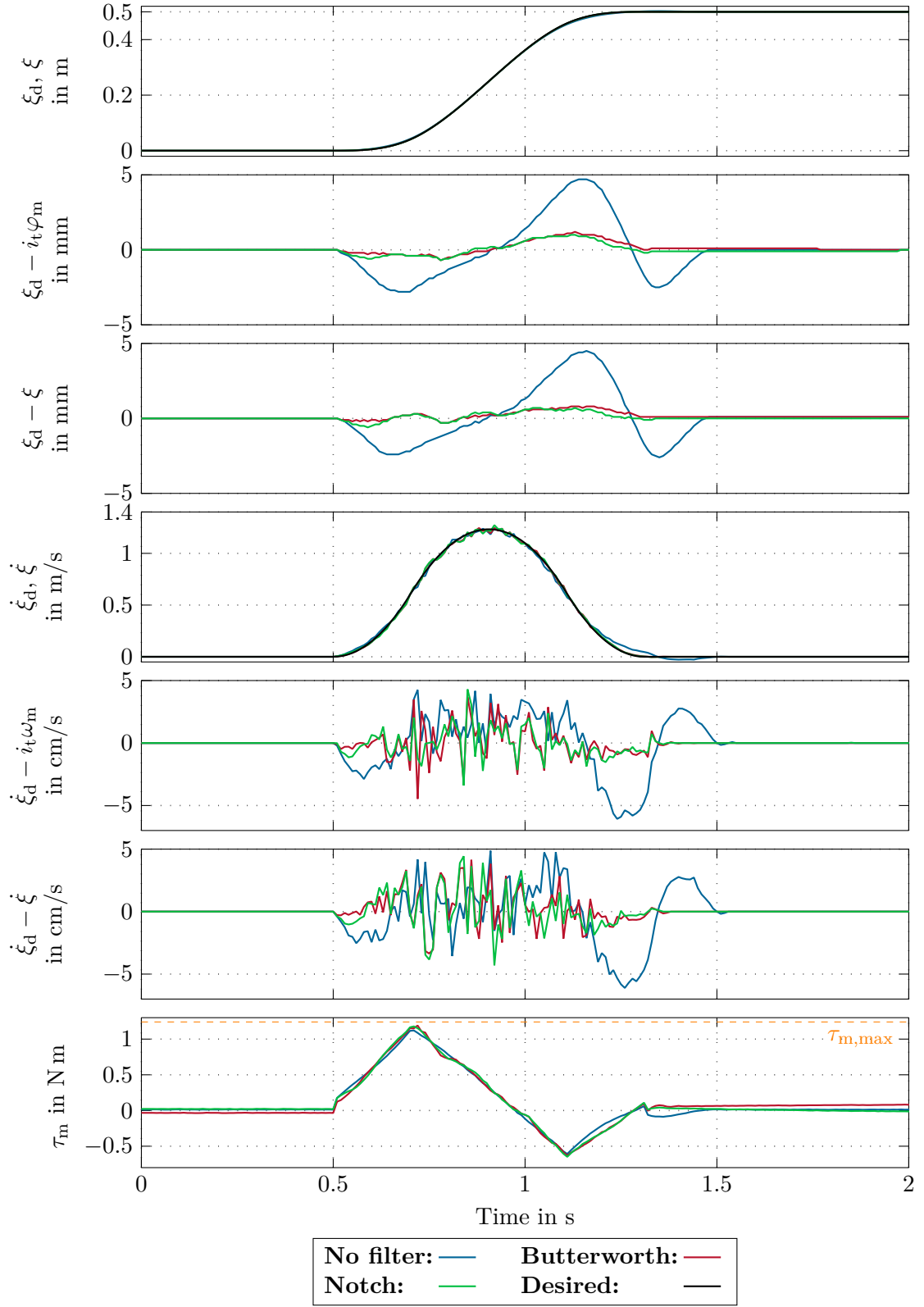


Figure 5.1: Position change from $\xi = 0$ mm to $\xi = 500$ mm using a Notch filter, a Butterworth filter and no prefilter and nonlinear feedforward control.

Analogously to Figure 5.1, Figure 5.2 and Figure 5.3 depict the response behavior of the closed-loop system. For the results depicted in Figure 5.2, a moving mass of $m_c = 11.2\text{ kg}$ is used and for the experiment depicted in Figure 5.3, a moving mass of $m_c = 0\text{ kg}$ is used. As expected, the controller without feedforward control shows the worst control performance. Including feedforward control is significantly more accurate, while the nonlinear feedforward controller shows the smallest positioning error with less than 1 mm, cf. Figure 5.4. Depending on the desired accuracy and implementation effort, the nonlinear feedforward control is preferable at the costs of the explicit friction identification, as outlined in Section 3.6. If the implementation effort should be as low as possible, the linear feedforward control is preferable. When comparing the measurement results of Figure 5.2 and Figure 5.3, it is obvious that for small moving masses the advantage of the feedforward control decreases. Moreover, it is worth mentioning that the linear feedforward control shows a sign reversal in the tracking error $\xi_d - \xi$ and the velocity error $\dot{\xi}_d - i_t \omega_m$, which can be explained by overcompensating the real friction for medium to high velocities, as the Coulomb friction is approximated by a viscous one.

5.3 Influence of the moving mass

In the measurement results depicted in Figure 5.4, a Butterworth prefilter is used for two different moving masses, i. e. $m_c = 11.2\text{ kg}$ and $m_c = 0\text{ kg}$, and nonlinear feedforward control. The dynamic error in both cases in the position is smaller than 1 mm, while the static positioning error is smaller than 100 μm . The static positioning error can be explained by the friction in the system. Especially for a small moving mass, the friction is the dominant effect, which explains the positioning error between $t = 1.3\text{ s}$ and $t = 1.8\text{ s}$. In the case of the small moving mass, the trajectory generator parameters can be further tuned as the motor torque limit $\tau_{m,\max}$ allows for a faster position change. However, in order to compare the results for both moving masses in this experiment, the trajectory generator parameters remain unchanged. In case of the larger moving mass, a larger positioning error $\xi_d - \xi$ compared to $\xi_d - i_t \varphi_m$ can be observed. This is due to the flexibility of the toothed belt.

To conclude, the measurement results in this chapter show that the usage of (nonlinear) feedforward control improves the overall control performance.

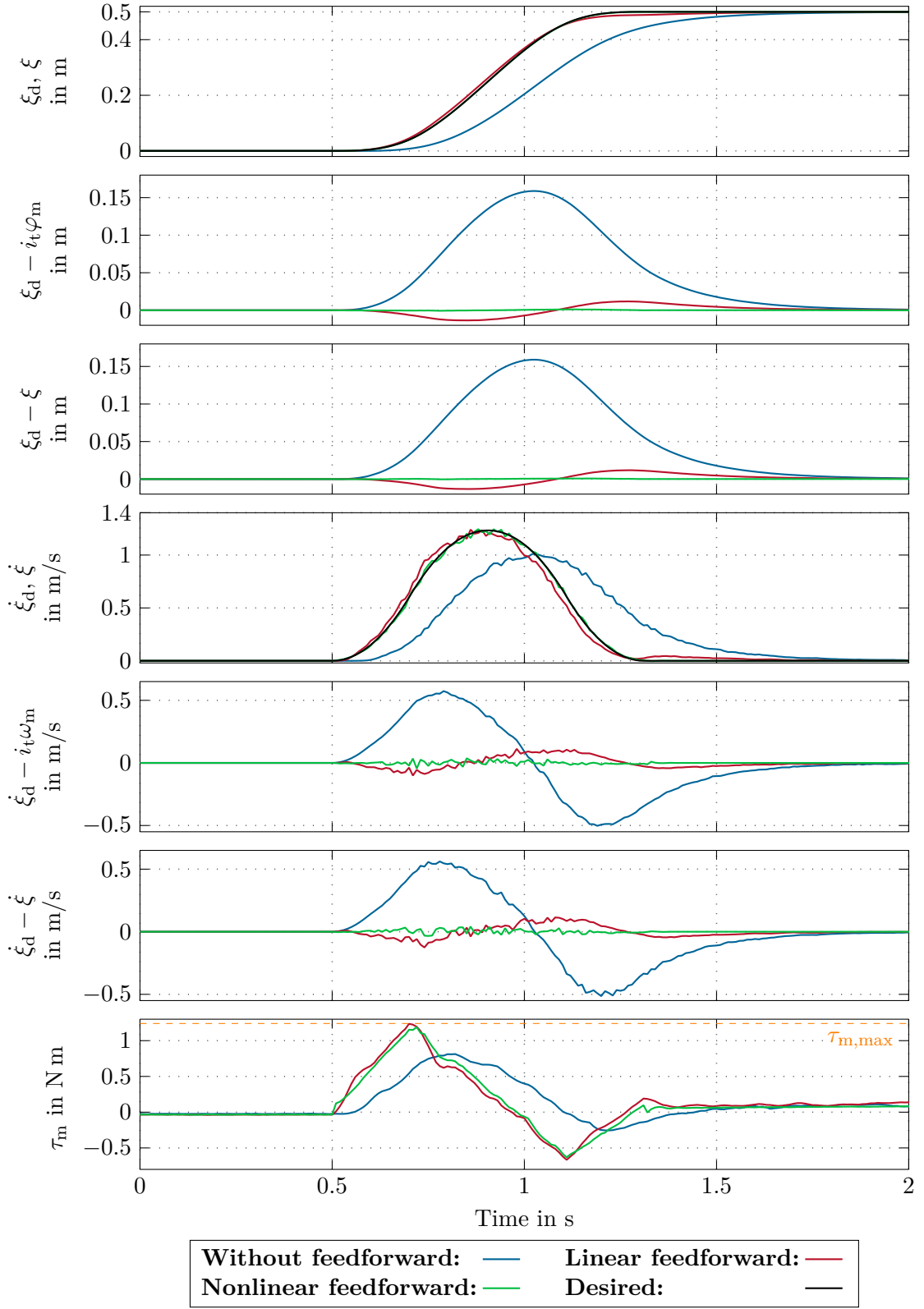


Figure 5.2: Position change from $\xi = 0$ mm to $\xi = 500$ mm using a Butterworth filter for filtering the mechanical resonance with linear, nonlinear and without feedforward control and moving mass $m_c = 11.2$ kg.

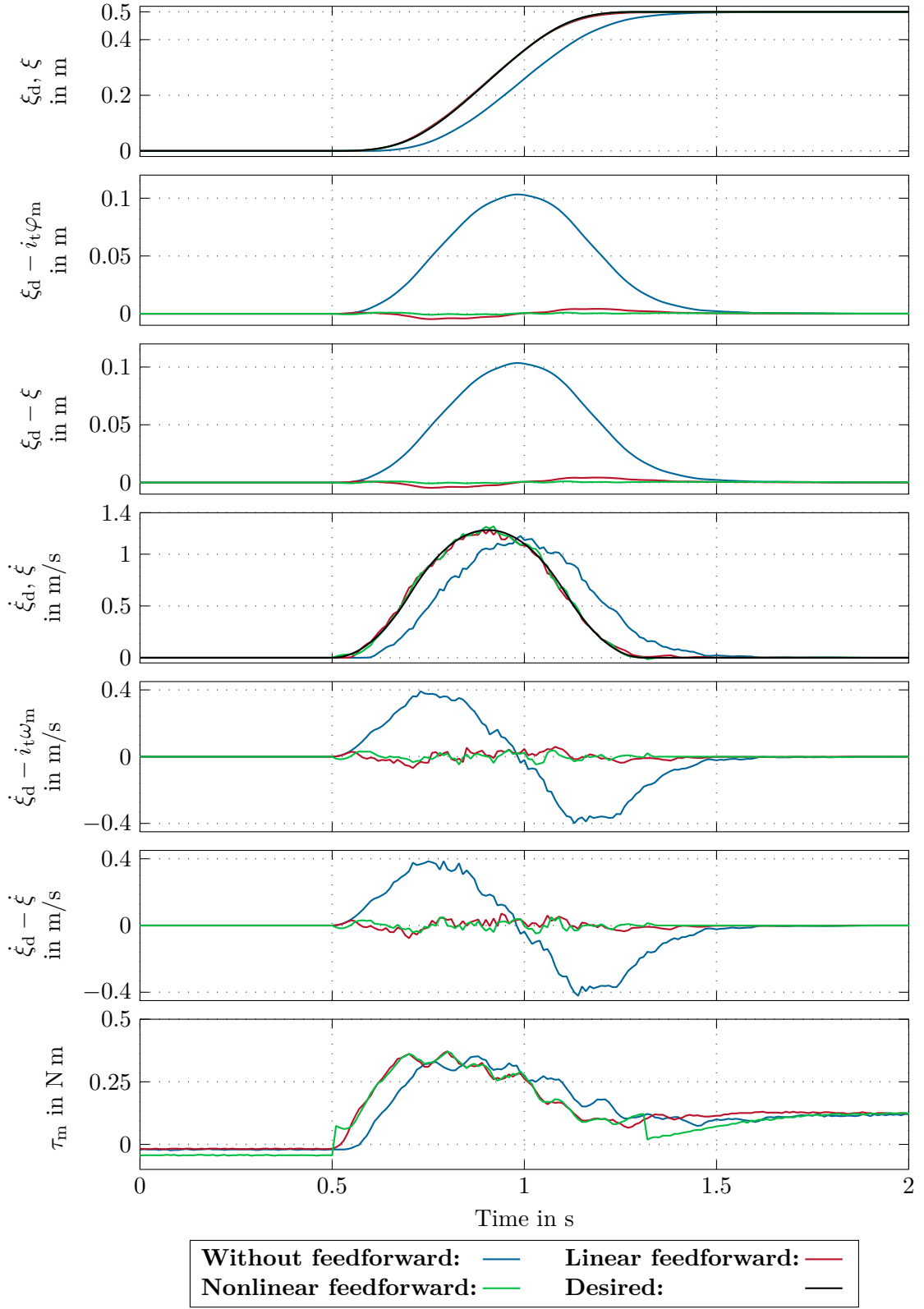


Figure 5.3: Position change from $\xi = 0$ mm to $\xi = 500$ mm using a Butterworth filter for filtering the mechanical resonance with linear, nonlinear and without feedforward control and moving mass $m_c = 0$ kg.

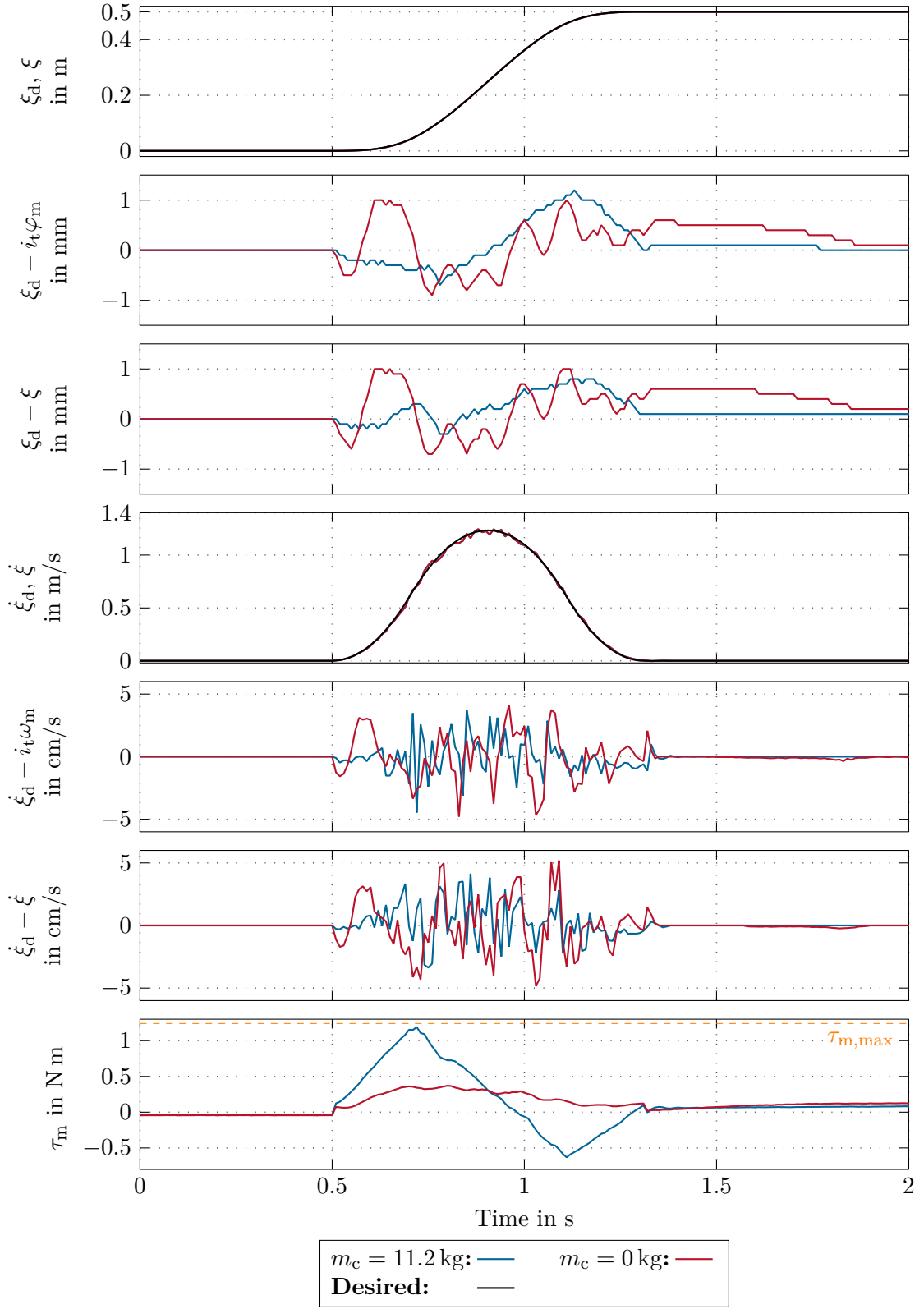


Figure 5.4: Position change from $\xi = 0$ mm to $\xi = 500$ mm using a Butterworth filter for filtering the mechanical resonance and nonlinear feedforward control with different moving masses.

6 Implementation

This chapter deals with some important notes regarding the implementation of the control strategies from the previous chapter on a real-time hardware (RTH) including the field programmable gate array (FPGA) assisted estimation of a velocity signal from the incremental encoder signals. Additionally, the considered integral controller includes a specific anti-windup procedure, which is discussed in the second section. The last section of this chapter presents a time-optimal trajectory generator for setpoint changes in the position.

6.1 Velocity signal calculation

In order to implement the cascaded velocity controller of Section 4.2, the velocity signal ω_m has to be estimated from the measured position signal φ_m .

Four approaches are outlined in the following:

- (i.) The first approach makes use of a classical first-order high-pass filter in the form

$$G_R = \frac{s}{sT_R + 1}, \quad (6.1)$$

with time constant $T_R > 0$.

- (ii.) The second approach, namely the event counter approach, counts the number of incremental encoder edges in one sampling period T_s and measures the time between the first and the last increment. This approach aims for a higher resolution of the velocity signal at high velocities. Details on this approach are presented in Section 6.1.1.
- (iii.) The third approach, in the following named gate measurement approach, measures the time between two consecutive incremental encoder edges and calculates the velocity based on that time. This method aims for a higher resolution of the velocity signal at low velocities. It is discussed in detail in Section 6.1.2.
- (iv.) The last approach combines the gate measurement approach and the event counter approach in order to take advantage of the benefits from both approaches. It is discussed in Section 6.1.3.

In Chapter 4, we introduced the transfer function

$$G_R = \frac{\hat{\omega}_m}{\hat{\varphi}_m}, \quad (6.2)$$

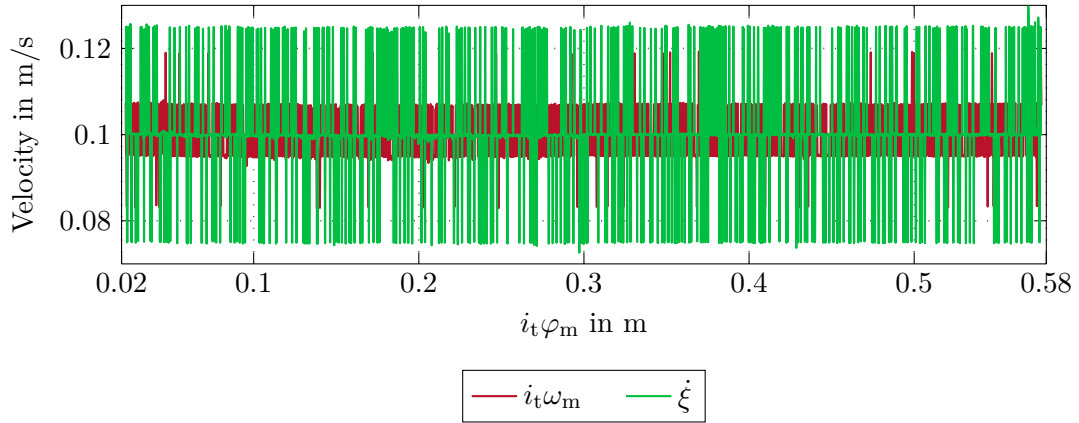


Figure 6.1: Velocity signal calculated by a first-order high-pass filter with desired velocity $i_t\varphi_m = 0.1$ m/s. Note the different heights of the spikes due to different encoder resolutions of the motor and cart incremental encoder.

cf. Figure 3.4(b) and Figure 3.4(c). The first approach, cf. (6.1), is simple to implement. Problematic, however, within this approach are the generated spikes as a consequence of the time-discrete implementation of (6.1), cf. Figure 6.1 and Figure 6.8. Especially for low velocities this can lead to a switching behavior between the minimal resolution and zero. This case is depicted in Figure 6.2, where the absolute value of the actual velocity drops below the minimal resolution $\dot{\xi}_{\min}$, which is given by the relation of the encoder resolution $\Delta\xi_{\min}$ and the sampling time T_s , i. e., by

$$\dot{\xi}_{\min} = \frac{\Delta\xi_{\min}}{T_s}. \quad (6.3)$$

Of course, by increasing the time constant T_R , this switching can be reduced at the costs of an additional phase lag in the closed-loop system. In order to reduce this necessary phase lag, that is to obtain a higher cutoff frequency of the filter, the gate measurement approach and the event counter approach are presented, both with different characteristics. The basic principles and characteristics are presented in [43] and [44]. These approaches will be combined in Section 6.1.3 to obtain a velocity signal with higher resolution, especially near the lower resolution bound of the high-pass filter approach.

The gate measurement and event counter approach as well as the combination of both are based on the incremental encoder signal channels A and B . Assuming a constant velocity, the encoder signals A and B are two differential rectangular signals, which are 90° out of phase to each other. For further explanation, the edges of the encoder signals need to be detected and are referred to as increments, see Figure 6.3. When transforming the encoder signals into the corresponding increments, the direction information of the quadrature signals A and B gets lost. However, it can be derived from the phase shift of the two signals to each other. If channel A leads in comparison to channel B , the velocity is positive and vice versa. Depending on this phase shift the increments count as positive for positive velocities and negative for negative velocities. Especially for low velocities it can occur that one of both channels jumps between high and low, whereas the other one

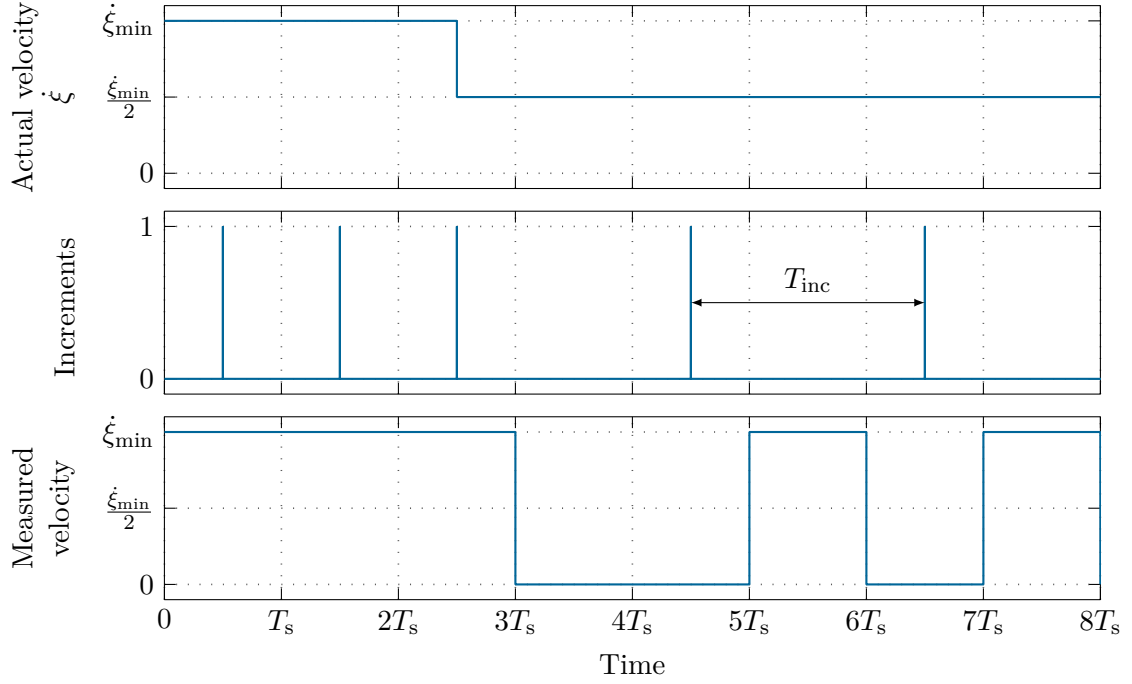


Figure 6.2: Showcase of the problem occurring when using a time-discrete high-pass filter to estimate the velocity from the incremental encoder position signals at the lower resolution bound $\dot{\xi}_{\min}$. Instantaneous change in the actual velocity is assumed for explaining reasons.

remains constant. Manufacturing imperfections or vibrations can lead to such a behavior. This is related to mechanical contact bouncing [45] and is here referred to as increment bouncing. To get rid of this behavior a state machine is used, which prevents repeated switching between two adjacent states.

A state S_i is referred to as a combination of the levels of both encoder channels, cf. Figure 6.3. Therefore, eight states exist, those are S_1 - S_4 for positive velocities and S_5 - S_8 for negative velocities. These states are transited cyclically when moving with constant velocity. The state sequence is only disturbed by the bouncing phenomena or when a sign reversal of the velocity occurs. The increment debouncing now prevents a switching from, for example, S_3 to S_7 , if the previous state has been S_2 . However, the previous state is then set to be S_7 and if the next state is S_8 , a sign reversal of the velocity occurred. On the other hand, if the next state is S_3 , the previous state is again set to be S_2 . An increment is then only generated, if a proper state transition occurred, that is, for positive velocities $S_i \rightarrow S_{\text{mod}(i+1,4)}$ with $i \in \{1, 2, 3, 4\}$. The downside of this increment debouncing approach is that a sign reversal in the velocity is delayed by one increment, or equivalently by one state transition. In the following, the increment signal is used to calculate an estimate for the actual velocity.

Independent of a rotary or translational encoder the following schemes can be applied to both. Henceforth, the distinction between ω and $\dot{\xi}$ is dropped in this section.

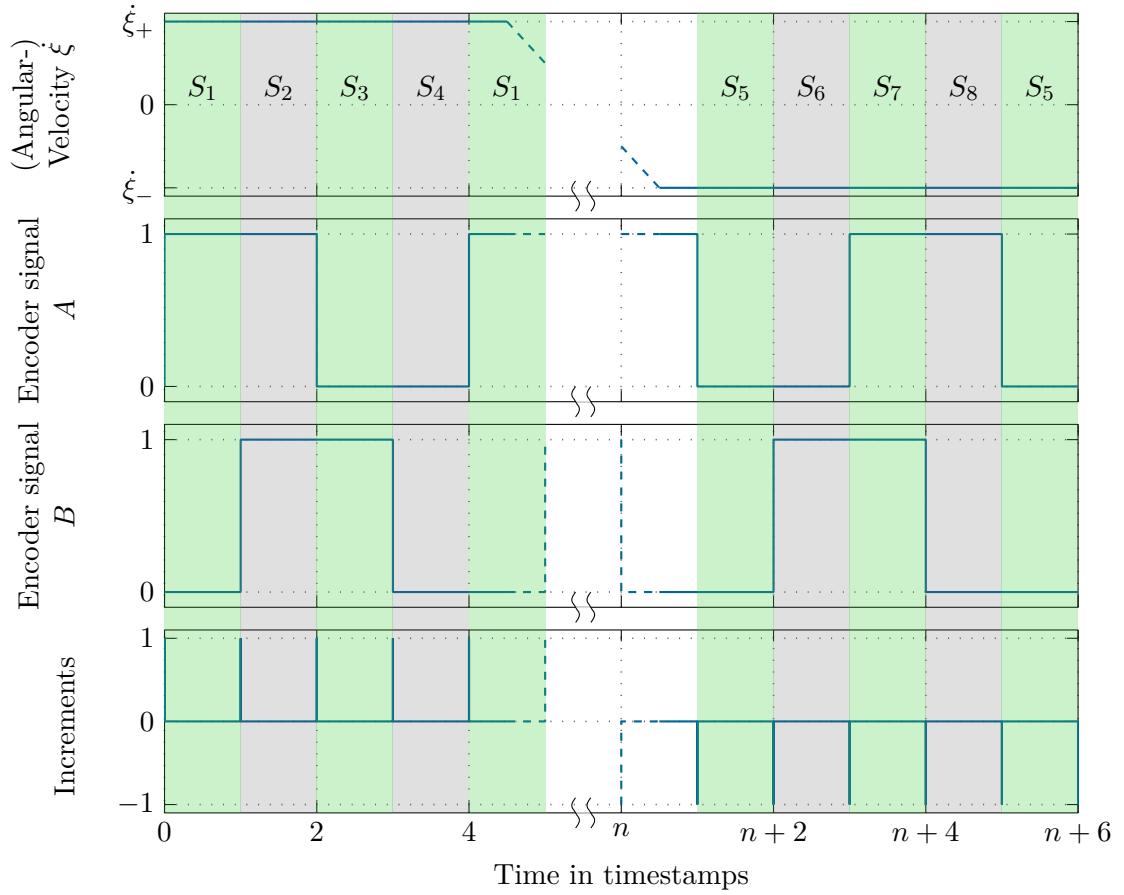


Figure 6.3: Showcase of the state machine and of the calculation of the increment signal from the quadrature incremental encoder signals for constant negative and positive velocities $\dot{\xi}_-$ and $\dot{\xi}_+$, where $|\dot{\xi}_-| = |\dot{\xi}_+|$.

6.1.1 Event counter approach

Within the event counter approach, the time between the first increment in the fundamental sampling period T_s and the last increment is measured, and additionally, the numbers of increments n_{inc} is counted. Figure 6.4 illustrates the principle of this approach. The velocity estimation is then given by

$$\dot{\xi}_h = \frac{(n_{\text{inc}} - 1)\Delta\xi_{\min}}{T_{n,\text{inc}}}, \quad (6.4)$$

where $T_{n,\text{inc}} \leq T_s$ denotes the measurement time, as depicted in Figure 6.4, and $n_{\text{inc}} \geq 2$. Because of the condition $n_{\text{inc}} \geq 2$, the minimal measurable velocity is given by

$$\dot{\xi}_{h,\min} = \frac{\Delta\xi_{\min}}{T_s}, \quad (6.5)$$

which occurs if $n_{\text{inc}} = 2$, that is, exactly two increments are detected in the sampling period T_s . On the other hand, the maximal velocity $\dot{\xi}_{h,\max}$ is theoretically only limited by

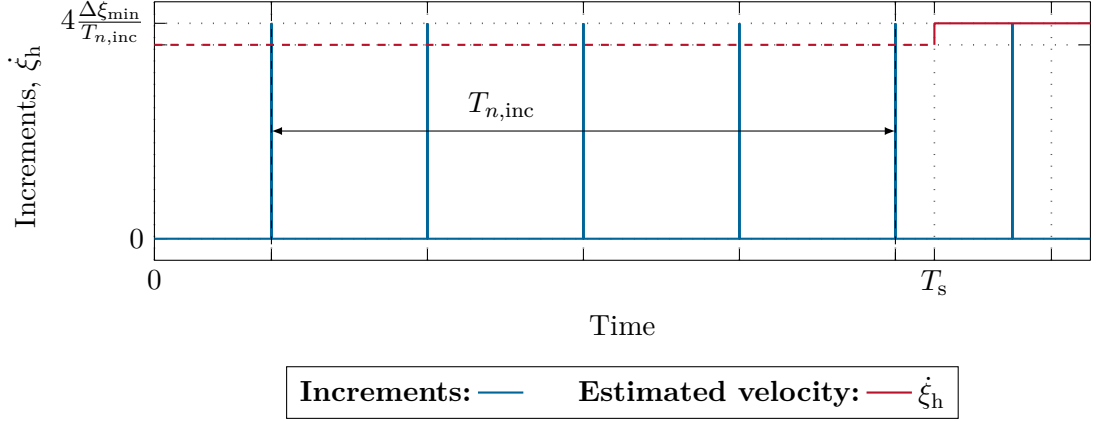


Figure 6.4: Graphical visualization of the event counter approach for estimating the actual velocity with $n_{\text{inc}} = 5$.

the processing speed of the used hardware. That is, if more than one increment is received from the incremental encoders during the timespan Δt_{min} , the maximum velocity reads as

$$\dot{\xi}_{h,\text{max}} = \frac{\Delta \xi_{\text{min}}}{\Delta t_{\text{min}}}. \quad (6.6)$$

The relationship between the actual velocity $\dot{\xi}$, the measurement time $T_{n,\text{inc}}$, as well as the measured position difference $\Delta \xi$ are given by

$$T_{n,\text{inc}} = \frac{\Delta \xi}{\dot{\xi}} \quad (6.7)$$

with

$$\Delta \xi = (n_{\text{inc}} - 1) \Delta \xi_{\text{min}}. \quad (6.8)$$

The difference of the event counter approach compared to the time-discrete differentiator with velocity estimation

$$\dot{\xi}_{\text{R}} = \frac{\Delta \xi}{T_s} \quad (6.9)$$

and constant sampling time T_s goes to zero for higher velocities, as

$$T_{n,\text{inc}} \rightarrow T_s \quad \text{if} \quad \dot{\xi} \rightarrow \infty. \quad (6.10)$$

In this case, the event counter approach is equivalent to the time-discrete high-pass filter, except for the additional filtering with the time constant T_{R} .

Under the assumption that $T_{n,\text{inc}}$ can be measured with an accuracy of $\pm \Delta t_{\text{min}}$ and the position measurement of $\Delta \xi_{\text{min}}$ is error free, cf. [43], the relative velocity error can be expressed as

$$\Delta \dot{\xi}_{h,\text{err}}(\dot{\xi}) = 100 \frac{\dot{\xi}_{\text{h}} - \dot{\xi}}{\dot{\xi}} \approx \mp 100 \frac{\dot{\xi}}{\left\lfloor \frac{\dot{\xi} T_s}{\Delta \xi_{\text{min}}} \right\rfloor \dot{\xi}_{h,\text{max}}} \quad (6.11)$$

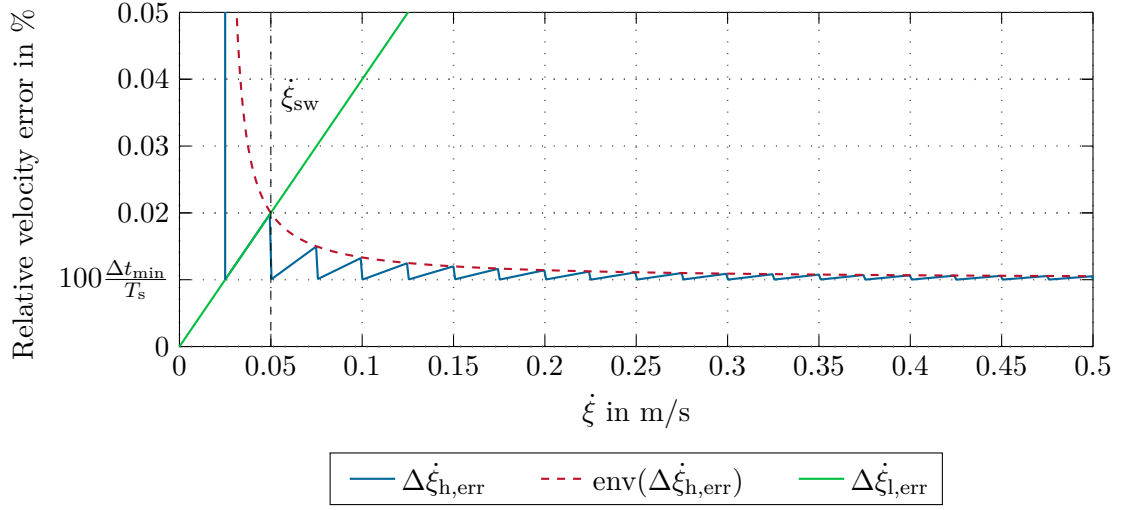


Figure 6.5: Comparison of the relative velocity errors of the gate measurement approach error $\Delta\dot{\xi}_{l,err}$ and the event counter approach $\Delta\dot{\xi}_{h,err}$. Here, $\text{env}(\cdot)$ denotes the envelope function of the argument. The minimal time resolution is supposed to be $\Delta t_{\min} = 10 \text{ ns}$ and the incremental encoder resolution is given by $\Delta\xi_{\min} = 2.5 \mu\text{m}$.

in percent, see Section C.1 in Appendix C. The visualization of the error in Figure 6.5 shows the envelope of the relative error

$$\text{env}\left(\Delta\dot{\xi}_{h,err}(\dot{\xi})\right) = 100 \frac{\dot{\xi}}{\left(\frac{\dot{\xi} T_s}{\Delta\xi_{\min}} - 1\right) \dot{\xi}_{h,\max}} \quad (6.12)$$

decreasing with increasing velocity, whereas the real error switches between its minimal value and the envelope function depending on the number of increments n_{inc} that fit into one sampling period T_s . Obviously, the error shows a reversed dependency on the actual velocity in comparison to the gate measurement approach, cf. Figure 6.5, hence, providing the justification for the usage in the higher velocity range, that is $\dot{\xi} > \dot{\xi}_{h,\min}$. However, this approach has its limitation as the relative velocity error $\Delta\dot{\xi}_{h,err}$ tends towards

$$\arg \min_{\dot{\xi}} \left(\Delta\dot{\xi}_{h,err}(\dot{\xi}) \right) = 100 \frac{\Delta t_{\min}}{T_s} \quad (6.13)$$

for $\dot{\xi} \rightarrow \dot{\xi}_{h,\max}$.

6.1.2 Gate measurement approach

Note that the condition $n_{\text{inc}} \geq 2$ of the event counter approach limits the minimal measurable velocity. Hence, we introduce a new approach, namely the gate measurement approach, for $n_{\text{inc}} \leq 2$. Compared to the event counter approach, the gate measurement approach does not average the number of increments over one period of the sampling

time T_s . Rather than that, only the last two increments are utilized, regardless of the number of increments n_{inc} that are detected in the time span T_s , cf. [44]. That is, this method only provides the latest available velocity estimation, which is based on the time difference between the last two increments, see Figure 6.6. Hence, the method provides a more accurate velocity estimation, that is, an estimate with a smaller phase shift at the costs of being more prone to noise, manufacturing imperfections, especially regarding the position resolution $\Delta\xi_{\text{min}}$, and other distortions.

The estimated velocity of the gate measurement approach is then given by

$$\dot{\xi}_l = \frac{\Delta\xi_{\text{min}}}{T_{\text{inc}}} . \quad (6.14)$$

Here, T_{inc} denotes the measured time between the last two increments, see Figure 6.2. Crucial for achieving a high resolution is an accurate time-measurement of the time T_{inc} . This accuracy can only be achieved by an **FPGA** implementation of the time-measurement. The test hardware has a time resolution of $\Delta t_{\text{min}} = 10 \text{ ns}$, with a position resolution of $\Delta\xi_{\text{min}} = 2.5 \text{ }\mu\text{m}$, leading to an approximate maximal measurable velocity of

$$\dot{\xi}_{l,\text{max}} = \frac{\Delta\xi_{\text{min}}}{\Delta t_{\text{min}}} = 250 \text{ m/s} , \quad (6.15)$$

where the resolution bound of the time-measurement is reached. For velocities larger than $\dot{\xi}_{l,\text{max}}$, the time-measurement is not feasible anymore.

The relative velocity error $\Delta\dot{\xi}_{l,\text{err}}$ of the gate measurement approach in percent is given by

$$\Delta\dot{\xi}_{l,\text{err}}(\dot{\xi}) = 100 \frac{\dot{\xi}_l - \dot{\xi}}{\dot{\xi}} = \mp 100 \left(\frac{\dot{\xi}}{\dot{\xi}_{l,\text{max}} \pm \dot{\xi}} \right) , \quad (6.16)$$

see Section C.2 in Appendix C. Note that the relative velocity error $\dot{\xi}_{l,\text{err}}$ depends on the actual velocity $\dot{\xi}$. The graphical representation of this equation is depicted in Figure 6.5, where the relative error in the depicted velocity range is nearly linearly decreasing with the velocity. Obviously, for the intended speed range, i.e., small velocities, this method shows a sufficiently small error, which is, however, increasing with increasing velocity. If, only a low time-measurement resolution Δt_{min} is available, the advantage of this method over the event counter approach decreases even faster with increasing velocity $\dot{\xi}$ and encoder resolution $\Delta\xi_{\text{min}}$, as indicated by (6.16).

The relative velocity error $\Delta\dot{\xi}_{l,\text{err}}$ does reach zero for zero velocity $\dot{\xi} = 0$, however, a new velocity value is only available when a new increment from the incremental encoder is detected. The estimated velocity never reaches zero, when the actual velocity is zero, i.e., $n_{\text{inc}} = 0$, but freezes at the last velocity estimate. For this reason, a timeout time T_{out} is introduced after which the velocity estimate is set to zero, when no further increment is detected, that is $T_{\text{inc}} \geq T_{\text{out}} > T_s$. In order to provide more accurate velocity estimates cyclic with the controller sampling time T_s , the velocity within the time span T_{out} is approximated by

$$\dot{\xi}_l = \frac{\Delta\xi_{\text{min}}}{\tau} , \quad \text{with } T_s < \tau < T_{\text{out}} , \quad (6.17)$$

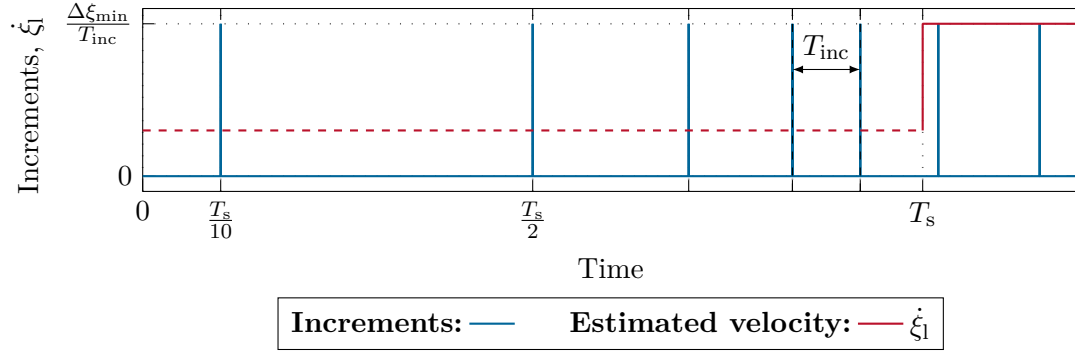


Figure 6.6: Schematic picture of the gate measurement approach for velocities above the intended measurement range.

where τ denotes the time since the last increment was detected, see Figure 6.7. This value remains as an estimate for the velocity, as long as no further increment is detected within $\tau \leq T_{\text{out}}$.

By adapting the gate measurement approach with the timeout time, the lower bound of the measurable velocity decreases to

$$\dot{\xi}_{l,\min} = \frac{\Delta \xi_{\min}}{T_{\text{out}}} . \quad (6.18)$$

Together with the condition $n_{\text{inc}} \leq 2$, this defines the reasonable velocity range for this method.

Because of the problems in the higher velocity range, the event counter approach, as explained in the previous section, is preferred for velocities where $n_{\text{inc}} > 2$.

6.1.3 Combined gate measurement and event counter approach

In Section 6.1.1 and Section 6.1.2 two approaches for estimating the velocity were introduced. The gate measurement approach is more accurate for small velocities, see (6.16), and the event counter approach is more accurate at high velocities, cf. (6.11). In the worst case, the relative error functions (6.12) and (6.16) intersect at

$$\dot{\xi}_{\text{sw}} = \frac{2\Delta \xi_{\min}}{T_s - \Delta t_{\min}} . \quad (6.19)$$

The switching function

$$\delta_{\text{sw}}(\dot{\xi}_l) = \begin{cases} 0 & \text{if } \dot{\xi}_l \leq \frac{\dot{\xi}_{\text{sw}}}{2} \\ \frac{1}{2} \left(1 - \sin \left(\pi \frac{\dot{\xi}_l}{\dot{\xi}_{\text{sw}}} \right) \right) & \text{if } \frac{\dot{\xi}_{\text{sw}}}{2} < \dot{\xi}_l < \frac{3\dot{\xi}_{\text{sw}}}{2} \\ 1 & \text{if } \dot{\xi}_l \geq \frac{3\dot{\xi}_{\text{sw}}}{2} \end{cases} \quad (6.20)$$

is introduced in order to combine the advantages of both approaches. The combined velocity signal is then expressed as

$$\dot{\xi}_m = (1 - \delta_{\text{sw}}) \dot{\xi}_l + \delta_{\text{sw}} \dot{\xi}_h \approx \dot{\xi} . \quad (6.21)$$

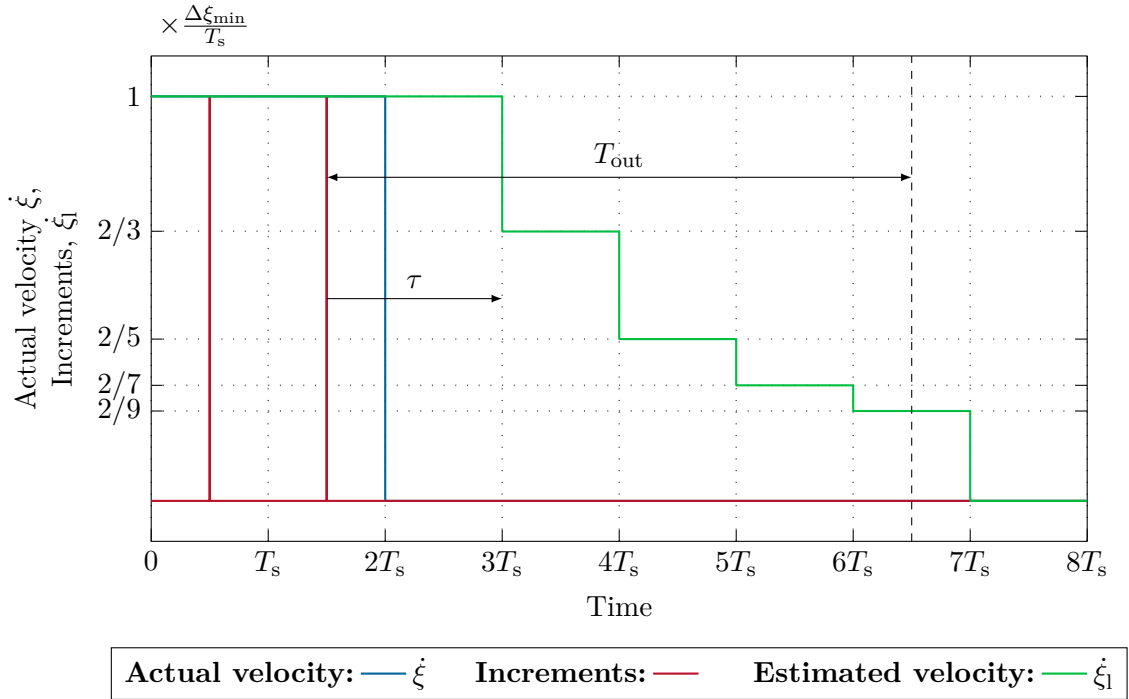


Figure 6.7: Schematic picture of the timeout extension of the gate measurement approach.

For the showcase $T_{out} = 5T_s$ has been chosen, and the actual velocity is supposed to jump from its initial value $\frac{\Delta \xi_{min}}{T_s}$ to zero at $t = 2T_s$.

Even though this allows for a better velocity signal compared to the pure differentiator approach, the signal $\dot{\xi}_m$ needs to be filtered by means of a low-pass filter. In order to do so, the signals $\dot{\xi}_l$ and $\dot{\xi}_h$ are filtered with the same filter and afterwards they are combined, as denoted in (6.21). Figure 6.8 depicts the unfiltered signals $\dot{\xi}_l$ and $\dot{\xi}_h$, as well as the velocity $\dot{\xi}_R$ calculated using a time-discrete high-pass filter, see (6.2). It can be noted that for low velocities the gate measurement approach provides a higher accuracy and for higher velocities the event counter approach is preferable. Moreover, the difference between a time-discrete differentiator and the event counter approach diminishes for velocities above approximately $\dot{\xi} = 0.1$ m/s. This is in accordance to the explanations in the previous sections. However, the gate measurement approach shows a high jitter in the upper velocity range due to the fact that more than two increments are detected within the time T_s .

To conclude this section, the presented velocity signal estimation approach allows for a high measurement accuracy, especially for low velocities. Clearly, by means of the improved velocity measurement it is possible to increase the bandwidth of the velocity controller. However, different tests have shown that the possible improvement in control performance when using the more sophisticated combined gate measurement and event counter approach is limited. Summarizing, the first-order high-pass filter approach is simple to implement and provides nearly an equivalent control performance.

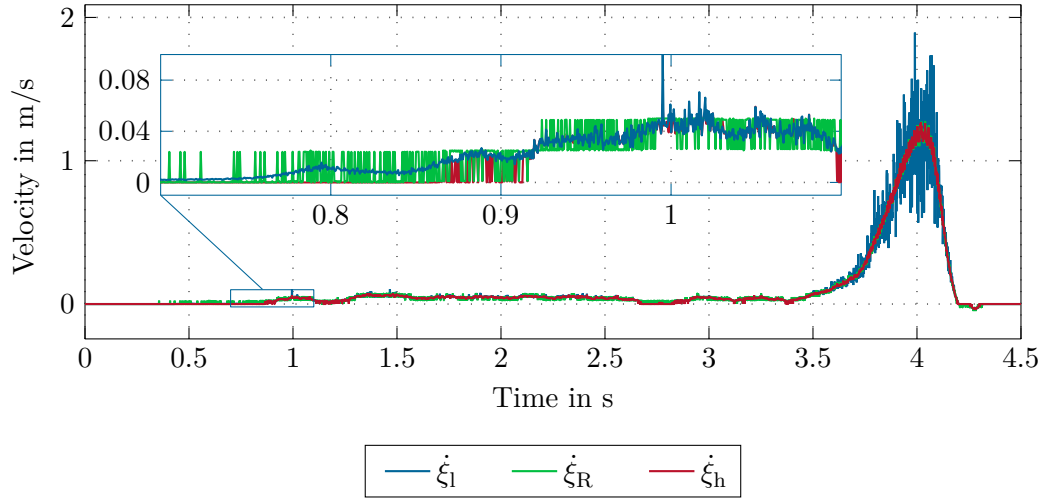


Figure 6.8: Comparison of the time-dependency of the gate measurement approach $\dot{\xi}_l$ and the event counter approach $\dot{\xi}_h$ for generating the velocity signals based on the incremental encoder output signals. For comparison reasons, the velocity signal $\dot{\xi}_R$, generated by a time-discrete high-pass filter, is also shown.

6.2 Integrator anti-windup

In Section 4.2, a controller with integral action for the velocity is presented. In combination with a limited control action $\tau_{m,\max}$ of the motor, integrator windup can occur, see [46]. Especially in positioning systems this behavior leads to an overshoot in the actual position compared to the desired one. An anti-windup measure aims at reducing the resulting overshoot. Different approaches are proposed in literature, see [41, p. 76ff], [46] and [47]. A straightforward approach to prevent integrator windup is presented here.

During normal operating conditions, that is, if the desired torque τ_d of the velocity controller fulfills $-\tau_{m,\max} \leq \tau_d \leq \tau_{m,\max}$, the state of the time-continuous integrator of the velocity controller is given by

$$x_I(t) = \int_0^t e_\omega(\tau) d\tau, \quad (6.22)$$

where x_I denotes the integrator state and e_ω the control error of the velocity control loop, see Figure 6.9. Using a sampling time T_s , so that $t = kT_s$ is valid, the notation

$$x_I[k] = x_I(kT_s) \quad (6.23)$$

and

$$e_\omega[k] = e_\omega(kT_s) \quad (6.24)$$

is introduced. The respective discrete-time integrator is then implemented in the form

$$x_I[k+1] = x_I[k] + T_s e_\omega[k]. \quad (6.25)$$

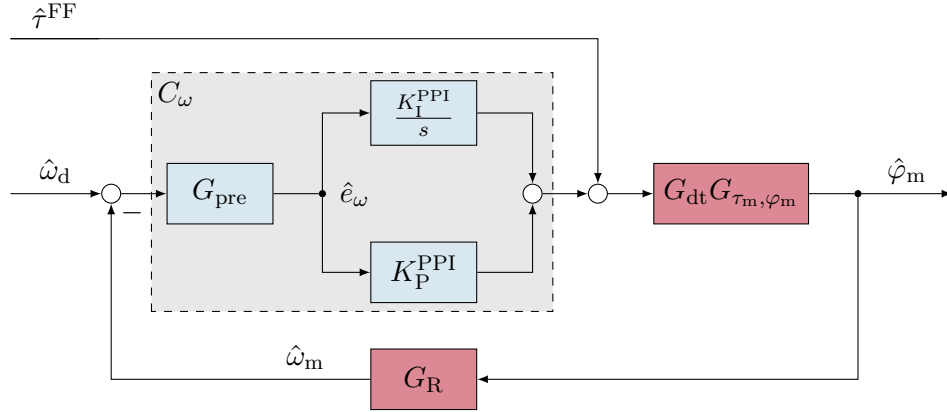


Figure 6.9: Block diagram of the velocity control loop with filtered velocity control error \hat{e}_ω .

If the control limits are violated, the conditional integration

$$x_I[k+1] = \begin{cases} \frac{\tau_{m,\max} - K_P^{PPI} e_\omega[k] - \tau^{FF}[k]}{K_I^{PPI}} & \text{if } (\tau_d[k+1] \geq \tau_{m,\max}) \wedge (e_\omega[k] > 0) \\ \frac{-\tau_{m,\max} - K_P^{PPI} e_\omega[k] - \tau^{FF}[k]}{K_I^{PPI}} & \text{if } (\tau_d[k+1] \leq -\tau_{m,\max}) \wedge (e_\omega[k] < 0) \\ x_I[k] + T_s e_\omega[k] & \text{otherwise} \end{cases} \quad (6.26)$$

is executed. The integrator state is set to meet the control limits exactly, if they would be exceeded. This conditional integration is used as anti-windup action and is compared to an experiment with an integrator according to (6.25). The measurement results are depicted in Figure 6.10. Even though the output of the controller reaches the actuation limit only for a short time, the anti-windup action shows a faster return to the actuation area after leaving the limit $\tau_{m,\max}$. Consequently, this leads to a smaller error in the position and velocity as can be seen in the highlighted area.

6.3 Trajectory generator

In trajectory following control, we would like to move from a starting position

$$\xi(0) = \xi_{\text{start}} \quad (6.27)$$

with initial velocity

$$\dot{\xi}(0) = \dot{\xi}_{\text{start}} \quad (6.28)$$

and acceleration

$$\ddot{\xi}(0) = \ddot{\xi}_{\text{start}} \quad (6.29)$$

at time $t = 0$ to an end position

$$\xi(T_{\text{trj}}) = \xi_{\text{end}} \quad (6.30)$$

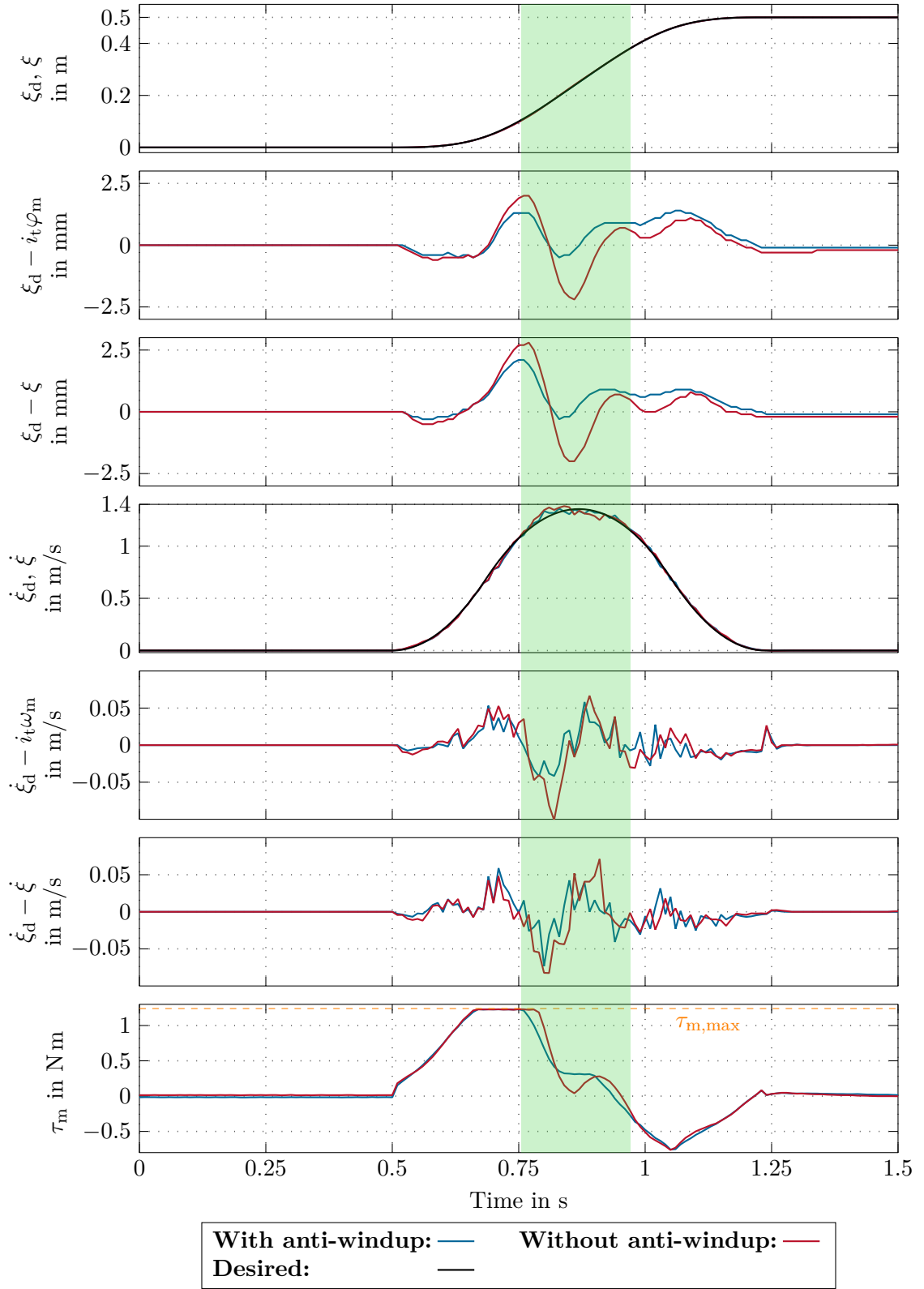


Figure 6.10: Influence of the integrator anti-windup on the control results for a position change of 500 mm. Controller parameters are given by $C_{\mathcal{B}}$, plant parameters by $G_{\mathcal{A}}$ and trajectory generator parameters by $T_{\mathcal{A}}$ and $T_{\mathcal{B}}$, see Table A.4, Table A.7, Table A.8 and Table A.9 in Appendix A.

with end velocity

$$\dot{\xi}(T_{\text{trj}}) = \dot{\xi}_{\text{end}} \quad (6.31)$$

and acceleration

$$\ddot{\xi}(T_{\text{trj}}) = \ddot{\xi}_{\text{end}} \quad (6.32)$$

within a transition time T_{trj} . In Chapter 5, especially in Section 5.2, the benefit of feedforward control is shown. In order to utilize this benefit, a trajectory generator has to provide a twice-continuously differentiable trajectory $\xi_d(t)$. The target of the presented trajectory generator is now to provide a time-optimal trajectory $\xi_d(t)$ and to meet the constraints in the velocity $\dot{\xi}_{\min} \leq \dot{\xi}_d \leq \dot{\xi}_{\max}$, the acceleration $\ddot{\xi}_{\min} \leq \ddot{\xi}_d \leq \ddot{\xi}_{\max}$ and the jerk $j_{\min} \leq j_d \leq j_{\max}$. Hereby, the jerk j is defined as

$$j := \ddot{\xi}. \quad (6.33)$$

The 7-step trajectory generator introduced in [48] allows to handle these constraints. The basic idea is to utilize the bang-bang behavior in the jerk j as a result of a time-optimal optimization problem subject to input and output constraints, see [49]. The so generated jerk signal is then integrated and used to obtain the desired trajectory $\xi_d(t)$. There are three main phases, an acceleration phase $P1 - P3$, a phase with maximum velocity $P4$ and a deceleration phase $P5 - P7$ as shown in Figure 6.11. The acceleration and deceleration phase are subdivided into phases with maximum jerk j_{\max} , $P1$ and $P7$, phases with maximum acceleration $\ddot{\xi}_{\max}$, $P2$ and $P6$ as well as phases with minimum jerk j_{\min} , $P3$ and $P5$. In [48], the underlying optimization problems are formulated and solved. The reader is kindly referred to [48] for more details on the 7-step trajectory generator.

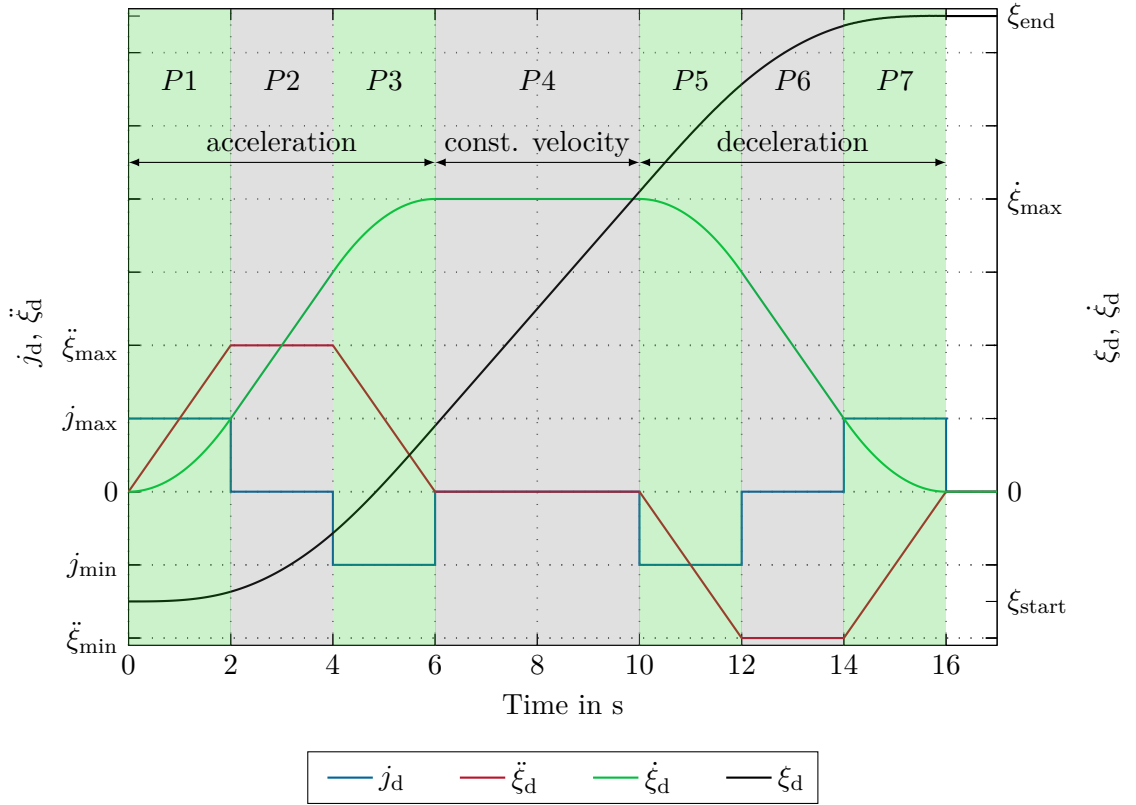


Figure 6.11: Trajectory $\xi_d(t)$ of the 7-step trajectory generator for $\ddot{\xi}(0) = 0 \text{ m/s}^2$, $\dot{\xi}(0) = 0 \text{ m/s}$, $\xi(0) = \xi_{\text{start}}$ and $\xi(T_{\text{trj}}) = \xi_{\text{end}}$ and the constraints $j_{\min} \leq j_d \leq j_{\max}$, $\ddot{\xi}_{\min} \leq \ddot{\xi}_d \leq \ddot{\xi}_{\max}$ and $\dot{\xi}_{\min} \leq \dot{\xi}_d \leq \dot{\xi}_{\max}$.

7 Conclusions and outlook

This chapter gives an overview and conclusions of the previous chapters and puts emphasis on the results and gained knowledge throughout this work. Additionally to this, an outlook is given on further research opportunities and possible improvements to the approaches presented in this work.

In Chapter 2, a mathematical model based on the mechanical structure of the linear belt driven servo mechanism was presented. This model was reduced to a two-mass-spring-damper system with nonlinear Coulomb friction acting on the motor.

The system parameters were estimated in a two step approach. At first, the frequency response function is estimated using a pseudo random binary excitation. An open-loop and two closed-loop approaches were examined and the resulting frequency response functions compared to each other. The results obtained are comparable to each other, however, the indirect closed-loop approach shows a bias in the lower frequency range. Hence, the open-loop approach is preferred because no controller has to be designed in advance.

Furthermore, this work assumes a horizontal situation of installation of the linear bearing. However, using the open-loop identification strategy, another problem arises if the toothed belt drive is mounted in a non-horizontal orientation. In this case, a pure integrator controller for the motor position can be used to determine the necessary torque for the compensation of the gravity forces. This approach was only tested in simulation and needs further investigation.

Based on the frequency response function resulting from the open-loop experiment, the linear system parameters were estimated by solving an appropriate static optimization problem. The resulting system parameters are then utilized to design a linear controller. The control strategy consists of a proportional-integral velocity controller and a superimposed proportional position controller. Additionally, a feedforward controller is designed. To achieve a higher controller bandwidth, the mechanical resonance is filtered by a prefilter. Two different prefilters were examined, namely a Notch filter and a Butterworth filter. Both show comparable performance in suppressing the mechanical resonance, however, the Butterworth filter is the more robust and, hence, the preferred prefilter, cf., Section 4.2.1 and Chapter 5. The general controller concept is designed to allow the user to adjust the positioning dynamics by only three parameters, i. e., the phase margin of the velocity and position control loop and the resonance suppression factor. Depending on the requirements of the closed-loop system, these tuning parameters can be easily changed without in-depth knowledge on control theory.

The designed feedback controller can then be used to identify the viscous and Coulomb friction parameters in the second identification step. The nonlinear friction parameters were used to design a feedforward controller. The results in Chapter 4 show that the high controller performance is mainly based on the model and parameter accuracy of the feedforward control. Already the linear feedforward controller shows a significantly better

control performance compared to the results obtained without feedforward control. At the costs of an additional identification step, the nonlinear feedforward controller further improves the control performance.

A time-optimal trajectory generator is used to generate the desired position, velocity and acceleration signals for a set point change, as introduced in Section 6.3. Also the velocity estimation based on the incremental encoder position signals was investigated in more detail. It is shown that the velocity resolution, especially in the area of the lower resolution bound of a conventional time-discrete high-pass filter, can be significantly increased. Despite this improvements of the measurement quality, the impact of this additional computational effort on the performance of the closed-loop system is minor compared to the advantages of the presented feedforward controller.

The algorithms developed in this work for system identification and model-based controller design are not limited to belt driven servo systems, as every electromechanical drive chain shows the characteristic frequency response behavior as presented in Chapter 2.

A Parameters

A.1 Data sheet parameters

Table A.1: Data sheet parameters of the toothed belt axis EMMS-AS-70-S-LS-RMB [50] from Festo used in the test rig.

Parameter	Value	Unit
Nominal voltage	360.00	V
Nominal current	2.20	A
Max. current	5.00	A
Nominal velocity	5300.00	rev/min
Max. velocity	6300.00	rev/min
Motor constant k_m	0.65	N m/A
Nominal torque	1.43	N m
Max. torque	3.10	N m
Winding resistance R_m	7.66	Ω
Winding inductance L_m	14.50	mH
Total drive mass moment of inertia Θ_m	0.45	kg/cm ²

Table A.2: Data sheet parameters of the linear axis EGC-70-600-TB-KF-0H-GK [51] from Festo used in the test setup.

Parameter	Value	Unit
Max. feed force	100.00	N
Max. driving torque	1.24	N m
Max. speed	5.00	m/s
Max. acceleration	50.00	m/s ²
Stroke length	0.60	m
Moving load	0.37	kg
Feed constant	78.00	mm/rev
Effective radius r	12.42	mm
Pulley mass moment of inertia Θ_r	23.63	kg/mm ²
Belt pitch	3.00	mm
Preloading force f_0	105.00	N
Belt stiffness c_b	106 250.00	N/m

Table A.3: Data sheet parameters of the connection kit EAMM-A-L38-70A from Festo used in the test setup.

Parameter	Value	Unit
Mass moment of inertia Θ_g	3.20	kg/mm ²
Stiffness	168.75	N m/rad

A.2 Identified parameters

A.2.1 Plant parameters

Table A.4: Plant parameters $G_{\mathcal{A}}$ as output of the identification process of Chapter 3 for additional mass $m_c = 11.2$ kg mounted on the cart.

Parameter	Value	Unit
Motor replacement mass momentum of inertia Θ_e	71.73	kg mm ²
Moving mass m_c	13.44	kg
Stiffness c	203.74	kN/m
Motor viscous damping coefficient d_m	33.17	N s/m
Cart viscous damping coefficient d_c	226.42	N s/m
Resonance frequency f_r	107.11	Hz
Antiresonance frequency f_z	19.59	Hz
Time constant for velocity filter T_R	2.00	ms

Table A.5: Plant parameters $G_{\mathcal{B}}$ as output of the identification process of Chapter 3 for no additional mass $m_c = 0$ kg mounted on the cart.

Parameter	Value	Unit
Motor replacement mass momentum of inertia Θ_e	71.73	kg mm ²
Moving mass m_c	0.96	kg
Stiffness c	222.39	kN/m
Motor viscous damping coefficient d_m	0.01	N s/m
Cart viscous damping coefficient d_c	53.70	N s/m
Resonance frequency f_r	134.00	Hz
Antiresonance frequency f_z	76.51	Hz
Time constant for velocity filter T_R	2.00	ms

A.2.2 Controller parameters

Table A.6: Controller parameters $C_{\mathcal{A}}$ for plant $G_{\mathcal{A}}$, using a Notch filter in the controller design process and a phase margin $\varphi_r^\omega = 60^\circ$ for the velocity controller and $\varphi_r^\varphi = 80^\circ$ for the position controller, as well as a resonance suppression factor of $A_{\text{sup}} = -10$ dB.

Parameter	Value	Unit
φ_r^ω	60.00	$^\circ$
φ_r^φ	80.00	$^\circ$
A_{sup}	-10.00	dB
K_I^{PPI}	1.69	N m/rad
K_P^{PPI}	0.08	N m s/rad
$K_{\text{PP}}^{\text{PPI}}$	10.91	1/s
\tilde{m}_e	0.02	kg m ²
d_n	4.60	—

Table A.7: Controller parameters $C_{\mathcal{B}}$ for plant $G_{\mathcal{A}}$, using a Butterworth filter in the controller design process and a phase margin $\varphi_r^\omega = 60^\circ$ for the velocity controller and $\varphi_r^\varphi = 80^\circ$ for the position controller, as well as a resonance suppression factor of $A_{\text{sup}} = -10$ dB.

Parameter	Value	Unit
φ_r^ω	60.00	$^\circ$
φ_r^φ	80.00	$^\circ$
A_{sup}	-10.00	dB
K_I^{PPI}	1.39	N m/rad
K_P^{PPI}	0.12	N m s/rad
$K_{\text{PP}}^{\text{PPI}}$	6.29	1/s
\tilde{m}_e	0.02	kg m ²
ω_{bw}	123.24	rad/s

A.2.3 Trajectory generator parameters

Table A.8: Parameters $T_{\mathcal{A}}$ of the 7-step trajectory generator used for all experiments.

Parameter	Value	Unit
\dot{j}_{\max}	40.00	m/s ³
\dot{j}_{\min}	−40.00	m/s ³
$\ddot{\xi}_{\max}$	45.00	m/s ²
$\ddot{\xi}_{\min}$	−45.00	m/s ²
$\dot{\xi}_{\max}$	5.00	m/s
$\dot{\xi}_{\min}$	−5.00	m/s
ξ_{\max}	0.57	m
ξ_{\min}	−0.01	m

Table A.9: Parameters $T_{\mathcal{B}}$ of the 7-step trajectory generator.

Parameter	Value	Unit
\dot{j}_{\max}	50.00	m/s ³
\dot{j}_{\min}	−50.00	m/s ³
$\ddot{\xi}_{\max}$	50.00	m/s ²
$\ddot{\xi}_{\min}$	−50.00	m/s ²
$\dot{\xi}_{\max}$	5.00	m/s
$\dot{\xi}_{\min}$	−5.00	m/s
ξ_{\max}	0.57	m
ξ_{\min}	−0.01	m

A.2.4 Friction parameters

$$s_{\xi} = [2, 0.1, 0.01, 0.5, 1.9, 1, 0.001, 0.03, 0.7, 0.002, 0.4, 1.8, 0.02, 0.09, 1.7, 1.1, 0.003, 0.009, 0.8, 1.6, 0.04, 0.004, 0.9, 1.2, 0.005, 1.4, 0.07, 0.6, 0.008, 0.3, 1.5, 0.006, 1.3, 0.06, 0.007, 0.2, 0.08, 0.05] \text{m/s} \quad (\text{A.1})$$

Table A.10: Friction parameters for the system configurations $G_{\mathcal{A}}$ and $G_{\mathcal{B}}$ as outcome of the procedure described in Section 3.6.

Parameter	Value for Configuration		Unit
	$G_{\mathcal{A}}$	$G_{\mathcal{B}}$	
Viscous friction \tilde{d}_v	2.530	2.230	mN m s/rad
Coulomb friction $\tilde{\tau}_c$	0.125	0.115	N m

A.3 Simulation parameters

Table A.11: Plant parameters $S_{\mathcal{A}}$ for simulations.

Parameter	Value	Unit
Motor replacement mass momentum of inertia Θ_e	44.90	kg mm ²
Moving mass m_c	10.00	kg
Stiffness c	200.00	kN/m
Motor viscous damping d_m	100.00	N s/m
Cart viscous damping d_c	100.00	N s/m
Belt damping d	20.00	N s/m
Resonance frequency f_r	133.78	Hz
Antiresonance frequency f_z	22.50	Hz

Table A.12: Plant parameters $S_{\mathcal{B}}$ for simulations.

Parameter	Value	Unit
Motor replacement mass momentum of inertia Θ_e	44.90	kg mm ²
Moving mass m_c	1.00	kg
Stiffness c	200.00	kN/m
Motor viscous damping d_m	100.00	N s/m
Cart viscous damping d_c	100.00	N s/m
Belt damping d	20.00	N s/m
Resonance frequency f_r	149.85	Hz
Antiresonance frequency f_z	71.17	Hz

Table A.13: Plant parameters S_{ℓ} for simulations.

Parameter	Value	Unit
Motor replacement mass momentum of inertia Θ_e	44.90	kg mm ²
Moving mass m_c	10.00	kg
Stiffness c	2000.00	kN/m
Motor viscous damping d_m	100.00	N s/m
Cart viscous damping d_c	100.00	N s/m
Belt damping d	20.00	N s/m
Resonance frequency f_r	423.05	Hz
Antiresonance frequency f_z	71.17	Hz

B Comparison of a PID- and a P-PI-control structure

Figure B.1 shows the block diagram of a PID- and a cascaded P-PI controller with velocity and acceleration feedforward control. Here,

$$\omega_d = s\varphi_d \quad (\text{B.1})$$

and

$$\dot{\omega}_d = s\omega_d \quad (\text{B.2})$$

are the first- and second-order time-derivatives of the desired motor angle φ_d . For comparison reasons, the velocity filter with transfer function G_R is assumed to be ideal, that is

$$G_R = s. \quad (\text{B.3})$$

Under this assumptions, the complementary sensitivity transfer function for the PID-controller, depicted in Figure B.1(a), is given by

$$T_{\varphi_d, \varphi_m}^{\text{PID}} = \frac{K_a^{\text{PID}} s^3 + (K_v^{\text{PID}} + K_D^{\text{PID}}) s^2 + K_P^{\text{PID}} s + K_I^{\text{PID}}}{K_D^{\text{PID}} s^2 + \left(\frac{1}{G} + K_P^{\text{PID}}\right) s + K_I^{\text{PID}}} \quad (\text{B.4})$$

and, for the cascaded P-PI-controller, shown in Figure B.1(b), by

$$T_{\varphi_d, \varphi_m}^{\text{PPI}} = \frac{K_a^{\text{PPI}} s^3 + K_v^{\text{PPI}} K_P^{\text{PPI}} s^2 + (K_v^{\text{PPI}} K_I^{\text{PPI}} + K_P^{\text{PPI}} K_{PP}^{\text{PPI}}) s + K_I^{\text{PPI}} K_{PP}^{\text{PPI}}}{K_P^{\text{PPI}} s^2 + \left(K_I^{\text{PPI}} + K_P^{\text{PPI}} K_{PP}^{\text{PPI}} + \frac{1}{G}\right) s + K_I^{\text{PPI}} K_{PP}^{\text{PPI}}}. \quad (\text{B.5})$$

Obviously, both control structures provide the same complementary sensitivity transfer functions. Comparing the coefficients of the polynomials in s of numerator and denominator from (B.4) and (B.5) result in seven equations of the form

$$K_a^{\text{PPI}} = K_a^{\text{PID}}, \quad (\text{B.6a})$$

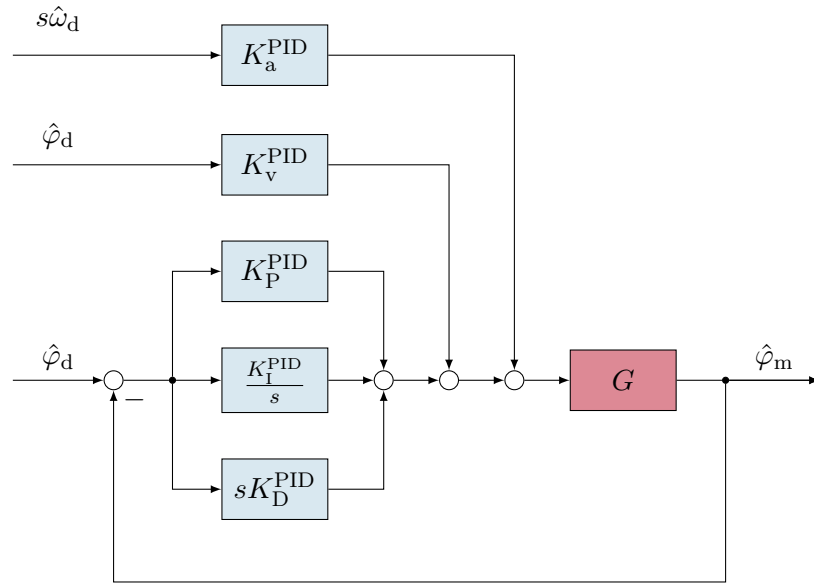
$$K_v^{\text{PPI}} K_P^{\text{PPI}} = K_v^{\text{PID}} + K_D^{\text{PID}}, \quad (\text{B.6b})$$

$$K_v^{\text{PPI}} K_I^{\text{PPI}} + K_P^{\text{PPI}} K_{PP}^{\text{PPI}} = K_P^{\text{PID}}, \quad (\text{B.6c})$$

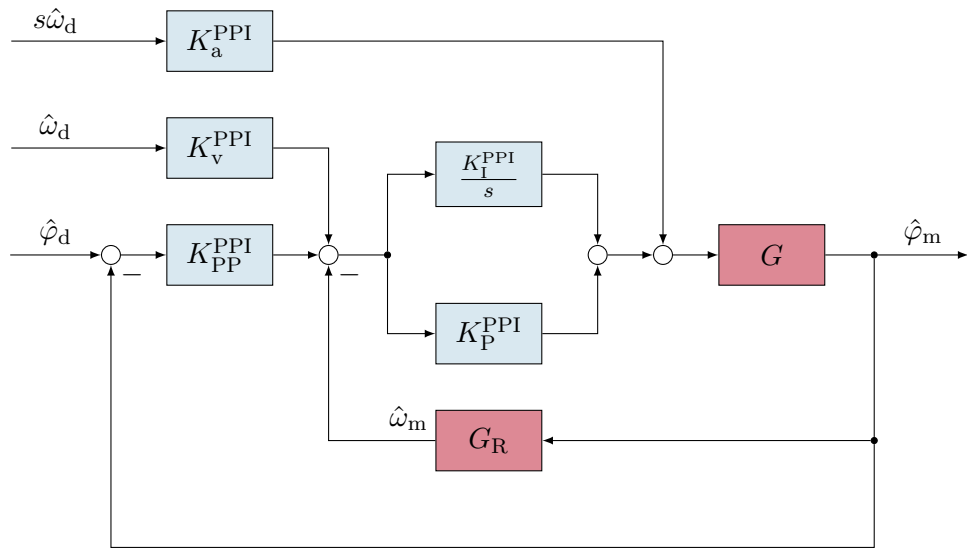
$$K_I^{\text{PPI}} K_{PP}^{\text{PPI}} = K_I^{\text{PID}}, \quad (\text{B.6d})$$

$$K_P^{\text{PPI}} = K_D^{\text{PID}}, \quad (\text{B.6e})$$

$$K_I^{\text{PPI}} + K_P^{\text{PPI}} K_{PP}^{\text{PPI}} = K_P^{\text{PID}} \quad (\text{B.6f})$$



(a) Block diagram of a PID-controller with feedforward controller.



(b) Block diagram of a P-PI-controller with feedforward controller.

Figure B.1: Comparison of a PID-controller and a P-PI cascaded controller including feedforward control.

and

$$K_I^{\text{PPI}} K_{\text{PP}}^{\text{PPI}} = K_I^{\text{PID}}. \quad (\text{B.6g})$$

However, (B.6d) and (B.6g) define the same relationship. Equation (B.6c) and (B.6f) can only be satisfied in a nontrivial way, if and only if

$$K_v^{\text{PPI}} = 1. \quad (\text{B.7})$$

With (B.7), (B.6b) and (B.6e) results in

$$K_v^{\text{PID}} = 0. \quad (\text{B.8})$$

The equations (B.6) allow to convert the P-PI-control structure into the PID-control structure.

If the feedforward part is neglected, that is $K_a^{\text{PID}} = K_v^{\text{PID}} = K_a^{\text{PPI}} = K_v^{\text{PPI}} = 0$, (B.4) reads as

$$T_{\varphi_d, \varphi_m}^{\text{PID}} = \frac{K_D^{\text{PID}} s^2 + K_P^{\text{PID}} s + K_I^{\text{PID}}}{K_D^{\text{PID}} s^2 + \left(\frac{1}{G} + K_P^{\text{PID}}\right) s + K_I^{\text{PID}}} \quad (\text{B.9})$$

and (B.5) becomes

$$T_{\varphi_d, \varphi_m}^{\text{PPI}} = \frac{K_P^{\text{PPI}} K_{\text{PP}}^{\text{PPI}} s + K_I^{\text{PPI}} K_{\text{PP}}^{\text{PPI}}}{K_P^{\text{PPI}} s^2 + \left(K_I^{\text{PPI}} + K_P^{\text{PPI}} K_{\text{PP}}^{\text{PPI}} + \frac{1}{G}\right) s + K_I^{\text{PPI}} K_{\text{PP}}^{\text{PPI}}}. \quad (\text{B.10})$$

Thus, the PID-controller without feedforward control provides one additional zero in the closed-loop transfer function, which, however, cannot be placed independently from its poles.

C Additional derivations

C.1 Event counter approach

The expression (6.11) is derived in the following. The actual distance covered during the sampling time is given by

$$\Delta\xi_{T_s} = \dot{\xi}T_s. \quad (\text{C.1})$$

With (6.7) the real number of increments reads as

$$n_{\text{inc}} - 1 = \frac{\Delta\xi_{T_s}}{\Delta\xi_{\text{min}}} \quad \text{with} \quad n_{\text{inc}} \in \mathbb{R}. \quad (\text{C.2})$$

Hence, the integer number of detected increments is given by

$$n_{\text{inc}} = 1 + \left\lfloor \frac{\dot{\xi}T_s}{\Delta\xi_{\text{min}}} \right\rfloor \quad \text{with} \quad n_{\text{inc}} \in \mathbb{N}. \quad (\text{C.3})$$

Together with (6.8) follows

$$T_{n,\text{inc}}\dot{\xi} = \Delta\xi = (n_{\text{inc}} - 1)\Delta\xi_{\text{min}} = \underbrace{\left\lfloor \frac{\dot{\xi}T_s}{\Delta\xi_{\text{min}}} \right\rfloor}_{\substack{(\text{C.3}) \\ = n_{\text{inc}} - 1}} \Delta\xi_{\text{min}}. \quad (\text{C.4})$$

Assuming only an error of $\pm\Delta t_{\min}$ in the time measurement for $T_{n,\text{inc}}$ yields an error in the velocity signal. With (6.4) it follows that

$$\begin{aligned}
 \Delta \dot{\xi}_{\text{h,err}} &= 100 \frac{\dot{\xi}_{\text{h}} - \dot{\xi}}{\dot{\xi}} \\
 &\stackrel{(6.4)}{=} 100 \frac{\frac{(n_{\text{inc}}-1)\Delta\xi_{\min}}{T_{n,\text{inc}} \pm \Delta t_{\min}} - \dot{\xi}}{\dot{\xi}} \\
 &= 100 \left(\underbrace{\frac{(n_{\text{inc}}-1)\Delta\xi_{\min}}{\dot{\xi}}}_{\stackrel{(6.7)}{=} T_{n,\text{inc}}} \frac{1}{T_{n,\text{inc}} \pm \Delta t_{\min}} - 1 \right) \\
 &= \mp 100 \frac{\Delta t_{\min}}{T_{n,\text{inc}} \pm \Delta t_{\min}} \\
 &= \mp 100 \frac{\Delta t_{\min} \dot{\xi}}{T_{n,\text{inc}} \dot{\xi} \pm \Delta t_{\min} \dot{\xi}} \\
 &\stackrel{(C.4)}{=} \mp 100 \frac{\Delta t_{\min} \dot{\xi}}{\left\lfloor \frac{\dot{\xi} T_s}{\Delta\xi_{\min}} \right\rfloor \Delta\xi_{\min} \pm \Delta t_{\min} \dot{\xi}}. \tag{C.5}
 \end{aligned}$$

Under the assumption $\Delta t_{\min} \ll T_s$ and the usage of (6.6) the expression can be further simplified to

$$\begin{aligned}
 \dot{\xi}_{\text{h,err}} &= \mp 100 \frac{\Delta t_{\min} \dot{\xi}}{\left\lfloor \frac{\dot{\xi} T_s}{\Delta\xi_{\min}} \right\rfloor \Delta\xi_{\min} \pm \Delta t_{\min} \dot{\xi}} \\
 &\approx \mp 100 \frac{\Delta t_{\min} \dot{\xi}}{\left\lfloor \frac{\dot{\xi} T_s}{\Delta\xi_{\min}} \right\rfloor \Delta\xi_{\min}} \\
 &\stackrel{(6.6)}{=} \mp \frac{\dot{\xi}}{\left\lfloor \frac{\dot{\xi} T_s}{\Delta\xi_{\min}} \right\rfloor \dot{\xi}_{\text{h,max}}}. \tag{C.6}
 \end{aligned}$$

C.2 Gate measurement approach

The expression (6.16) is derived in the following. With the actual velocity given by

$$\dot{\xi} = \frac{\Delta\xi_{\min}}{T_{\text{inc}}}, \tag{C.7}$$

it follows that the relative velocity error due to an error in the time measurement T_{inc} of $\pm\Delta t_{\text{min}}$, when estimating the velocity according to (6.14), is given by

$$\begin{aligned}
\Delta \dot{\xi}_{l,\text{err}} &= 100 \frac{\dot{\xi}_l - \dot{\xi}}{\dot{\xi}} \\
&\stackrel{(6.14)}{=} 100 \frac{\frac{\Delta \xi_{\text{min}}}{T_{\text{inc}} \pm \Delta t_{\text{min}}} - \dot{\xi}}{\dot{\xi}} \\
&= 100 \left(\frac{\Delta \xi_{\text{min}}}{\dot{\xi}(T_{\text{inc}} \pm \Delta t_{\text{min}})} - 1 \right) \\
&= 100 \frac{\Delta \xi_{\text{min}} - \overbrace{\dot{\xi}(T_{\text{inc}} \pm \Delta t_{\text{min}})}^{(C.7) \Delta \xi_{\text{min}}}}{\dot{\xi}(T_{\text{inc}} \pm \Delta t_{\text{min}})} \\
&= \mp 100 \frac{\Delta t_{\text{min}} \dot{\xi}}{(T_{\text{inc}} \pm \Delta t_{\text{min}}) \dot{\xi}} \\
&\stackrel{(6.15)}{=} \mp 100 \frac{\overbrace{\frac{1}{\xi_{l,\text{max}}}}^{(6.15)} \frac{\Delta t_{\text{min}}}{\Delta \xi_{\text{min}}}}{\frac{T_{\text{inc}}}{\Delta \xi_{\text{min}}} \pm \frac{\Delta t_{\text{min}}}{\Delta \xi_{\text{min}}}} \\
&\stackrel{(C.7)}{=} \mp 100 \left(\frac{\dot{\xi}}{\dot{\xi}_{l,\text{max}} \pm \dot{\xi}} \right). \tag{C.8}
\end{aligned}$$

Bibliography

- [1] F. Schütte, *Automatisierte Reglerinbetriebnahme für elektrische Antriebe mit schwingungsfähiger Mechanik*. Aachen: Shaker-Verlag, 2002, ISBN: 978-3-832-21226-1.
- [2] B. Henke, *Modellgestützte automatisierte Reglerauslegung für elektromechanische Antriebssysteme*. Aachen: Shaker-Verlag, 2016, ISBN: 978-3-844-04504-8.
- [3] M. Jokinen, “Centralized motion control of a linear tooth belt drive: analysis of the performance and limitations,” PhD thesis, Lappeenranta University of Technology, Lappeenranta, Finland, 2010.
- [4] M. Jokinen, S. Saarakkala, M. Niemela, R. Pollanen, and J. Pyrhonen, “Physical drawbacks of linear high-speed tooth belt drives,” in *International Symposium on Power Electronics, Electrical Drives, Automation and Motion (SPEEDAM)*, IEEE, Nov. 2008, pp. 872–877.
- [5] A. Selezneva, “Modeling and synthesis of tracking control for the belt drive system,” Master’s thesis, Lappeenranta University of Technology, Lappeenranta, Finland, 2007.
- [6] S. E. Saarakkala and M. Hinkkanen, “Identification of two-mass mechanical systems using torque excitation: Design and experimental evaluation,” *IEEE Transactions on Industry Applications*, vol. 51, no. 5, pp. 4180–4189, 2015.
- [7] N. Nevaranta, J. Parkkinen, M. Niemelä, T. Lindh, O. Pyrhönen, and J. Pyrhönen, “Recursive identification of linear tooth belt-drive system,” in *Proc. of the 16th European Conference on Power Electronics and Applications (EPE’14-ECCE Europe)*, Aug. 2014, pp. 1–8.
- [8] S. E. Saarakkala, “Identification and speed control design of resonating mechanical systems in electric drives,” PhD thesis, Aalto University, Department of Electrical Engineering and Automation, 2014, ISBN: 978-952-60-5827-6.
- [9] S. E. Saarakkala, A. Alahaivala, M. Hinkkanen, and J. Luomi, “Dynamic emulation of multi-mass mechanical loads in electric drives,” in *Proc. of the 14th European Conference on Power Electronics and Applications (EPE 2011)*, IEEE, Aug. 2011, pp. 1–10.
- [10] S. E. Saarakkala, T. Leppinen, M. Hinkkanen, and J. Luomi, “Parameter estimation of two-mass mechanical loads in electric drives,” in *Proc. of the 12th IEEE International Workshop on Advanced Motion Control (AMC)*, IEEE, Mar. 2012, pp. 1–6.
- [11] S. E. Saarakkala and M. Hinkkanen, “Identification of two-mass mechanical systems in closed-loop speed control,” in *Proc. of the 39th Annual Conference of the IEEE Industrial Electronics Society (IECON)*, IEEE, Nov. 2013, pp. 2905–2910.

- [12] S. E. Saarakkala, M. Hinkkanen, and K. Zenger, “Speed control of two-mass mechanical loads in electric drives,” in *Energy Conversion Congress and Exposition (ECCE)*, IEEE, Sep. 2012, pp. 1246–1253.
- [13] S. E. Saarakkala and M. Hinkkanen, “State-space speed control of two-mass mechanical systems: Analytical tuning and experimental evaluation,” *IEEE Transactions on Industry Applications*, vol. 50, no. 5, pp. 3428–3437, Sep. 2014.
- [14] L. Harnefors, S. E. Saarakkala, and M. Hinkkanen, “Speed control of electrical drives using classical control methods,” *IEEE Transactions on Industry Applications*, vol. 49, no. 2, pp. 889–898, 2013.
- [15] M. Weck, *Werkzeugmaschinen 3: Mechatronische Systeme, Vorschubantriebe, Prozessdiagnose*. Springer-Verlag Berlin Heidelberg, 2006.
- [16] A. Hace, K. Jezernik, and A. Sabanovic, “A new robust position control algorithm for a linear belt-drive,” in *Proc. of the IEEE International Conference on Mechatronics (ICM)*, Jun. 2004, pp. 358–363.
- [17] K. Jezernik, A. Sabanovic, et al., “SMC with disturbance observer for a linear belt drive,” *IEEE Transactions on Industrial Electronics*, vol. 54, no. 6, pp. 3402–3412, Dec. 2007.
- [18] G. Ellis and Z. Gao, “Cures for low-frequency mechanical resonance in industrial servo systems,” in *Proc. of the IEEE Industry Applications Conference. 36th IAS Annual Meeting*, IEEE, vol. 1, Sep. 2001, pp. 252–258.
- [19] H. Gurocak, *Industrial Motion Control: Motor Selection, Drives, Controller Tuning, Applications*. John Wiley & Sons Ltd, Chichester, West Sussex, United Kingdom, 2015.
- [20] R. S. Beikmann, N. C. Perkins, and A. G. Ulsoy, “Free vibration of serpentine belt drive systems,” *Journal of Vibration and Acoustics*, vol. 118, no. 3, pp. 406–413, 1996.
- [21] S. N. Vukosavic and M. R. Stojic, “Suppression of torsional oscillations in a high-performance speed servo drive,” *IEEE Transactions on Industrial Electronics*, vol. 45, no. 1, pp. 108–117, 1998.
- [22] W. Schnell, D. Gross, and W. Hauger, *Technische Mechanik 2 Elastostatik*, 13th ed. Springer Berlin Heidelberg, 2013.
- [23] C. Iurian, F. Ikhoulane, J. Rodellar Benedé, and R. Griño Cubero, “Identification of a system with dry friction,” Universitat Politècnica de Catalunya, Tech. Rep., 2005.
- [24] L. Ljung, “System Identification,” in *Signal Analysis and Prediction*, A. Procházka, J. Uhlíř, P. W. J. Rayner, and N. G. Kingsbury, Eds. Birkhäuser Boston, 1998, pp. 163–173, ISBN: 978-1-4612-1768-8.
- [25] L. Ljung, Ed., *System Identification: Theory for the User*, 2nd ed. Upper Saddle River, NJ, USA: Prentice Hall PTR, 1999, ISBN: 0-13-656695-2.
- [26] R. Isermann and M. Munchhof, *Identification of Dynamic Systems*. Springer Berlin Heidelberg, 2011, ISBN: 978-3-540-78879-9.


- [27] K.-K. Shyu and Y.-Y. Lee, “**Identification of electro-mechanical actuators within limited stroke**,” *Journal of Vibration and Control*, vol. 16, no. 12, pp. 1737–1761, 2010.
- [28] N. Nevaranta, J. Parkkinen, T. Lindh, M. Niemelä, O. Pyrhönen, and J. Pyrhönen, “**Online estimation of linear tooth belt drive system parameters**,” *IEEE Transactions on Industrial Electronics*, vol. 62, no. 11, pp. 7214–7223, 2015.
- [29] I. D. Landau and G. Zito, *Digital Control Systems*. London: Springer, 2006, ISBN: 978-1-84628-056-6.
- [30] J. P. Clary and G. F. Franklin, “**Self-tuning control with a priori plant knowledge**,” in *Proc. of the 23rd IEEE Conference on Decision and Control*, Las Vegas, NV, Dec. 1984, pp. 369–374.
- [31] B. V. Gnedenko and A. N. Kolmogorov, *Limit distributions for sums of independent random variables*, ser. Addison-Wesley Mathematics Series. Cambridge, MA: Addison-Wesley, 1954, Translated and annotated by K. L. Chung. With an Appendix by J. L. Doob. MR:0062975. Zbl:0056.36001.
- [32] D. W. Marquardt, “**An algorithm for least-squares estimation of nonlinear parameters**,” *Journal of the Society for Industrial and Applied Mathematics*, vol. 11, no. 2, pp. 431–441, 1963.
- [33] K. Levenberg, “**A method for the solution of certain non-linear problems in least squares**,” *Quarterly of Applied Mathematics*, vol. 2, no. 2, pp. 164–168, 1944.
- [34] J. J. Moré, “**The Levenberg-Marquardt algorithm: Implementation and theory**,” in *Numerical Analysis*, ser. Lecture Notes in Mathematics, G. Watson, Ed., vol. 630, Springer Berlin Heidelberg, 1978, pp. 105–116, ISBN: 978-3-540-08538-6.
- [35] T. F. Coleman and Y. Li, “**On the convergence of interior-reflective Newton methods for nonlinear minimization subject to bounds**,” *Mathematical programming*, vol. 67, no. 1, pp. 189–224, 1994.
- [36] T. F. Coleman and Y. Li, “**An interior trust region approach for nonlinear minimization subject to bounds**,” *SIAM Journal on optimization*, vol. 6, no. 2, pp. 418–445, 1996.
- [37] J. A. Nelder and R. Mead, “**A simplex method for function minimization**,” *The Computer Journal*, vol. 7, no. 4, pp. 308–313, 1965.
- [38] P. Schmidt and T. Rehm, “**Notch filter tuning for resonant frequency reduction in dual inertia systems**,” in *Conference Record of the 34th IAS Annual Meeting on Industry Applications Conference.*, IEEE, vol. 3, Oct. 1999, pp. 1730–1734.
- [39] S. Butterworth, “**On the theory of filter amplifiers**,” *Wireless Engineer*, vol. 7, no. 6, pp. 536–541, 1930.
- [40] W. K. Ho, C. C. Hang, and L. S. Cao, “**Tuning of PID controllers based on gain and phase margin specifications**,” *Automatica*, vol. 31, no. 3, pp. 497–502, 1995.
- [41] K. J. Åström and T. Hägglund, *Advanced PID control*. Research Triangle Park, NC, USA: ISA-The Instrumentation, Systems and Automation Society, 2006.

- [42] D. G. Luenberger and Y. Ye, *Linear and nonlinear programming*. Heidelberg, New York, London: Springer, 2015, vol. 228.
- [43] R. Petrella, M. Tursini, L. Peretti, and M. Zigliotto, “Speed measurement algorithms for low-resolution incremental encoder equipped drives: a comparative analysis,” in *Proc. of the International Aegean Conference on Electrical Machines and Power Electronics (ACEMP)*, Bodrum, TUR, Sep. 2007, pp. 780–787.
- [44] R. Petrella and M. Tursini, “An Embedded System for Position and Speed Measurement Adopting Incremental Encoders,” *Conference Record of the 39th IAS Annual Meeting of the IEEE Industry Applications Conference.*, vol. 44, no. 5, pp. 1436–1444, 2004.
- [45] P. Barkan, “A study of the contact bounce phenomenon,” *IEEE Transactions on Power Apparatus and Systems*, vol. PAS-86, no. 2, pp. 231–240, 1967.
- [46] C. Bohn and D. Atherton, “An analysis package comparing PID anti-windup strategies,” *IEEE Control Systems*, vol. 15, 2 1995.
- [47] K. J. Åström and L. Rundqwist, “Integrator windup and how to avoid it,” in *Proc. of the American Control Conference*, Jun. 1989, pp. 1693–1698.
- [48] M. Hofmair, M. Böck, and A. Kugi, “Time-optimal trajectory generation, path planning and control for a wood patching robot,” in *Proc. of the Conference on Control Applications (CCA)*, Sydney, Australia, Sep. 2015, pp. 459–465.
- [49] J. P. LaSalle, “Time Optimal Control Systems,” eng, in *Proc. of the National Academy of Sciences of the United States of America*, vol. 45, Apr. 1959, pp. 573–577.
- [50] *Servo motors EMMS-AS*, accessed 24.4.2017, Festo.
- [51] *Toothed belt axis EGC-TB with recirculating ball bearing guide*, accessed 24.4.2017, Festo.

Eidesstattliche Erklärung

Hiermit erkläre ich, dass die vorliegende Arbeit gemäß dem Code of Conduct – Regeln zur Sicherung guter wissenschaftlicher Praxis (in der aktuellen Fassung des jeweiligen Mitteilungsblattes der TU Wien), insbesondere ohne unzulässige Hilfe Dritter und ohne Benutzung anderer als der angegebenen Hilfsmittel, angefertigt wurde. Die aus anderen Quellen direkt oder indirekt übernommenen Daten und Konzepte sind unter Angabe der Quelle gekennzeichnet. Die Arbeit wurde bisher weder im In- noch im Ausland in gleicher oder in ähnlicher Form in anderen Prüfungsverfahren vorgelegt.

Wien, 14. Juni, 2017



David Gruber